


Winter 2009

Comparative Study of Forward and Diffusely Scattered Light in a Coherently Prepared Ultracold Rubidium Gas

Rocio Gisel Olave Gonzalez
Old Dominion University

Follow this and additional works at: https://digitalcommons.odu.edu/physics_etds

 Part of the [Atomic, Molecular and Optical Physics Commons](#), [Optics Commons](#), and the [Quantum Physics Commons](#)

Recommended Citation

Gonzalez, Rocio G.. "Comparative Study of Forward and Diffusely Scattered Light in a Coherently Prepared Ultracold Rubidium Gas" (2009). Doctor of Philosophy (PhD), Dissertation, Physics, Old Dominion University, DOI: 10.25777/309d-2g02
https://digitalcommons.odu.edu/physics_etds/111

This Dissertation is brought to you for free and open access by the Physics at ODU Digital Commons. It has been accepted for inclusion in Physics Theses & Dissertations by an authorized administrator of ODU Digital Commons. For more information, please contact digitalcommons@odu.edu.

**COMPARATIVE STUDY OF FORWARD AND
DIFFUSELY SCATTERED LIGHT IN A COHERENTLY
PREPARED ULTRACOLD RUBIDIUM GAS**

by

Rocio Gisel Olave Gonzalez
Bachelor of Science, UTEP, 1999
Master of Science, ODU, 2003

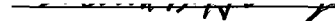
A Dissertation Submitted to the Faculty of
Old Dominion University in Partial Fulfillment of the
Requirement for the Degree of

DOCTOR OF PHILOSOPHY


DEPARTMENT OF PHYSICS

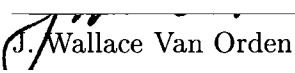
OLD DOMINION UNIVERSITY
December 2009

Approved by:


Mark D. Havey (Director)


Charles I. Sukenik


Leposava Vuskovic


J. Wallace Van Orden


Amin N. Dharamsi

ABSTRACT

COMPARATIVE STUDY OF FORWARD AND DIFFUSELY SCATTERED LIGHT IN A COHERENTLY PREPARED ULTRACOLD RUBIDIUM GAS

Rocio Gisel Olave

Old Dominion University, 2009

Director: Dr. Mark D. Havey

A comparison between forward and diffusely scattered light propagating in a coherently prepared ultracold ^{87}Rb atomic vapor is presented. This research is part of the ongoing effort to characterize the processes, such as diffusion, that contribute to coherence loss in atomic media under conditions of electromagnetically induced transparency, for applications in realistic systems. Toward this end, a magneto optical trap (MOT) of ^{87}Rb has been built, and the atomic vapor sample characterized in terms of atomic density, shape and size, temperature, and optical depth. Next, two co-propagating beams were sent through the sample, to establish an electromagnetically induced transparency in a Λ -type system. In these measurements the two laser fields are not phase-locked, so ground state coherence will be affected by the lasers' phase fluctuations. Observation of the forward and diffusely scattered light were made for different conditions of probe pulse length, control field intensity, and probe field frequency detuning. Storage and retrieval of slow light pulses was achieved for the forward scattering (transmission) channel, but was not observed unambiguously in the diffusely scattered (fluorescence) channel.

To my husband Carlos, for all our dreams, our goals, our hopes. For bringing endless love and joy to our lives. You are my heart.

To my daughter Giselle, and my son Ian. For everything the future holds in store for us. For being a constant source of joy and delight. You are the best gift life could have given me.

To my dad Héctor, and my mom Conchita, for your endless love, for your endless supply of “packets of cheer,” and “eighty-four kisses and more,” for being my best teachers every day of my life, and for sharing with me your passion for knowledge.

To my sister Luz Eugenia (Luce), for your endless support, for always pushing me forward, for the source of inspiration you are, and for always being there for me.

To my big brother Héctor Daniel, and my “little brother” Daniel Alejandro, for all the moments we’ve shared, for all the memories and the common source of love and inspiration we have.

To Blanca, and my nephews Ale, Danielito, Gabriel, Teto, and Kristy. For always being cheerful, for being just as you are.

To my father and mother-in-law, Carlos and Carolina, for your warmth and love. For welcoming me into your lives as another daughter, for being an example to follow, for cheering me on.

And to my Lord, and Mary Lady of Guadalupe. For everything.

ACKNOWLEDGMENTS

First of all, I would like to thank Dr. Mark Havey. His passion for atomic physics has made learning a very intense and enjoyable experience. I thank him for continuously challenging and encouraging me, for his patience and understanding along this journey. I thank him for always listening, and not just about physics. I thank him for many enjoyable conversations, of physics, and of this and that. For his optimism when I've been pessimistic, for his steadiness throughout these years. As a teacher, as an advisor, as a person, it has been a pleasure to know him and work with him.

The faculty at the Physics Department have always been friendly and helpful, but I would like particularly to give thanks to Dr. Sukenik, for always helping me the many times I knocked on his door, for always trying to speak in Spanish to me, and for his sense of humor. I also give thanks to Dr. Vuskovic and Dr. Dodge for creating such a positive environment for women in the Physics Department, and to the members of my dissertation committee for your good advice.

Many people contributed in some way or another to the development of this project, but I would like to mention particularly Aye Lu Win for sharing with me many hours of head-scratching, and many hours of data taking, for his assistance and for his friendship. Thanks to Salim Balik, from whom I've learned a lot, for all his help, his friendship, and for making the labs such a pleasant environment. I also thank Chris Hopper, and wish him good luck in taking over the laboratory.

And I would like to thank my friends, who have helped me through their support and laughter. Particularly, I would like to give thanks to Mickey Ann (RIP) and Abel Garcia, for being a source of inspiration, for their support, and their friendship. Thanks to Vicky (RIP) and Walt Hooks, who opened their home and hearts to Carlos and me, and made us feel welcome all the time we've been in Norfolk. Thanks to Claudia and Vance Trznadel, Felipe and Victoria Cruz, Marija Raskovic and Héctor García, Fr. Wayne L. Ball, Fr. David McGuire, Karla Rojasvértiz, Sandra García, Alejandra Méndez, Rozzio Rivera, Luisa A. Chávez, the group of "mexicanos de ODU", the group of friends from the "comité hispano y el coro" at Holy Trinity Catholic Church, and to my fellow students, for walking with me along the way.

TABLE OF CONTENTS

	Page
LIST OF TABLES	vii
LIST OF FIGURES	ix
Chapter	
I INTRODUCTION	1
I.1 EIT, QUANTUM COHERENCE AND CONTROL	1
I.2 HISTORICAL BACKGROUND	3
I.3 MOTIVATION	6
II THEORETICAL BACKGROUND	8
II.1 LASER COOLING AND TRAPPING	8
II.2 $^{87}\text{RUBIDIUM}$	15
II.3 ELECTROMAGNETICALLY INDUCED TRANSPARENCY	18
II.3.1 THE IDEAL THREE-LEVEL ATOM	19
II.3.2 OPTICAL PROPERTIES OF AN EIT PREPARED MEDIUM	24
II.4 MULTIPLE SCATTERING IN RANDOM MEDIA	31
III GENERAL EXPERIMENTAL ARRANGEMENT	34
III.1 DIODE LASER SYSTEMS	34
III.1.1 EXTERNAL CAVITY DIODE LASERS	34
III.1.2 LASER FREQUENCY STABILIZATION AND DOPPLER-FREE SATURATED ABSORPTION SPECTROSCOPY	36
III.1.3 LASER POWER AMPLIFICATION	41
III.1.4 LASER FREQUENCY SHIFTING AND ACOUSTO-OPTIC MODULATORS	42
III.2 THE VACUUM CHAMBER SYSTEM	46
III.3 THE MAGNETO OPTICAL TRAP CONFIGURATION	47
III.4 CHARACTERIZATION OF THE ULTRACOLD GAS	50
III.4.1 FLUORESCENCE IMAGING	50
III.4.2 ABSORPTION IMAGING	53
III.4.3 TIME-DEPENDENT FLUORESCENCE	55
IV DATA ACQUISITION AND RESULTS	61
IV.1 INITIAL CONSIDERATIONS FOR EIT MEASUREMENTS	61
IV.2 TRANSMISSION OF A PROBE PULSE PROPAGATING THROUGH A COHERENTLY PREPARED RB CLOUD	64
IV.3 FLUORESCENCE OF A PROBE PULSE PROPAGATING THROUGH A COHERENTLY PREPARED RB CLOUD	76

V	CONCLUSIONS AND FUTURE EXPERIMENTS	86
	BIBLIOGRAPHY	88
	APPENDICES	
A	THE TWO-LEVEL ATOM	94
	A.1 THE PROBABILITY AMPLITUDE APPROACH	94
	A.2 THE WEAK FIELD LIMIT	96
	A.3 OPTICAL ATTENUATION AND LINEAR SUSCEPTIBILITY OF THE MEDIUM	98
	A.4 THE DENSITY MATRIX APPROACH	102
	A.5 THE AUTLER-TOWNES EFFECT	104
B	ESTIMATE OF THE ADIABATIC EVOLUTION CONDITION	106
C	OPTICAL PUMPING AND RATE EQUATIONS MODEL	109
	VITA	111

LIST OF TABLES

Table	Page
1. Physical properties of ^{87}Rb	16
2. ^{87}Rb D2 ($5^2\text{S}_{1/2} \rightarrow 5^2\text{P}_{3/2}$) transition optical properties.	18
3. Operation and characterization parameters of the MOT.	60
4. Estimates of the condition for adiabatic evolution for the transmission measurements.	108
5. Estimates of the condition for adiabatic evolution for the fluorescence measurements.	108

LIST OF FIGURES

Figure	Page
1. Three-level atoms in the presence of two classical radiation fields. . .	2
2. Radiation pressure on an atom.	8
3. Velocity dependent forces acting on an atom in a one-dimensional optical molasses.	10
4. Components of polarization gradient cooling.	12
5. Trapping atoms in a magneto-optical trap.	14
6. Rubidium 87 transition energy diagram for the D2 line.	17
7. The three-level atom in a Λ scheme, in the presence of two classical electromagnetic fields.	20
8. The three-level atom in a Λ scheme, including relaxation rates.	25
9. Complex susceptibility $\chi(\omega)$ in an EIT system.	28
10. External-cavity diode laser (ECDL).	35
11. Saturated-absorption spectroscopy setup.	39
12. Saturated-absorption spectrum of ^{87}Rb for transitions from the ground state $F = 2$ to excited states F'	39
13. Flow diagram of the electronic components for the frequency locking setup.	40
14. Schematic of two diode lasers in a master-slave configuration.	42
15. Laser beam and AOM optical systems.	44
16. Rb vacuum chamber.	47
17. Magneto optical trap setup	48
18. Detection setup for MOT fluorescence and absorption imaging.	51
19. MOT spatial density distribution.	52
20. The ballistic expansion of the ^{87}Rb atomic cloud.	54
21. Detuning-dependent MOT probe absorption measurements.	56
22. Time-dependent MOT fluorescence detection setup.	57
23. Detuning-dependent MOT probe fluorescence measurements.	58
24. Relevant hyperfine lambda scheme.	61
25. The coupling and probe laser beams combined bandwidth.	62
26. Data acquisition time sequence.	63
27. Experimental setup for detection in transmission of a probe pulse through the EIT prepared medium.	64
28. Relative signal comparison for variable probe pulse duration.	65
29. Calibration set of measurements.	66
30. EIT signal as a function of Ω_c	68
31. Intensity of the steady-state transmitted EIT signal as a function of Ω_c	69
32. Probe frequency detuning dependence of the EIT transmission signal.	71
33. Light shift of the $ 2\rangle \rightarrow 1\rangle$ transition caused by the control laser field coupling the $ 2\rangle \rightarrow 2\rangle$ transition.	72
34. Slow light storage and retrieval representative timing diagram.	73

35.	Slow light storage and retrieval with variable delays.	74
36.	Slow light retrieval signal for variable storage times.	75
37.	Experimental setup for detection of fluorescence from a probe pulse propagating through the EIT prepared medium.	77
38.	Probe fluorescence from an EIT Rb cloud as a function of the control field Rabi frequency Ω_c	78
39.	Probe fluorescence as the control field ($\Omega_c = 0.69 \Gamma_p$) is turned off/on for various time delays.	80
40.	Probe fluorescence as the control field ($\Omega_c = 0.18 \Gamma_p$) is turned off/on for various time delays.	81
41.	Coherent optical pumping.	82
42.	Probe fluorescence from an EIT prepared medium as a function of probe frequency detuning Δ_p	85
43.	An ideal two-level atom in the presence of a classical laser field. . . .	95
44.	Complex susceptibility $\chi(\omega)$ of a medium composed of two-level atoms.	100
45.	Optical pumping and rate equations model.	110

CHAPTER I

INTRODUCTION

In recent years the fields of quantum and nonlinear optics have been greatly enriched by the development of techniques which allow controlled coherent manipulation of matter through light. The linear and nonlinear optical properties of a medium can be dramatically modified by establishing controlled atomic coherence and interference effects, as has been evidenced by the processes of coherent population trapping (CPT) and electromagnetically induced transparency (EIT). In these processes, two radiation fields drive a three-level atom into a coherent superposition of states, at which point absorption from the radiation fields is suppressed. Most of the emphasis of recent research is in optimizing control of the coherent system, or using an optimized coherently prepared medium as the basis for experiments [1]. It is necessary, therefore, to have a better understanding of the mechanisms, such as diffusion, that contribute to coherence loss for applications in realistic systems.

The intention of this dissertation research is to provide a better understanding of such coherence loss by comparing forward and diffusely scattered light in an ultracold ^{87}Rb atomic gas, which has been coherently prepared by the process of electromagnetically induced transparency.

In this introduction, the basic nature of EIT is discussed first, followed by a section presenting briefly the emergence and evolution of EIT-based research and broader impacts of the field, and last, the motivation and purpose of this dissertation research.

I.1 EIT, QUANTUM COHERENCE AND CONTROL

Electromagnetically induced transparency, or EIT, is an interference effect between different transition pathways in a three-level atomic system in the presence of two electromagnetic fields, which induce quantum coherence within the atoms. This interference leads to surprising consequences, such as rendering an otherwise opaque medium into a transparent one [2, 3].

Consider an atomic medium consisting of three level atoms (or systems that can be reduced to three levels), where the energy states $|1\rangle$, $|2\rangle$, and $|3\rangle$ are called the bare states of the atom, i.e. the states of the unperturbed atom. Now place

This dissertation follows the style of *Physical Review A*

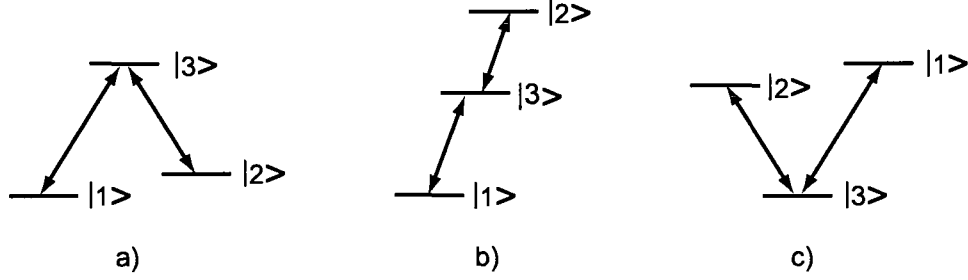


FIG. 1: Three-level atoms in the presence of two classical radiation fields. (a) Lambda (Λ) scheme. (b) Ladder or cascade scheme. (c) Vee (V) scheme. In all three cases there may be dipole coupling between states $|1\rangle$ and $|3\rangle$ and between states $|2\rangle$ and $|3\rangle$, but not between states $|1\rangle$ and $|2\rangle$.

this atomic medium in the presence of two near-resonant classical electromagnetic waves: a control (also called coupling) field \vec{E}_c and a probe field \vec{E}_p , which have electric dipole-coupling strengths characterized by their Rabi frequencies Ω_c and Ω_p respectively. Figure 1 shows the three possible schemes: lambda (Λ), ladder or cascade, and vee (V). It can be seen that the electric fields may each drive a dipole transition between a pair of states, $|1\rangle \leftrightarrow |3\rangle$ or $|2\rangle \leftrightarrow |3\rangle$, but there is no electric dipole coupling allowed for the third pair of states, $|1\rangle \leftrightarrow |2\rangle$.

The Hamiltonian of the system must now include the interactions driven by these fields, and the eigenstates of the new Hamiltonian will be superpositions of the bare states. Since the Λ scheme is specially relevant for this experiment, it will be used as an example. For the particular situation when both radiation fields are at their transition resonance frequency, two of the eigenstates are coherent superpositions of the two lower states such that

$$|C\rangle = \frac{\Omega_p}{\Omega}|1\rangle + \frac{\Omega_c}{\Omega}|2\rangle, \quad (1)$$

$$|NC\rangle = \frac{\Omega_c}{\Omega}|1\rangle - \frac{\Omega_p}{\Omega}|2\rangle, \quad (2)$$

$$(3)$$

where $\Omega = \sqrt{|\Omega_p|^2 + |\Omega_c|^2}$. The eigenstate $|C\rangle$ may be coupled to the excited state $|3\rangle$ through the electric dipole interaction, but the other eigenstate $|NC\rangle$ may not; once the atomic population is in this state it ceases to interact with the radiation fields, thus the medium becomes transparent. Because of the negative sign

in $|NC\rangle$, the probability transition amplitudes for the atoms to be excited are of equal and opposite magnitude, hence the amplitude is zero. This is a destructive interference effect due to the mutual coherence of the ground states that has been established due to the presence of the two radiation fields. The state $|NC\rangle$ is also called a “dark” state, since the radiation fields do not “see” or interact with atoms that have evolved into this state. Any dephasing between these two ground states will drive the atom out of the dark state, suppressing the transparency.

In EIT atoms are in the ground state, which is the lowest energy state. The probe field, which drives the transition $|1\rangle \leftrightarrow |3\rangle$, is assumed to be very weak. The control field is assumed to be driving the essentially empty transition $|2\rangle \leftrightarrow |3\rangle$, but it is also assumed to be very intense. EIT may also be pictured as the interference between transition pathways [2], the amplitude to be in the excited state may arise from a direct pathway $|1\rangle \rightarrow |3\rangle$, or from indirect pathways such as $|1\rangle \rightarrow |3\rangle \rightarrow |2\rangle \rightarrow |3\rangle$. Since the intensity of the control field is much larger than that of the probe field, the indirect pathways may have a probability amplitude as large as the direct route to excitation, and may thus interfere destructively, suppressing absorption of radiation.

When the system is considered in terms of an atomic system “dressed” by the strong coupling field, the medium not only becomes transparent to the probe field, but it acquires some very peculiar optical properties. For example, the medium has a “normal” dispersion about the transparency frequency, or slow group velocity of the probe accompanied by compression of the pulse, which may be controlled by adjusting the coupling field strength. The power of EIT resides in the ease of control of the system through external parameters, such as the coupling field intensity, atomic density, or laser frequency detuning.

I.2 HISTORICAL BACKGROUND

In 1961, Fano explained the observed asymmetric emission spectrum from He atoms irradiated with far-ultraviolet light in terms of interference between different autoionization pathways [4]. This early work led to the prediction by Arimondo and Orriols that atoms could be pumped into non-absorbing states by interference processes [5, 6]; the first observations of coherent population trapping (CPT) with sodium atoms were reported in 1976 in a Λ scheme by Alzetta et al. [7], and independently in a cascade scheme by Gray et al. [8] in 1978. While the field of CPT has continued

to grow, its emphasis remains in manipulating and transferring atomic populations in coherent states. At the same time, other processes related to the trapping and optical properties of a three-level system coherently prepared were reported, such as lasing without inversion (LWI) [9, 10, 11], electromagnetically induced absorption (EIA) [12, 13], and electromagnetically induced transparency.

In 1990 Harris, Field and Imamoglu [14] used the term “electromagnetically induced transparency” for the first time, to describe a process to create a nonlinear medium with a resonant enhanced third-order susceptibility, while rendering the medium transparent at the same time. The first observation of EIT was in 1991 by Boller et al. [15] in a neutral strontium gas, where the transmittance of an ultraviolet autoionizing transition was changed from e^{-20} to e^{-1} by the addition of a coupling laser. This was followed by Field et al. [16] who reported EIT in a ladder scheme in collisionally broadened lead vapor, increasing the transmission of a resonance line by e^{10} . Since then the field of EIT has evolved in many directions.

In 1992 Harris’ group calculated the dispersive properties of an EIT prepared medium [17], by expanding the real and imaginary parts of the susceptibility in the spectral region around the transparency, and paving the way for the development of slow-light experiments. Indeed, in 1995 Kasapi et al. [18] reported the propagation dynamics in an EIT prepared Pb vapor, where pulse velocities as slow as $c/165$ were observed.

EIT has been used to enhance isotope discrimination [19], by making one isotope highly opaque and the other highly transparent to a probe. By this method, a signal of 0.03% from ^{207}Pb has been obtained against the correspondingly large background of ^{208}Pb .

Xiao’s group has done extensive research on an inhomogeneously broadened Rb gas in a Doppler-free configuration [20, 21, 22]. Among other things, by setting up a Mach-Zender interferometer they have measured the dispersion properties of an EIT system [23]. The optical bistability and instability have been studied for Rb atoms in a Λ scheme in an optical ring cavity [24]. They have achieved all-optical switching [25] by taking advantage of the enhanced Kerr nonlinearity of an EIT system; the intensity of a cavity field interacting with another transition is switched on and off by adjusting the frequency of the coupling field.

EIT has led to frequency conversion with enhanced efficiency [3, 26]. In conventional frequency mixing light will propagate through the medium, both at the

frequencies of the driving fields, and at the new frequencies given by their combinations. However, the near-resonant generated light may be reabsorbed by the medium. In EIT the medium is transparent, leading to enhanced optical frequency conversion, as has been observed by various groups [27, 28, 29, 30].

In 1999, Hau et al. [31] reported EIT in a sodium Bose-Einstein condensate. The combination of temperatures down to the nanokelvin scale, and high atomic density made possible the slowing down of laser pulses to a speed of 17 m/s, while the system displayed very large optical nonlinearities. Associated with the slow group velocities is the compression of the pulse as it enters the atomic-coupling field system, which allows for the possibility of long light pulses to be completely contained within the sample. The observation of light pulses completely contained, stopped or halted and reaccelerated in an ultracold cloud of Na atoms, was reported in 2001 [32, 33]. A vapor need not be cooled to ultracold temperatures to halt and regenerate light pulses within it, as was proved by Phillips in a Rb vapor cloud at temperatures of 70 – 90 °C [34].

The possibility to “halt and regenerate” or “store and retrieve” light was quickly linked to the field of quantum information, as EIT was identified as a tool to provide possible carriers in quantum information protocols [35, 36, 37]. Lukin et al. [38] discuss the possibility of entanglement of two or more atomic ensembles by storing entangled photon wave packets on separate atomic systems, opening interesting possibilities for information processing. Fleischhauer and Lukin associated a quantum excitation called a “dark-state polariton” with the propagation and storage of light in matter [39], and presented a polariton-based technique for transfer of quantum information [40]. In 2005, by converting single photons into dark-state polaritons, Chanelière et al. reported the storage and retrieval of single photons using two remote atomic ensembles as quantum memory nodes, separated by 100 m of optical fiber [41].

As can be seen, EIT has emerged as a powerful technique for controlling systems in a large variety of experiments. It can be foreseen that EIT-based research will continue to grow and find very interesting applications.

I.3 MOTIVATION

As was pointed out by Duan et al. [42], in a quantum communication protocol, the losses and decoherence in the quantum communication channel decrease the communication fidelity. Independently, in 2006 Datsyuk et al. [43] proposed that multiple scattering of light is one of the many mechanisms by which coherence loss takes place in an EIT-based system, but that the elastically scattered light maintains coherence with the forward propagating excitation, giving rise to a diffusely propagating polariton.

Multiple scattering as a coherence loss mechanism is the subject of this dissertation. In the ongoing effort towards quantum control of information in an EIT prepared medium, it becomes important to understand as much as possible the optical and atomic processes of the sample.

Ultracold atomic gases are promising media in which to study diffusion and multiple scattering. Atoms as scatterers of electromagnetic waves form well-controlled and characterized mono-disperse systems; well-defined atomic transition lines allow strongly resonant light scattering [44]. At the same time, considerable advances have been achieved in creating and controlling dilute gases of cold atoms with the use of lasers, which are coherent monochromatic light sources with well-defined phases, direction and polarization axes. Cold atomic vapors are suitable to study diffusion and EIT-based experiments because the Doppler broadening is greatly reduced, and the sample is therefore quasi-static. At the same time, the density of the sample may be controlled, so that broadening and coherence loss due to collisions becomes negligible.

The purpose of this research is to compare the forward and diffusely scattered light in a ^{87}Rb ultracold gas, under conditions of electromagnetically induced transparency. Toward this end, a magneto optical trap (MOT) of ^{87}Rb has been built, and the atomic vapor sample characterized in terms of atomic density, shape and size, temperature, and optical depth. Next, two co-propagating beams were sent through the sample, to establish a Λ -type EIT system. It should be mentioned that the two laser fields are not phase-locked, so ground state coherence will be affected by the lasers' phase fluctuations. Observation of the forward and diffusely scattered light were made for different conditions of probe pulse length, control field intensity, and probe frequency detuning. Storage and retrieval of pulses was achieved for the forward scattering (transmission) channel, but was not observed unambiguously in

the diffusely scattered (fluorescence) channel.

The remainder of this dissertation is organized in four chapters. Chapter II contains the theoretical background needed for understanding the development of EIT in a Rb ultracold gas. This includes the basic theory of laser cooling and trapping, some pertinent information about Rb, the basic theory of EIT, and a brief discussion of light diffusion. Chapter III presents the experimental setup, and the characterization of the Rb ultracold sample. The data acquisition setup and results are discussed in Chapter IV. The results are divided into measurements of transmission of a probe through the sample, and measurements of fluorescence, under similar conditions, from the probe. Finally, Chapter V presents the conclusions and future possible projects.

CHAPTER II

THEORETICAL BACKGROUND

This dissertation focuses on the differences between forward and diffuse propagation of light in an ultracold ^{87}Rb atomic cloud, which has been coherently prepared to exhibit electromagnetically induced transparency. The first section of this chapter presents the basic theory of laser cooling and trapping that leads to a magneto-optical trap (MOT). It is followed by a section on ^{87}Rb , and the relevant physical and optical properties to be considered when cooling and trapping it in a MOT. The third section of this chapter presents the basic theory of electromagnetically induced transparency (EIT). In the last section of this chapter, the relevance of diffusion in random media and the propagation of coherence in multiply scattered light will be briefly discussed.

II.1 LASER COOLING AND TRAPPING

The process of cooling atoms relies on the scattering force of a radiation field on the atoms. This dissipative force (also known as radiation pressure) is velocity dependent [45]. The atoms are considered to be colder when the average velocity of the atomic sample is reduced. In terms of the three-dimensional average kinetic energy E_k , the temperature T is given by:

$$\langle E_k \rangle = \frac{3k_B T}{2} = \frac{\langle p^2 \rangle}{2m}, \quad (4)$$

where k_B is Boltzmann's constant, and p and m are the atom's momentum and mass respectively [46, 47].

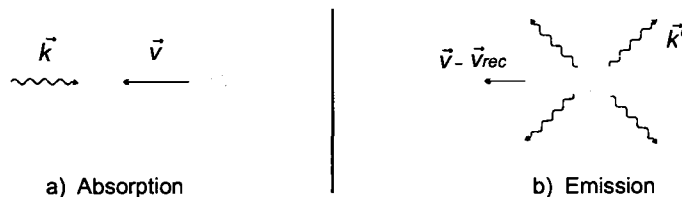


FIG. 2: Radiation pressure on an atom. The continuous absorption-emission cycle results in a decrease in the atom's velocity.

To understand how the radiation pressure can be controlled to cool or slow atoms, consider the one-dimensional system where an atom with mass m in the ground state is moving with a velocity v and a photon with wavenumber k is moving in the opposite direction, as in Fig. 2(a). The frequency of the light is nearly-resonant to an atomic transition. If the atom absorbs the photon, there will be a momentum transfer to the atom; since the photon carries momentum $\hbar k$, the atom will recoil with velocity $v_{rec} = \frac{\hbar k}{m}$ and consequently slow down. If the atom decays through a spontaneous emission of a fluorescence photon with wavenumber k' , the atom's momentum will change by $-\hbar k'$.

The average atomic momentum change is $\langle \Delta p \rangle = \langle \hbar k - \hbar k' \rangle$. However, spontaneous emission has the same probability in any two opposite directions, as in Fig. 2(b), so that $\hbar k'$ averages to zero. Thus, an atom in a radiation field undergoing multiple absorption-emission cycles has a net momentum change of $\langle \Delta p \rangle = \langle \hbar k \rangle$, and the atom's motion in the direction of the radiation field slows down.

The mean radiative force on an atom is given by the net momentum change times the rate γ_R at which the absorption-emission processes take place, also known as the scattering rate:

$$\vec{F} = \hbar \vec{k} \gamma_R, \quad (5)$$

$$\gamma_R = \frac{s_o(\frac{\Gamma_L}{2})}{\left(1 + s_o + 4(\frac{\Delta_L}{\Gamma_L})^2\right)}, \quad (6)$$

$$s_o = \frac{I}{I_s}. \quad (7)$$

In these equations s_o is the on-resonance saturation parameter, Γ_L is the atomic transition linewidth, Δ_L is the laser beam's frequency detuning from resonance, I is the intensity of the scattered laser beam, and I_s is the saturation intensity for the particular transition excited by the laser beam.

Thus, to dampen the velocity of an atom and confine it to a particular region in three-dimensional space, six counterpropagating laser beams in three mutually orthogonal directions may be used in what is commonly known as a three-dimensional optical molasses [48, 49, 50]. These beams are red-detuned from resonance, such that there is always a radiation force opposing the motion of atoms. Indeed, because of the Doppler effect, an atom moving in the $-\hat{x}$ direction as in Fig. 2(a) will be blue-shifted with respect to the light propagating in the $+\hat{x}$ direction; if said light is red-shifted, the frequency will be closer to the atomic resonance, and the atom will

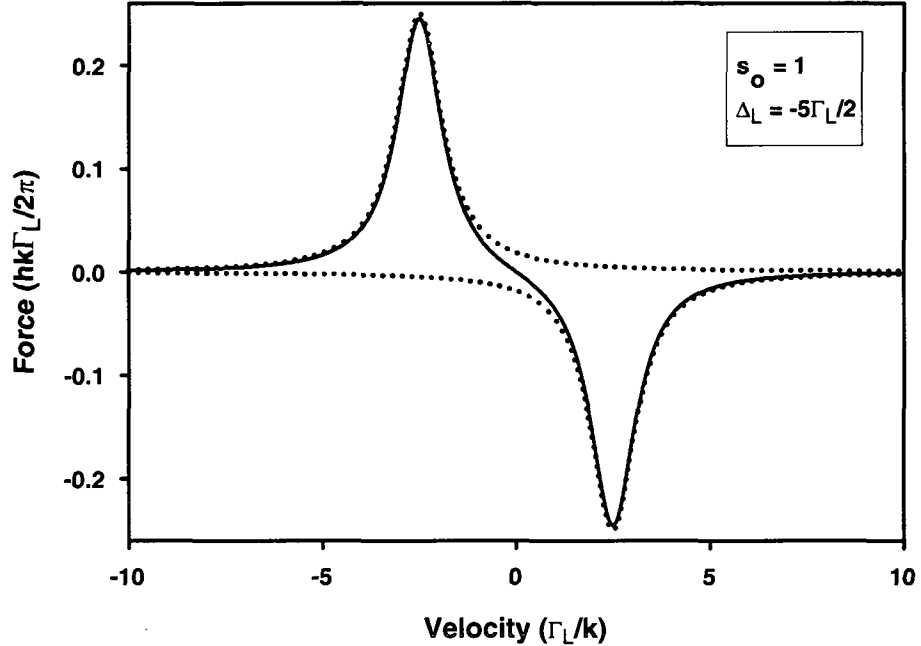


FIG. 3: Velocity dependent forces acting on an atom in a one-dimensional optical molasses. Shown in dotted lines are the forces from each laser beam, and the average force exerted on the atom is given by their sum, shown as a solid line. These forces are calculated for a saturation parameter of $s_o = 1$ and a laser detuning from resonance of $\Delta_L = -\frac{5}{2}\Gamma_L$.

be more likely to absorb photons. It also means that light propagating in the same direction as the atom, $-\hat{x}$, will be off-resonance, and less likely to interact with the atom. Because it relies on the Doppler effect, this process is also known as Doppler cooling.

Figure 3 illustrates the dampening effect of the velocity-dependent radiative forces for a one-dimensional optical molasses. For this case, the force acting on the atom will be given by the contribution of two forces as described in equations (5) and (6) with opposite \vec{k} , for a net force of:

$$\vec{F}_{net} = \hbar\vec{k}\gamma_{R+} + \hbar\vec{k}\gamma_{R-} \simeq \frac{8\hbar k^2 \Delta_L s_o \vec{v}}{\Gamma \left(1 + s_o + 4(\Delta_L/\Gamma_L)^2\right)^2} = -\kappa \vec{v}, \quad (8)$$

where κ is a damping coefficient. Shown are the individual and combined forces for a saturation parameter of $s_o = 1$ and a laser detuning from resonance of $\Delta_L = -\frac{5}{2}\Gamma_L$. As can be seen, regardless of the direction in which the atom is moving there is a net

viscous force centered around $v = 0$. As this effect extends to a three-dimensional situation the atoms can be slowed down in the center of the molasses. The atoms, however, cannot be stopped; the smallest velocity they can have is the recoil velocity v_{rec} . The energy change of a single-photon recoil associated with a single photon absorption and emission process can be related to a recoil limit temperature $T_R = \frac{\hbar^2 k^2}{k_B m}$.

Cooling of atoms in a MOT beyond the Doppler limit temperature is possible, as was found by Lett et al. in 1988 [51] and rapidly confirmed and explained by others, [52, 53, 54, 55]. Sub-Doppler cooling occurs in a three-dimensional optical molasses because of the multilevel structure of the atoms, optical pumping, and the spatial variation of the laser field polarization; it is also known as polarization gradient cooling. Atoms in a ground state have orientations due to the different populations in the different ground-state sublevels. In the presence of polarization gradients, moving atoms will try to compensate in a non-adiabatic way for the changing light field via optical pumping, as was explained by Dalibard and Cohen-Tanoudji [52].

As a near-resonant light field interacts with a atom possessing multiple ground-state Zeeman sublevels, two processes can occur: optical pumping between the sublevels, and light shifts. Optical pumping is a process by which a change of population between atomic sublevels occurs via absorption/emission of light. As an example, consider an atom with ground state angular momentum $J_g = \frac{1}{2}$, and an excited state angular momentum $J_e = \frac{3}{2}$, as shown in Fig. 4(a). The transition probabilities between the energy levels of an atom with angular momentum along the z quantization axis are described by the square of the appropriate Clebsch-Gordan coefficients coupling the atom and the light field, shown for each transition. It is clear that for a particular light field polarization some transitions will be driven more strongly than others. Consider, for example, atoms interacting with σ_+ polarized light, red-detuned as in most Doppler-cooling experiments, which can only drive transitions where $\Delta m = +1$. If the atom is found in the $g_{+1/2}$ ground-state sublevel, it will be excited to the $e_{+3/2}$ excited state sublevel and can only decay via spontaneous emission back to $g_{+1/2}$. However, an atom in the $g_{-1/2}$ ground-state sublevel is only $\frac{1}{3}$ as likely to be excited to $e_{+1/2}$ sublevel; once excited it can decay by spontaneous emission and the probability for decaying to $g_{+1/2}$ is $\frac{2}{3}$ compared to $\frac{1}{3}$ for decay back into the $g_{+1/2}$ sublevel. Thus, after several absorption/emission cycles the atomic population is redistributed or optically pumped into the $g_{+1/2}$ sublevel.

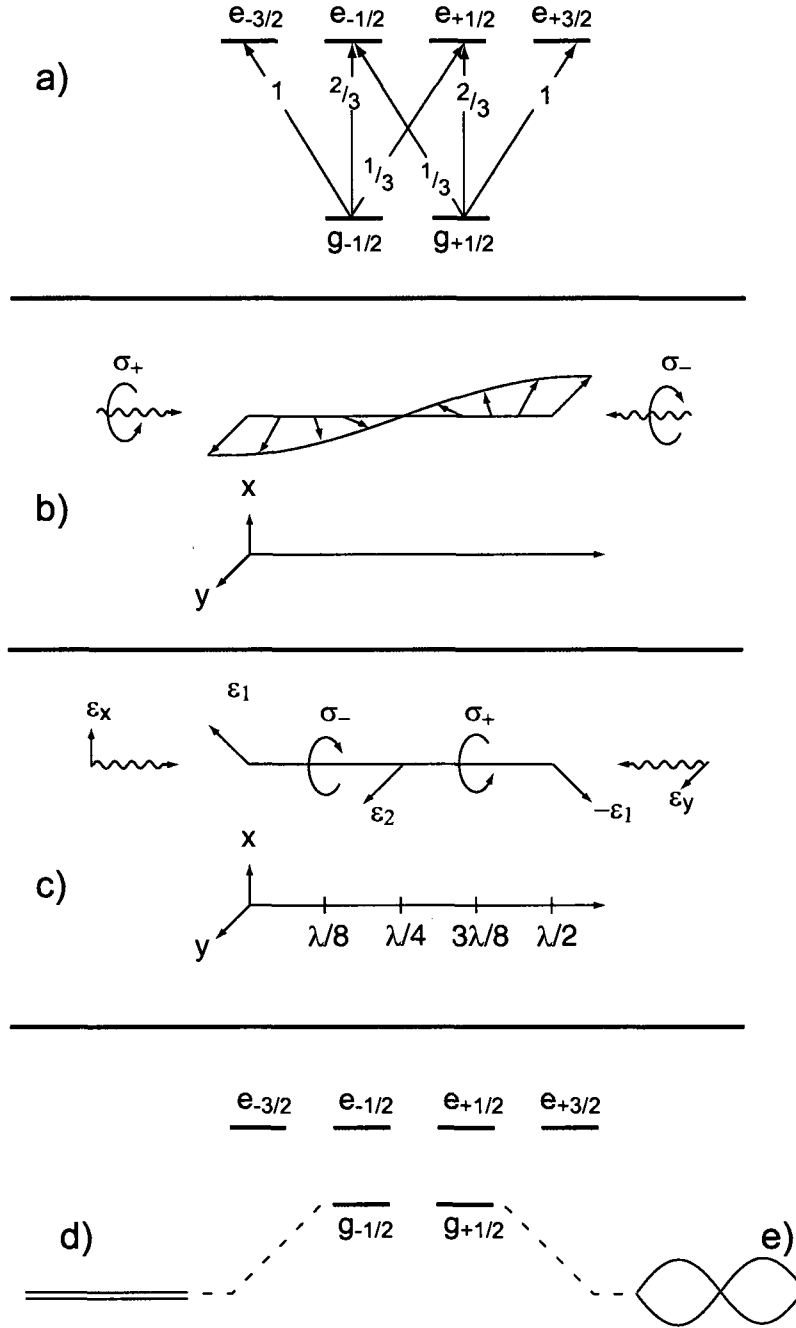


FIG. 4: Components of polarization gradient cooling. It relies on optical pumping between the multiple levels of the atom's ground state, polarization gradients induced by two counterpropagating laser beams with orthogonal polarization, and light shifts. (a) Atomic level structure and square Clebsch-Gordan coefficients for a $J_g = \frac{1}{2} \rightarrow J_e = \frac{3}{2}$ transition. (b) Polarization gradient for a $\sigma_+ - \sigma_-$ configuration. (c) Polarization gradient for a $\text{lin} \perp \text{lin}$ configuration. (d) Light shifted ground sublevels for the $\text{lin} \perp \text{lin}$ configuration. (e) Light shifted ground sublevels for the $\sigma_+ - \sigma_-$ configuration.

The light shift for the Zeeman sublevels due to two laser beams with intensity $s_o I_s$, given by Eq. (7), in the low-intensity limit is given by [46]:

$$\delta E_g = \frac{\hbar \Delta_L s_o C_{ge}^2}{1 + 4(\Delta_L/\Gamma_L)^2}, \quad (9)$$

where Δ_L is the laser frequency detuning from the atomic resonance, C_{ge}^2 are the appropriate Clebsch-Gordan coefficients and Γ_L is the transition linewidth. Continuing with the example of atoms interacting with σ_+ polarized light, it can be seen by the Clebsch-Gordan coefficients that while both ground-state sublevels will have energy shifts, the $g_{+1/2}$ will be three times larger than the shift for $g_{-1/2}$.

Therefore, it can be seen that the polarization of the light field (and polarization gradients) should be taken into account in the discussion of multilevel atoms. For simplicity, consider one-dimensional polarization gradients, where there are two counterpropagating laser beams with orthogonal polarization. The electric field due to two counterpropagating beams along the z -direction with the same intensity and wavelength is given by:

$$\vec{E}(z, t) = \vec{E}_o(z)e^{-i\omega t} + \vec{E}_o^*(z)e^{i\omega t}, \quad (10)$$

$$\vec{E}_o(z) = E_o(\hat{e}_+ e^{ikz} + \hat{e}_- e^{-ikz}). \quad (11)$$

where \hat{e}_+ and \hat{e}_- are the polarization vectors of the counterpropagating plane waves.

It can be seen that these beams produce a standing wave whose polarization varies in space. In one possible scheme, the beams have mutually orthogonal circular polarizations ($\sigma_+ - \sigma_-$); for this case the polarization vector along the standing wave will rotate, but the magnitude remains the same; this is illustrated in Fig. 4(b). As the polarization is linear and the laser intensity is the same along the standing wave, the ground-state sublevels are shifted by an equal amount, and do not vary along z , as shown in Fig. 4(d). For atoms at rest, the population distribution in the ground state sublevels will reflect the local light field polarization. However, for moving atoms the quantization axis rotates, and the ground state population changes via optical pumping (an energy-dissipative effect) in order to follow it. Because this cooling effect relies on the ground-state atomic orientation, it only works for atoms where the ground-state is $J_g \geq 1$.

In another scheme, the beams have mutually orthogonal linear polarizations (lin \perp lin); for this case the ellipticity of the laser polarization changes along the standing wave, as is illustrated in Fig. 4(c). In this case, the ground-state light-shifted Zeeman

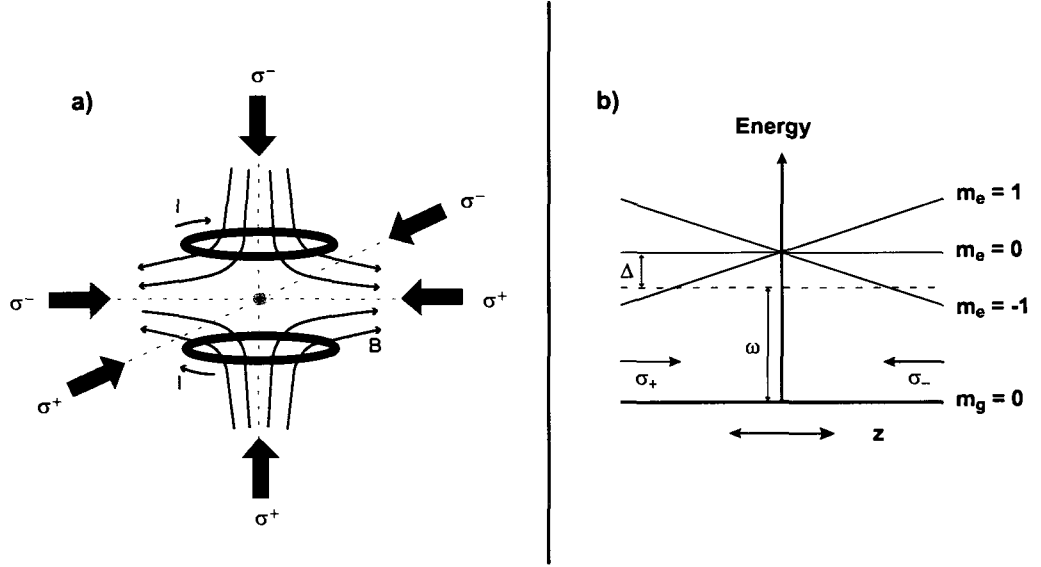


FIG. 5: Trapping atoms in a magneto-optical trap. (a) An inhomogeneous magnetic field produced by an Anti-Helmholtz coil pair; $|B|=0$ at the center of the molasses. (b) Illustration of the Zeeman energy shift induced by the position-dependent magnetic field.

sublevels will oscillate along the standing wave, with a period of $\lambda/2$, as shown in Fig. 4(e). For atoms at rest, the energies and population of ground-state sublevels depend on the position along z . For atoms moving along z , because there is a time lag between the optical pumping process and the atomic motion, the atoms at the bottom of an energy valley will remain in the same sublevel as the atom moves, thus climbing the potential hill. If the velocity is such that the atoms move a distance on the order of $\lambda/4$ when the next absorption event occurs, then upon emission they will be optically pumped to the next potential energy valley, thus losing some kinetic energy on the process. Because it appears that atoms are continuously climbing potential hills, this type of cooling is also known as “Sisyphus cooling,” after the Greek myth where a king was cursed to roll a boulder up a hill eternally.

Although the atoms have now been slowed down and cooled in the center of the molasses, they are by no means trapped; once the atoms have small enough velocities they can diffuse and creep away from the center of the molasses. To trap the atoms, a position-dependent force is needed. By introducing a magnetic field gradient, the radiation force becomes position-dependent.

A magneto optical trap relies on an inhomogeneous magnetic field, such as the quadrupole field induced by a set of coils conducting opposite currents, and the Zeeman structure of the atoms. Figure 5(a) shows the magnetic \vec{B} field lines which run parallel to the axes defined by the counterpropagating radiation fields; the magnetic field at the center is $|B| = 0$, and its magnitude increases in all directions. To illustrate how the radiation force becomes position-dependent, consider the simple case of an atom in a ground state $J_g = 0$ ($m_g = 0$) and an excited state $J_e = 1$ ($m_e = \pm 1, 0$). This atom may interact with light from two counterpropagating laser beams, which have circular polarization σ_+ and σ_- along the z -axis. Recall that the field lines run parallel to the axes defined by the radiation fields, so we may assume the presence of a magnetic field that can be described, to a first approximation, as $B_z = B_0 z$. The Zeeman levels will consequently be split by $\Delta E_{mF} = \mu m_e$, as illustrated in Fig. 5(b). If, as in a magneto optical trap, the light is red-detuned with respect to the atomic resonance, then an atom moving in the $+\hat{z}$ direction will be closer to resonance with the $m_e = -1$ transition, and will more readily interact with the σ_- beam than with the σ_+ beam. Likewise, an atom moving in the $-\hat{z}$ direction will more readily interact with the σ_+ beam. The net effect is a force pushing the atom towards $z = 0$.

For three-dimensional trapping, counterpropagating radiation beams are added along the x and y axes, as shown in Fig. 5(a). This scheme works for any atoms where $J_e = J_g + 1$.

Thus, a magneto optical trap (MOT) relies on the radiative force to dampen atoms in velocity space, and on the radiative pressure selection rules in the presence of a magnetic field gradient to dampen the motion in position space.

More comprehensive and thorough discussions on the theory of laser cooling and trapping can be found in [45, 46, 56], while [57] contains technical details and instructions for assembling a magneto optical trap.

II.2 ⁸⁷RUBIDIUM

⁸⁷Rb was chosen for the present experiment for several reasons. First, it is an alkali-metal, which have excitation frequencies in the visible or near-infrared regime that can be accessible by relatively inexpensive commercial lasers. Second, it has a closed shell with a single valence electron and it alone contributes to the total electronic angular momentum \vec{J} of the atom; these two conditions are important for cooling cycling transitions. Third, it has a large vapor pressure at temperatures of a few

TABLE 1: Physical properties of ^{87}Rb .

Rubidium 87 Property	Value
Atomic Number	37
Nucleons	87
Atomic Mass	$1.443\,160\,648(72) * 10^{-25} \text{ kg}$
Nuclear Spin	$I = 3/2$
Density at 25 °C	1.53 g/cm^3
Vapor Pressure at 25 °C	$3.92(20) * 10^{-7} \text{ torr}$

hundred °C, easily achievable in the lab. And fourth, several components of the equipment necessary for building a ^{87}Rb MOT were already in the laboratory. For a good compilation of ^{87}Rb data see Ref. [58].

Naturally occurring rubidium has two isotopes, a stable one (^{85}Rb), and a radioactive one (^{87}Rb), with an abundance ratio of 72.2% to 27.8%. The lifetime of ^{87}Rb is roughly 49 billion years, so it is considered to be quite stable. Table 1 lists some important physical properties of ^{87}Rb .

Using the Russell-Saunders notation $n^{(2S+1)}L_J$ (where n is the principal quantum number of the valence electron, S is the spin angular momentum, L is the orbital angular momentum where $L = 0$ is called the S orbital and $L = 1$ is called a P orbital, and $J = L + S$ is the total angular momentum of the electron), then the ground state of ^{87}Rb is $5^2\text{S}_{1/2}$. For the first excited states, the angular momentum $L = 1$ can couple with the spin momentum S to form the $5^2\text{P}_{1/2}$ state and a $5^2\text{P}_{3/2}$ state; the optical transitions from the ground state to these levels are referred to as the D1 and D2 lines respectively. Coupling J with the nuclear angular momentum I results in the atomic angular momentum F , giving rise to a hyperfine structure.

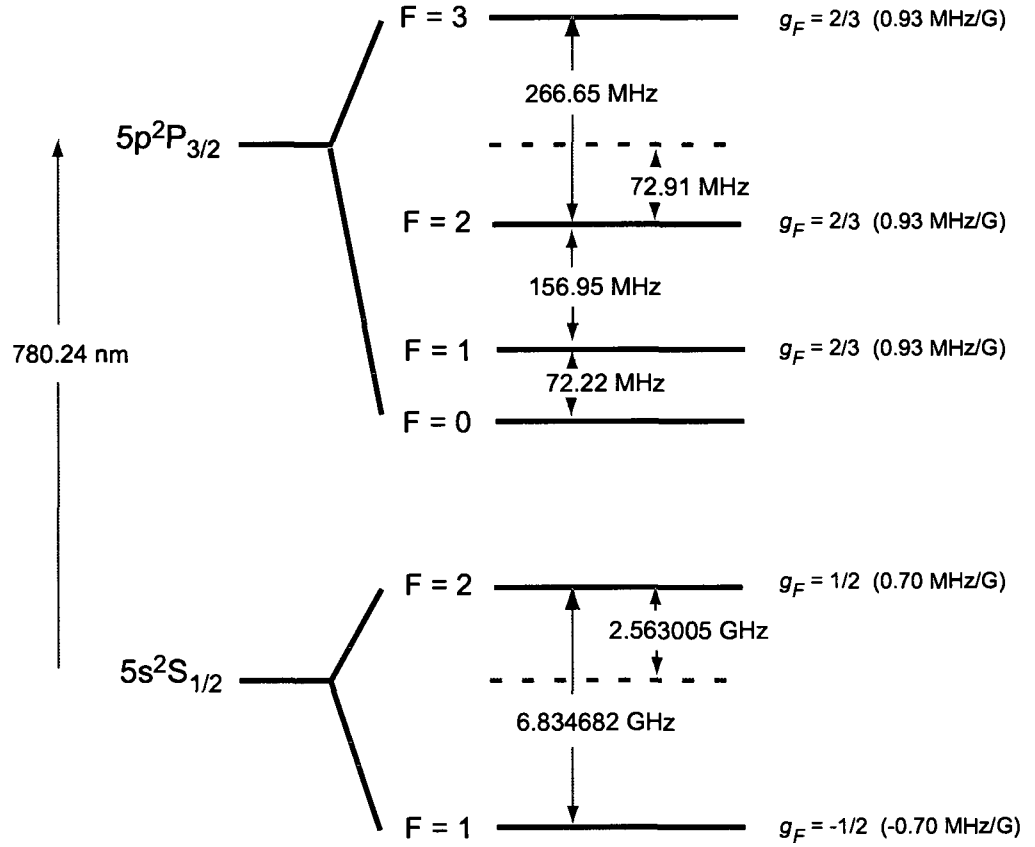


FIG. 6: Rubidium 87 transition energy diagram for the D2 line [58]. The relative spacing between energy levels is not to scale. The frequency splittings between the hyperfine energy levels are shown. Included also are the approximate values of the g_F factor for each level, and Zeeman splittings between contiguous sublevels.

TABLE 2: ^{87}Rb D2 ($5^2\text{S}_{1/2} \rightarrow 5^2\text{P}_{3/2}$) transition optical properties.

Optical Property	Symbol	Value
Frequency	ω_o	$2 \pi \cdot 384.230\,484\,468\,5(62)$ THz
Wavelength in vacuum	λ	$780.241\,209\,686(13)$ nm
Lifetime	τ	$26.2348(77)$ ns
Natural Linewidth	Γ_L	$2 \pi \cdot 6.0666(18)$ MHz

For the present experiment the relevant structure is that of the D2 line ($5^2\text{S}_{1/2} \rightarrow 5^2\text{P}_{3/2}$ transition) which is illustrated in Fig. 6; included are the frequency splittings between the hyperfine energy levels.

In the presence of a weak magnetic field B_z along the atomic quantization axis z , the hyperfine levels split into the Zeeman sublevels and are energy-shifted by an amount $\Delta E_{m_F} = \mu_B g_F m_F B_z$, where μ_B is the Bohr magneton, g_F is the Landè g_F factor, and m_F is the hyperfine sublevel. Figure 6 includes the approximate values for each level of the g_F factor, and Zeeman splittings between contiguous magnetic sublevels.

For the realization of a ^{87}Rb MOT in the D2 $5^2\text{S}_{1/2} \rightarrow 5^2\text{P}_{3/2}$ transition, the relevant optical properties are listed in Table 2.

II.3 ELECTROMAGNETICALLY INDUCED TRANSPARENCY

Electromagnetically induced transparency arises from the quantum interference of a three level atom induced by the presence of two different radiation fields, as will be explained later. Before plunging into a discussion of the three-level atom under conditions of EIT, a review of the two-level atom is recommended, and presented in Appendix A.

In the first part of this section, it is shown that when a three-level atom, with two stable ground states and one excited state, is in the presence of two electromagnetic fields which may independently couple the atom to the excited state, the atom may evolve into a “dark” state. The dark state is a coherent superposition of the ground states, for which absorption is inhibited. In the second part of this section the optical properties of such a coherently prepared medium are examined.

II.3.1 THE IDEAL THREE-LEVEL ATOM

Consider an ideal three-level atom at rest, in a Λ configuration, such that it has two lower ground energy states $|1\rangle$ and $|2\rangle$ (with the same parity, so they cannot couple via the electric dipole interaction), and an excited state $|3\rangle$ of opposite parity. The unperturbed atom satisfies the following equations:

$$\hat{H}_o|k\rangle = E_k|k\rangle, \quad \langle n|k\rangle = \delta_{nk}, \quad (12)$$

$$\hat{H}|\psi(t)\rangle = \hat{H}_o|\psi(t)\rangle = i\hbar\frac{\partial}{\partial t}|\psi\rangle, \quad (13)$$

$$|\psi(t)\rangle = \sum_k a_k(t)|k\rangle e^{-i\omega_k t}, \quad (14)$$

$$a_k(t) = \langle k|\psi(t)\rangle, \quad P_k(t) = |a_k(t)|^2. \quad (15)$$

Here, $|k\rangle$ are the eigenstates (also known as the bare states) of the unperturbed Hamiltonian \hat{H}_o with eigenvalues $E_k = \hbar\omega_k$, $|\psi(t)\rangle$ is the atomic wave function, $a_k(t)$ is a probability amplitude and $P_k(t)$ is the probability of the atom to be in the state $|k\rangle$ at a time t .

The resonant transition frequency between states is given by

$$\omega_{ij} = \omega_i - \omega_j. \quad (16)$$

This three-level atom is in the presence of two near-resonant monochromatic laser fields, as in Fig. 7. One of them is a weak probe field with a frequency ω_p , which it is assumed may only couple the $|1\rangle$ and $|3\rangle$ states via the electric dipole interaction, and which is detuned from the ω_{31} resonant frequency by an amount

$$\Delta_p = \omega_p - \omega_{31}. \quad (17)$$

The second is a strong field, (it may be referred to as the coupling or control laser) with a frequency ω_c , which is near-resonant with the $|2\rangle$ and $|3\rangle$ atomic transition

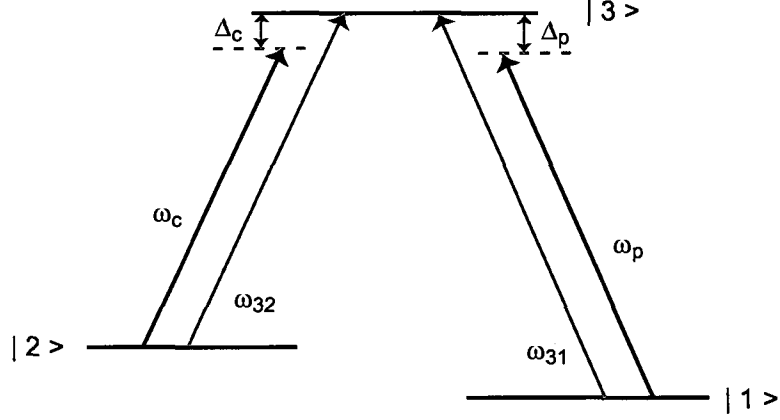


FIG. 7: The three-level atom in a Λ scheme, in the presence of two classical electromagnetic fields. The three level atom has two lower states $|1\rangle$ and $|2\rangle$ which may be coupled to an upper state $|3\rangle$ via the electric dipole operator. The $|1\rangle \rightarrow |3\rangle$ transition has a resonant frequency ω_{31} . The $|2\rangle \rightarrow |3\rangle$ transition has a resonant frequency ω_{32} . The atom is in the presence of two classical electromagnetic fields, a strong “coupling” field with frequency ω_c detuned by an amount Δ_c from the ω_{32} resonant transition frequency, and a weak “probe” field with frequency ω_p detuned by an amount Δ_p from the ω_{31} resonant frequency.

(but it is assumed it does not couple other states), and is frequency detuned from resonance by

$$\Delta_c = \omega_c - \omega_{32}. \quad (18)$$

Using the electric dipole approximation, it is assumed that the wavelength of the fields is much larger than the size of the atom, so that the spatial variations of the electric field can be neglected. With this approximation, the probe and control beams can be described respectively by:

$$\vec{E}_p(t) = E_p \hat{\epsilon}_p \cos(\omega_p t) = \frac{E_p}{2} \left(e^{-i\omega_p t} + e^{i\omega_p t} \right), \quad (19)$$

$$\vec{E}_c(t) = E_c \hat{\epsilon}_c \cos(\omega_c t) = \frac{E_c}{2} \left(e^{-i\omega_c t} + e^{i\omega_c t} \right), \quad (20)$$

where $\hat{\epsilon}_p$ is the probe field polarization vector, and $\hat{\epsilon}_c$ is the control field polarization vector.

In the presence of these fields, the Hamiltonian of the system becomes

$$\hat{H} = \hat{H}_o + \hat{V}_p + \hat{V}_c, \quad (21)$$

$$\hat{V}_p = q\vec{E}_p(t) \cdot \vec{r}, \quad (22)$$

$$\hat{V}_c = q\vec{E}_c(t) \cdot \vec{r}, \quad (23)$$

where \hat{V}_p is the operator driving the transition between the $|1\rangle$ and $|3\rangle$ states, and \hat{V}_c drives the transition between the $|2\rangle$ and $|3\rangle$ states. The Schrödinger's equation may be rewritten as

$$|\dot{\psi}(t)\rangle = \sum_k \dot{a}_k |k\rangle e^{-i\omega_k t} - \sum_k a_k i\omega_k |k\rangle e^{-i\omega_k t}, \quad (24)$$

$$|\dot{\psi}(t)\rangle = \frac{1}{i\hbar} \left(\sum_k \hbar\omega_k |k\rangle + \sum_k a_k \hat{V}_p |k\rangle e^{-i\omega_k t} + \sum_k a_k \hat{V}_c |k\rangle e^{-i\omega_k t} \right). \quad (25)$$

Multiplying on the left by $\langle n|$ and applying the orthogonality conditions the following equations are obtained for the three-level atom:

$$\dot{a}_1 = \frac{1}{i\hbar} a_3 \langle 1|\hat{V}_p|3\rangle e^{-i\omega_{31}t}, \quad (26)$$

$$\dot{a}_2 = \frac{1}{i\hbar} a_3 \langle 2|\hat{V}_c|3\rangle e^{-i\omega_{32}t}, \quad (27)$$

$$\dot{a}_3 = \frac{1}{i\hbar} \left(a_1 \langle 3|\hat{V}_p|1\rangle e^{i\omega_{31}t} + a_2 \langle 3|\hat{V}_c|2\rangle e^{i\omega_{32}t} \right). \quad (28)$$

Substituting the dipole operators, Eq. (22) and (23), into these equations will yield fast oscillatory terms of the order $e^{\pm i(\omega+\omega_{31})}$ and $e^{\pm i(\omega+\omega_{32})}$. These terms may be replaced by their zero average value by using the rotating-wave approximation (RWA) which focuses on the slow dynamics of a system.

The coupling between an atom and a radiation field is characterized by the Rabi frequency defined in terms of the magnitude of the electric field and the dipole transition matrix element. For this particular case

$$\Omega_p = \frac{qE_p}{\hbar} \langle 3|\hat{\epsilon}_p \cdot \vec{r}|1\rangle, \quad (29)$$

$$\Omega_c = \frac{qE_c}{\hbar} \langle 3|\hat{\epsilon}_c \cdot \vec{r}|2\rangle, \quad (30)$$

Ω_p and Ω_c are the probe and control Rabi frequencies respectively.

Putting all these equations together, after the RWA, the following three coupled differential equations for the probability amplitudes of the states are obtained:

$$\dot{a}_1 = \frac{a_3}{2i} \Omega_p^* e^{i\Delta_p t}, \quad (31)$$

$$\dot{a}_2 = \frac{a_3}{2i} \Omega_c^* e^{i\Delta_c t}, \quad (32)$$

$$\dot{a}_3 = \frac{1}{2i} \left(a_1 \Omega_p e^{-i\Delta_p t} + a_2 \Omega_c e^{-i\Delta_c t} \right). \quad (33)$$

Now we find the steady state solution of these equations. As initial conditions assume that at time $t = 0$ the atom is not excited, so that $a_3(0) = 0$ and that the probability of finding the atom in the ground states is 1,

$$\dot{a}_3 = 0 \implies a_1 = -\frac{a_2 \Omega_c}{\Omega_p}, \quad |a_1|^2 + |a_2|^2 = 1, \quad (34)$$

by solving these equations it is found that the atom has evolved into the state

$$|\psi\rangle = \frac{\Omega_c}{\Omega} |1\rangle e^{-i\omega_1 t} - \frac{\Omega_p}{\Omega} |2\rangle e^{-i\omega_2 t}, \quad (35)$$

where

$$\Omega = \sqrt{|\Omega_p|^2 + |\Omega_c|^2}. \quad (36)$$

It is interesting to note that the system has evolved into a coherent superposition of the ground states. Indeed, when $\Delta_p = \Delta_c = 0$, two of the three eigenstates of the total Hamiltonian will be symmetric and antisymmetric coherent superpositions of the two ground states [2]:

$$|C\rangle = \frac{\Omega_p}{\Omega} |1\rangle + \frac{\Omega_c}{\Omega} |2\rangle, \quad (37)$$

$$|NC\rangle = \frac{\Omega_c}{\Omega} |1\rangle - \frac{\Omega_p}{\Omega} |2\rangle. \quad (38)$$

The electric dipole interaction may couple the eigenstate $|C\rangle$ to the excited state $|3\rangle$, but it will not couple the eigenstate $|NC\rangle$, that is, once the atom evolves into that state it ceases to interact with the electric fields, and there are no additional processes that may take the atom out of this state. For this reason, $|C\rangle$ is called a “bright” state, while $|NC\rangle$ is called a “dark” or “trapped” state. This is the basis of coherent population trapping (CPT), where the atomic population may be driven to the dark state by balancing Ω_p and Ω_c , and becoming trapped in this coherent state. It is clear that since the atoms will not be excited to the upper state, they become “transparent” to the electric fields.

Another representation of the dark state is given in terms of a mixing angle Θ , such that

$$|NC\rangle = \cos \Theta |1\rangle - \sin \Theta |2\rangle, \quad (39)$$

$$\tan \Theta = \frac{\Omega_p}{\Omega_c}. \quad (40)$$

The atomic populations are given by the square probability amplitudes $|a_1|^2 = \cos^2 \Theta = \Omega_c^2 / (\Omega_p^2 + \Omega_c^2)$, $|a_2|^2 = \sin^2 \Theta = \Omega_p^2 / (\Omega_p^2 + \Omega_c^2)$, $|a_3|^2 = 0$ [59]. It is important

to notice that in the absence of a probe field ($\Omega_p = 0$), the dark state corresponds to the bare state $|1\rangle$ when the coupling field is on. Likewise, the dark state may correspond to the bare state $|2\rangle$ for $\Theta = \frac{\pi}{2}$. If the Rabi frequencies change adiabatically (slowly enough in time) then the non-coupling state described by $|NC\rangle$ has time to adjust to the changing Rabi frequencies by changing the mixing angle Θ .

Thus, by adjusting slowly the ratio of the control and probe field intensities, the atomic population may be coherently transferred from one bare state to the other, or to a coherent superposition of states. This process is called coherent population transfer; since it does not involve spontaneous emission, it is a very efficient way of transferring population between the atomic states. The condition for adiabatic evolution is that, as the ratio of the control and field Rabi frequencies changes, the dark state should be able to follow the rotation of the angle Θ . For the case when $\Delta_p = \Delta_c = 0$, the condition for adiabaticity reduces to [26, 59]

$$\Omega(t) = \sqrt{\Omega_p^2(t) + \Omega_c^2(t)} \gg |\dot{\Theta}|. \quad (41)$$

In the context of this dissertation, a coherently prepared medium is a medium in which the atoms have been driven into a coherent superposition of their ground states, particularly the dark state. EIT is a phenomenon related to CPT, for the case when $\Omega_p \ll \Omega_c$. Thinking in terms of the bare states, the strong coupling beam drives the atomic population to the $|1\rangle$ ground state through the process of optical pumping. In this way, the atoms are prepared in the dark state that coincides with $|1\rangle$ in the absence of the probe field. When the probe field is turned on the dark state rotates through the angle Θ , and after reaching a steady state the atoms cease to “see” or interact with the coupling field. The atom may still be excited through the interaction with \vec{E}_p , even though Ω_p is very small. However, the amplitude to be in the excited state may arise from different excitation pathways, through $|1\rangle \rightarrow |3\rangle$, or more indirect pathways such as $|1\rangle \rightarrow |3\rangle \rightarrow |2\rangle \rightarrow |3\rangle$. Since the intensity of the control field is much larger than that of the probe field, the indirect pathways have a probability amplitude as large as that of the direct route to excitation, and in fact interfere destructively, suppressing absorption [2]. Thus the atomic medium becomes transparent to the probe field. EIT is a process by which an otherwise optically thick medium becomes transparent, and it arises from externally induced quantum mechanical coherence and interference within the atoms.

II.3.2 OPTICAL PROPERTIES OF AN EIT PREPARED MEDIUM

In an atomic ensemble, the coherences in the system are identified by the off-diagonal elements ρ_{ij} of the density matrix $\hat{\rho}$ defined as

$$\hat{\rho} = \sum_n W_n |\psi_n\rangle \langle \psi_n|, \quad (42)$$

$$\rho_{ij} = \sum_n W_n a_{in} a_{jn}^*, \quad (43)$$

where a_{in} describes the probability amplitude for the n atom to be in the state $|\psi_i\rangle$, and ρ_{ii} is the population of the ensemble which is in a state $|\psi_i\rangle$ (See Appendix A). The time evolution of the density matrix is given by the Liouville equation

$$\dot{\hat{\rho}} = \frac{1}{i\hbar} [\hat{H}, \hat{\rho}]. \quad (44)$$

So far no relaxation processes have been included in the three-level atom description in the presence of two classical plane waves. It is clear, however, that relaxation processes play an important role, as can be seen by considering Eqs. (37) and (38), the eigenstates of the full Hamiltonian mentioned above. Since atoms in the bright state continue to be excited by the electric fields, simple spontaneous emission will eventually transfer all the atomic population to the dark or trapped state. Spontaneous emission, collision broadening, and coherence decays can be included in the time-dependent density matrix equations by adding a relaxation matrix Γ' to the Liouville equation

$$\langle n | \hat{\Gamma}' | m \rangle = \Gamma_n \delta_{nm}, \quad (45)$$

$$\dot{\hat{\rho}} = \frac{1}{i\hbar} [\hat{H}, \hat{\rho}] - \frac{1}{2} \{ \hat{\Gamma}' \hat{\rho} \}, \quad (46)$$

The equations of motion for the off-diagonal elements of the density matrix are given by [20]:

$$\rho_{31} = \tilde{\rho}_{31} e^{-i\Delta_p t}, \quad (47)$$

$$\rho_{32} = \tilde{\rho}_{32} e^{-i\Delta_c t}, \quad (48)$$

$$\rho_{21} = \tilde{\rho}_{21} e^{i(\Delta_c - \Delta_p)t}, \quad (49)$$

$$\dot{\tilde{\rho}}_{31} = (i\Delta_p - \Gamma) \tilde{\rho}_{31} + \frac{i\Omega_p}{2} (\tilde{\rho}_{33} - \tilde{\rho}_{11}) - \frac{i\Omega_c}{2} \tilde{\rho}_{21}, \quad (50)$$

$$\dot{\tilde{\rho}}_{32} = (i\Delta_c - \Gamma) \tilde{\rho}_{32} + \frac{i\Omega_c}{2} (\tilde{\rho}_{33} - \tilde{\rho}_{22}) - \frac{i\Omega_p}{2} \tilde{\rho}_{21}^*, \quad (51)$$

$$\dot{\tilde{\rho}}_{21} = \left(i(\Delta_p - \Delta_c) - \Gamma_g \right) \tilde{\rho}_{21} - \frac{i\Omega_c^*}{2} \tilde{\rho}_{31} + \frac{i\Omega_p}{2} \tilde{\rho}_{23}^*. \quad (52)$$

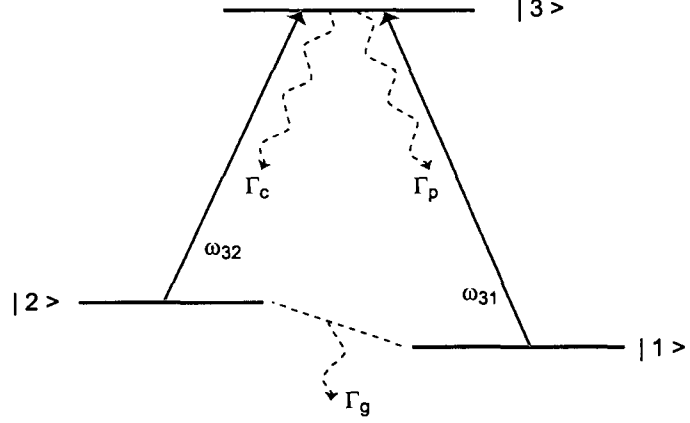


FIG. 8: The three-level atom in a Λ scheme, including relaxation rates. The three level atom has two lower states $|1\rangle$ and $|2\rangle$ which may be coupled to an upper state $|3\rangle$ via the electric dipole operator. The $|1\rangle \rightarrow |3\rangle$ transition has a resonant frequency ω_{31} , with a spontaneous decay rate Γ_p . The $|2\rangle \rightarrow |3\rangle$ transition has a resonant frequency ω_{32} , with a spontaneous decay rate Γ_c . Γ_g is a nonradiative decay rate between the two lower ground states.

where $\Gamma = (\Gamma_p + \Gamma_c + \Gamma_g)/2$; Γ_p is the spontaneous decay rate from the excited state $|3\rangle$ to the ground state $|1\rangle$, Γ_c is the spontaneous decay rate from the excited state $|3\rangle$ to $|2\rangle$, and Γ_g is the nonradiative decay rate between the two ground states (see Fig. 8).

To learn how the presence of the strong coupling laser changes the optical properties of the atomic gas of density ϱ , it is necessary to calculate the polarization generated as the medium is probed by the much weaker field \vec{E}_p . It is assumed that the control field has been turned on for a sufficiently long time to optically pump all the atoms to the $|1\rangle$ state, so that no more excitations occur due to the presence of the strong field. Under these conditions, the polarization due to the probe field is

$$P(t) = \varrho \langle \vec{p} \rangle_p = -q \left(\rho_{31} \langle 1 | \hat{\epsilon}_p \cdot \vec{r} | 3 \rangle e^{-i\omega_{31}t} + \rho_{13} \langle 3 | \hat{\epsilon}_p \cdot \vec{r} | 1 \rangle e^{i\omega_{31}t} \right), \quad (53)$$

$$P(t) = \frac{-\varrho \hbar}{E_p} \left(\tilde{\rho}_{31} \Omega_p^* e^{-i\omega_p t} + \tilde{\rho}_{13} \Omega_p e^{i\omega_p t} \right). \quad (54)$$

The polarization may also be expressed in terms of the complex linear susceptibility $\chi(\omega)$ defined such that:

$$P(t) = \frac{\epsilon_o E_o}{2} \left(\chi(\omega) e^{-i\omega t} + \chi(-\omega) e^{i\omega t} \right). \quad (55)$$

In steady state $\dot{\rho}_{ij} = 0$. To find the solution of the density matrix equations of motion, assume that the probe field is very weak, so $\Omega_p \ll \Omega_c$, and the atoms remain mostly on the $|1\rangle$ ground state so $\rho_{11} \simeq 1$, $\rho_{22} \simeq \rho_{33} \simeq 0$. Then the relevant matrix element is found to be

$$\tilde{\rho}_{31} = \frac{-i\Omega_p/2}{\Gamma - i\Delta_p + \frac{|\Omega_c|^2/4}{\Gamma_g - i(\Delta_p - \Delta_c)}}, \quad (56)$$

and putting the last three equations together yields

$$\chi(\omega) = \frac{\varrho \hbar |g_p|^2}{\epsilon_o} \left(\frac{i}{\Gamma - i\Delta_p + \frac{|\Omega_c|^2/4}{\Gamma_g - i(\Delta_p - \Delta_c)}} \right), \quad (57)$$

where $|g_p|^2 = |\Omega_p|^2/E_p^2$. In the limit $|\Omega_c| \rightarrow 0$ the susceptibility reduces to that of a two-level atom.

This is indeed a very interesting result. Before considering its implications, it is important to remember that the real part of the susceptibility is related through the real index of refraction to the group velocity of a wave propagating in the medium, while the imaginary part of the susceptibility is related to the absorption of said wave through the imaginary index of refraction. To a first approximation

$$n_r = 1 + \frac{\chi_r}{2}, \quad n_i = \frac{\chi_i}{2}, \quad (58)$$

where n_r and n_i are the real and imaginary parts of the index of refraction n .

Going back to Eq. (57), consider for instance, the case when $\Delta_p = \Delta_c = 0$:

$$\chi(\omega) = \frac{\varrho \hbar |g_p|^2}{\epsilon_o} \left(\frac{i\Gamma_g}{\Gamma_g \Gamma + |\Omega_c|^2/4} \right), \quad (59)$$

where it can be seen that the susceptibility of the medium becomes purely imaginary. This means that the index of refraction is $n_r = 1 + \frac{\chi_r}{2} = 1$, and the wave has a phase velocity of $v_p = \frac{c}{n_r} = c$. It can also be seen that as $|\Omega_c|$ becomes increasingly larger, $\chi(\omega) \rightarrow 0$, so the absorption vanishes. To find the lineshape and width near the spectral region of the vanishing absorption, consider that for an optically thick medium of length z and optical depth $\varrho\sigma z > 1$ (σ is the atomic absorption cross section), the intensity transmission amplitude is defined as [26, 59]

$$T(\omega) = \frac{I(z)}{I(z=0)} = e^{-kz\chi_i}. \quad (60)$$

By expanding χ_i in the vicinity of the two photon resonance $\Delta_p = \Delta_c = 0$ in a power series, and assuming $|\Omega_c| \gg \Gamma_g(\Gamma, \Delta_p), \Delta_p^2, \Gamma^2$, then

$$T(\omega) \simeq e^{-\frac{(\Delta_c - \Delta_p)^2}{\Delta\omega_{EIT}}}, \quad (61)$$

$$\Delta\omega_{EIT} = \frac{|\Omega_c|^2}{\Gamma_p \sqrt{\varrho\sigma z}}, \quad (62)$$

the vanishing absorption is a Gaussian, where $\Delta\omega_{EIT}$ is the width of the transparency. Clearly Ω_c has a broadening effect, and the transparency is narrower for media with larger optical depth. For a very intense coupling field, the absorption profile is then split by an amount proportional to Ω_c , consistent with the Autler-Townes splitting effect [60]. If $\Omega_c \ll \Gamma_p$ the window of the transparency is smaller than the natural linewidth of the transition. It should also be mentioned, from Eq. (59), that decoherence of the ground states quickly inhibits the transparency of the medium.

This is what is understood by “EIT”, the medium dressed by the strong coupling field becomes transparent to a probe beam for a narrow frequency range, and the depth and width of the transparency are dependent on the intensity of the coupling beam. A vanishing absorption can just as easily be obtained by tuning the frequency of the probe beam far away from resonance, but the difference is that because of the difference in the susceptibility of the dressed medium, the probe can experience strong nonlinear effects.

For the ideal case of no ground-states decoherence ($\Gamma_g = 0$), the only significant decoherence rate is the probe spontaneous decay rate ($\Gamma \rightarrow \Gamma_p/2$); finding the real and imaginary components of the susceptibility for $\Delta_c = 0$ yields:

$$\chi_r = \frac{\varrho\hbar|g_p|^2}{\epsilon_o} \left(\frac{4\Delta_p(|\Omega_c|^2 - 4\Delta_p^2)}{(|\Omega_c|^2 - 4\Delta_p^2)^2 + 4\Delta_p^2\Gamma_p^2} \right), \quad (63)$$

$$\chi_i = \frac{\varrho\hbar|g_p|^2}{\epsilon_o} \left(\frac{8\Delta_p^2\Gamma_p}{(|\Omega_c|^2 - 4\Delta_p^2)^2 + 4\Delta_p^2\Gamma_p^2} \right). \quad (64)$$

Figure 9 shows the real and imaginary parts of the complex susceptibility $\chi(\omega)$, plotted as a function of Δ_p/Γ_p , for $\Delta_c = 0$. The dip in the absorption and consequent transparency at the resonant frequency $\Delta_p = 0$ is obvious from the χ_i plot. Now consider the real part of the complex susceptibility $\chi(\omega)$. It can be seen from this plot that the dispersion χ_r is zero at resonance, and that it is linear and has a positive steep slope about the transparency frequency range. This differs significantly from the behavior of dispersion for a “undressed” medium consisting of two-level atoms (see Fig. 44, Appendix A).

The slope of the dispersion curve is given by $\frac{d\chi_r}{d\omega}$, and from Eq. (64), it can be

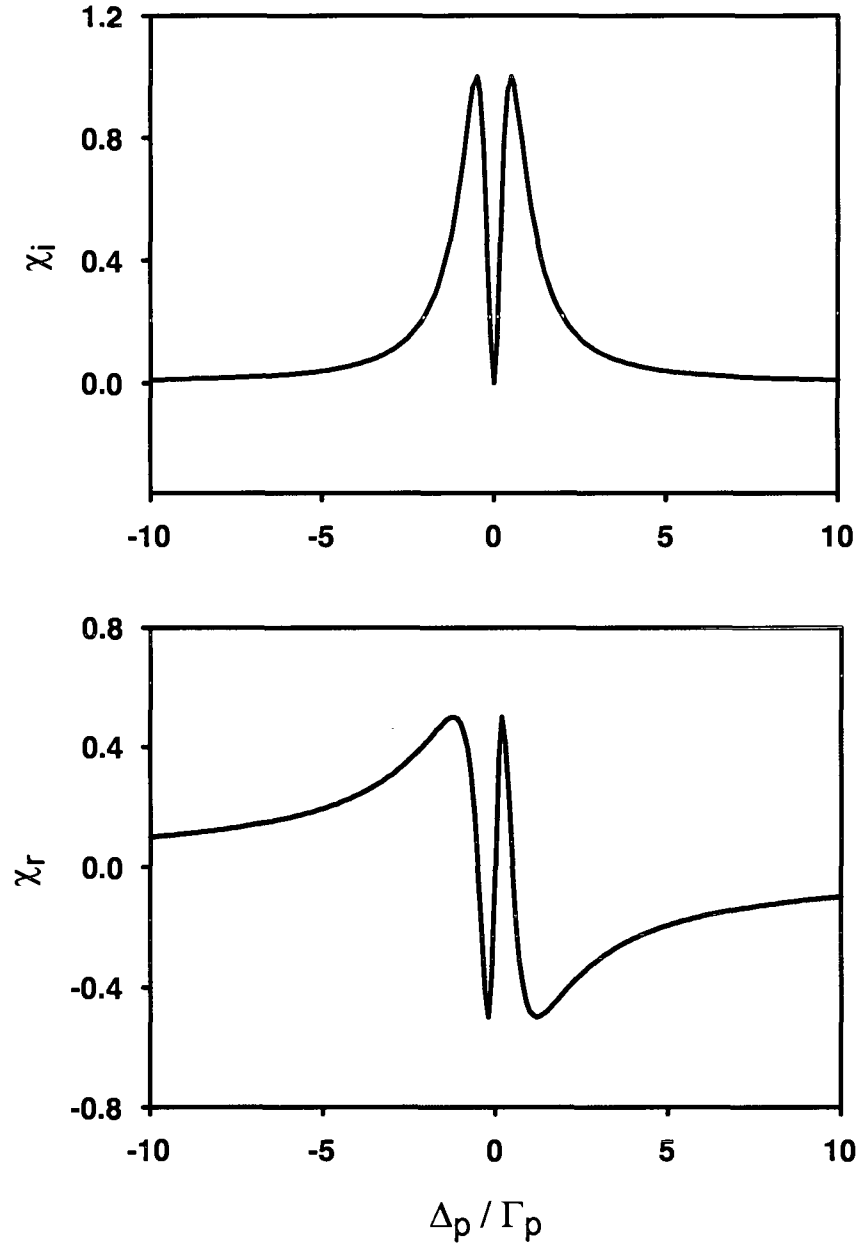


FIG. 9: Complex Susceptibility $\chi(\omega)$ in an EIT system. $\Delta_c = 0$. χ_i is the imaginary part of the susceptibility; it shows that at resonance the absorption goes to zero. χ_r is the real part of the susceptibility; it can be seen that there is normal steep dispersion about the resonance frequency.

found that the leading term is [17]

$$\frac{d\chi_r}{d\omega} = \frac{\rho\hbar|g_p|^2}{\epsilon_o} \left(\frac{4}{|\Omega_c|^2} \right). \quad (65)$$

Thus it can be seen that while at resonance there is no group velocity dispersion, away from resonance the medium can become highly dispersive, and it is directly dependent on the coupling field intensity given by Ω_c .

Recall that the group velocity of a wave is given by

$$v_g = \frac{d\omega}{dk} = \frac{c}{\left(\omega \frac{dn_r}{d\omega} + n_r \right)}, \quad (66)$$

where the first term in the denominator dominates. Therefore, at resonance ($\Delta_p = \Delta_c = 0$), for negligible ground-states decoherence, and when Ω_c is smaller than Γ_p , the group velocity of the wave is

$$v_g \approx \frac{c\epsilon_o|\Omega_c|^2}{2\rho\hbar\omega_p|g_p|^2}. \quad (67)$$

This is quite a remarkable result. It implies that even though there is no absorption of the wave, for high atomic densities and small Ω_c , the group velocity can become very small; it is the intensity of the coupling laser that controls the group velocity of the probe laser through the medium.

The first demonstrations of reduced pulse group velocity were done in 1995 by Kasapi et al. [18], in lead vapor, where velocities as slow as $c/165$ were observed. It was, however, the beautiful experiments in 1999 by Hau et al. [31], where a group velocity of 17 m/s was reported in a Bose-Einstein condensate of Na atoms, that opened the door for using ultra-slow light pulses, in ultracold media, for quantum information purposes.

In terms of pulse propagation, the implications of a reduced group velocity in a transparent medium are profound. First, the index of refraction is unity, so there is no reflection of the wave at the boundary of the medium; since there is no absorption there is no dissipation of energy, so the electric field strength remains constant. However, as the pulse enters the medium it becomes compressed in the direction of propagation (because the front of the wave that has entered the medium travels much slower than the rest of the incoming wave) by a factor of c/v_g [32]; this allows the possibility of probe pulses to be completely localized within the atomic medium. So, although the photon flux (power per area) is constant, the number of photons in

the medium is reduced by the same factor c/v_g . The extra electromagnetic energy must be temporarily stored in the atom-coupling field system [39]; as the wave leaves the atomic cloud the energy returns to the probe pulse adiabatically so that there is no net momentum transfer to the atomic medium.

An explanation of the adiabatic transfer of energy between the probe pulse and the atom-coupling field system was proposed by Fleischhauer and Lukin in 2000 [39] in terms of a quasi-particle bosonic excitation called a “dark-state polariton:”

$$\hat{\Psi}(z, t) = \cos \theta(t) \bar{E}_p(z, t) - \sin \theta(t) \sqrt{\varrho} \rho_{21}(z, t) e^{i\Delta_k z}, \quad (68)$$

$$\tan^2 \theta = \frac{\varrho \sigma c \Gamma_p}{\Omega_c^2}, \quad \varrho = \frac{N}{V}. \quad (69)$$

Here, ϱ is the atomic density, ρ_{21} is the matrix element of the undressed atom, $\Delta_k = k_c^{\parallel} - k_p$, k_p is the probe field wave number, and k_c^{\parallel} is the projection of the control field wave vector onto the z -axis. The equation for the dark-state polariton has two components, a electromagnetic or photonic one, in terms of the normalized probe field \bar{E}_p , and an atomic one, in terms of the atomic density, the coherence of the ground states, and the projection of the control field wave vector along the direction of propagation of the probe. These two components are mixed by an angle θ that depends on the atomic density and, most importantly, on the control field intensity given by Ω_c . Thus, by adiabatically varying Ω_c the quasi-particle excitation may become purely atomic, or purely electromagnetic. At this point it is necessary to point out that now the term “group velocity” refers to the velocity of the excitation whether it is in an electromagnetic, atomic, or mixed state. The fact that the atomic density ϱ is part of the atomic component of the polariton implies that this is a collective excitation. It should also be pointed out that the atomic component is in terms of the ground state coherence as specified by ρ_{21} . In the initial experiments [34] these ground states were Zeeman or hyperfine states, thus the atomic excitation was called a “spin” excitation or “spin wave,” and it continues to be called in this manner in the literature.

Before the probe pulse interacts with the medium, the control pulse “prepares” the medium by optically pumping all the atoms to the bare state $|1\rangle$. From Eq. (38) it can be seen that in the limit $\Omega_p = 0$ the dark state $|NC\rangle$ corresponds to $|1\rangle$. According to Fleischhauer et al. [26], as the probe pulse enters the medium, the dark state rotates through an angle θ to a superposition of $|1\rangle$ and $|2\rangle$. The energy necessary for this rotation, for establishing the coherence, is taken from the

probe field into the dressed atoms. The speed of rotation depends on the strength of the coupling field, if $\Omega_c \rightarrow 0$ the rotation stops, leaving the excitation stationary in the form of a purely coherent atomic excitation (which can exist in the medium for as long as the coherence is maintained). The reverse situation occurs when the polariton reaches the exiting boundary of the atomic medium, then the dark state rotates adiabatically back into $|1\rangle$, taking the energy necessary to do so from the atomic-coupling field system and transferring it to an electromagnetic excitation that can then leave the sample. In this sense, light can be “stored” and “retrieved” in an atomic vapor.

II.4 MULTIPLE SCATTERING IN RANDOM MEDIA

Atoms as scatterers of electromagnetic waves form well-controlled and characterized systems in which to study light propagation, since an atomic cloud is a monodisperse ensemble of scatterers. Well-defined atomic transition lines allow strongly resonant light scattering. At the same time, cold atomic vapors are suitable because the Doppler broadening is reduced, and the sample is quasi-static. Transport of radiation in atomic vapors is normally thought of as a diffusive incoherent process where radiation waves are sequentially scattered by the atoms of a macroscopic system, particularly given the large dephasing effects associated with collisions or atomic motion. However, there are regimes for which such a description is not appropriate. Multiple scattering of light frequently appears as radiation trapping, which is a slowing of the escape of radiation as the vapor density is increased.

In particle diffusion, a particle travels undisturbed through free space until it suffers a collision with some other particle, whereby it changes its direction and speed, which leads to a statistical wandering of the particle. The main parameter describing its behavior is the particle’s mean free path between collisions [61]. In the simplest case, the process can be described as a particle performing a three dimensional random walk.

Consider a particle undergoing a Brownian motion in three dimensions through a fluid medium, and let $P(r_o, r, t)$ be the probability that the particle is found at the position r at a time t , provided the particle was at the position r_o at $t = 0$. Such a particle will have a motion given by the diffusion equation

$$\frac{\partial P(r_o, r, t)}{\partial t} = D \nabla^2 P(r_o, r, t), \quad (70)$$

in terms of the diffusion coefficient D [62, 63, 64]

$$D = \frac{lv}{3}, \quad (71)$$

where v is the velocity of the particle, and l is the mean free path, i.e. the average distance that the Brownian particle travels undisturbed from one scattering event to the next one.

The solution to this equation for an infinite homogeneous and isotropic medium is the spatial Gaussian

$$P(r_o, r, t) = \frac{1}{(4\pi Dt)^{3/2}} \left(e^{-\frac{(r-r_o)^2}{4Dt}} \right). \quad (72)$$

The consequence of this probability distribution is obvious: as time goes on, the particles will spread out and the local density will be reduced. This irreversible process is a result of the random nature of the collisions between the Brownian particles and the fluid medium particles.

There are some important differences between particle diffusion and radiation diffusion [61]. The first important difference is that in particle diffusion, the time between two “scattering” (collision) processes is rather long, while the scattering process itself is almost instantaneous in a dilute gas. In radiation trapping the “scattering” (absorption-reemission) process is rather long, while the time between scatterings is very short (the time of flight of the photon).

The second difference lies in the definition of mean free path. In radiation diffusion, the probability of scattering or absorption is given by the linewidth or lineshape of the atomic resonance. This implies that the mean free path depends strongly on the frequency of the near-resonant light. In order to still be able to use a diffusion model to describe radiation scattering in random media, a redefinition of parameters is needed. For radiation scattering, the diffusion constant D is now defined as

$$D = \frac{l^* v_E}{3}, \quad (73)$$

where l^* is the energy transport mean free path, and v_E is the energy transport velocity. The transport mean free path describes the distance necessary, on the average, for the initial direction of propagation of the light to be randomized, or the average distance that the energy propagates along the initial direction [65]. The energy transport velocity v_E accounts for the propagation of energy by the scattered wave [66].

The diffusion model is valid when $l^* \gg \lambda$, where λ is the wavelength of the radiation. The transport mean free path can also be defined in terms of the atomic sample's density ϱ and the frequency-dependent scattering cross section σ as

$$l^* = \frac{1}{\varrho\sigma}. \quad (74)$$

For a weak field, the total light scattering cross section depends on the incident light's detuning from resonance Δ_L , the transition energy levels J (ground state) and J' (excited state), and the transition probability width Γ_L , in the following way:

$$\sigma = \frac{2J' + 1}{2J + 1} \left(\frac{\lambda^2}{2\pi} \right) \frac{1}{1 + \left(\frac{2\Delta_L}{\Gamma_L} \right)^2}. \quad (75)$$

Very few detailed experiments have been performed to study the diffusion of light in cold atomic clouds. Interestingly, Labeyrie et al., confirms that the transport time per scattering event is equal to the natural lifetime, independent of detuning from resonance [67, 68]. In this analysis, multiple scattering is considered to be composed of individual scattering events and propagation to the next scatterer in an effective medium with an index of refraction $n = n_r + in_i$, where n_r is the real component of n and is related to the group velocity v_g of the propagating energy, and n_i , the imaginary part, measures the attenuation through the sample. The transport time τ_{tr} is then the sum of the time delay due to the scattering process τ_W , and the propagation time in the effective medium with the group velocity v_g :

$$\tau_{tr} = \tau_W + \frac{l^*}{v_g} = \tau_{nat} = \frac{1}{\Gamma_L}. \quad (76)$$

This is a very interesting result, since for near-resonant light τ_W , l^* , and v_g depend on the frequency detuning from resonance.

Another important factor that is neglected by a diffusive theory is the effect of wave interference. There are situations, such as in coherent backscattering (CBS) where constructive interference of multiply scattered waves occur [69].

Of most particular relevance to this dissertation, is the prediction by Datsyuk et al. [43] that under conditions of EIT, light multiply scattered in an elastic way would emerge from the atomic sample with the time delay associated with EIT reduction of the group velocity. They predict that the polariton will not disappear but will diffuse coherently through the sample, and that the scattered or diffuse polariton may be stored and regenerated just as in the forward direction.

CHAPTER III

GENERAL EXPERIMENTAL ARRANGEMENT

In the first part of this chapter the details of the experimental setup will be discussed. These include the diode laser systems, the Rb vacuum chamber system, and the optical setup for the MOT. The detection setup will be discussed in the data acquisition chapter. The second part of this chapter describes the procedures used to characterize the ultracold ^{87}Rb atomic gas.

III.1 DIODE LASER SYSTEMS

The formation, characteristics, and behavior of the ultracold Rb gas are determined by the lasers that at any given time interact with it. Lasers cool and trap the atoms that become the sample; the lasers' frequency, intensity, and beam shape determine the characteristics of the ultracold sample. An external laser light interacting with the cooled Rb gas can alter the optical properties of the aforementioned sample, as can be observed by probing with yet another laser light source. It is therefore important to have good control of the laser systems used in the experiment; the different components needed are discussed in this section.

III.1.1 EXTERNAL CAVITY DIODE LASERS

The MOT trapping and probing lasers, the repumper laser, and the EIT control and probe lasers come from external-cavity diode laser (ECDL) systems. An external cavity diode laser consists of a semiconductor diode laser, and optical elements to provide optical feedback into the diode. Semiconductor diode lasers, while being cost-effective and having good amplitude stability, have linewidths on the order of tens of MHz, and continuous tuning is limited to intervals given by the diode cavity modes. Furthermore, the lasing frequency is dependent on the temperature and injection current. Optical and electronic feedback can reduce the linewidth to less than 1 MHz (much less than the linewidth of the atomic transitions of interest), and allow frequency stabilization, single-mode oscillation, and larger continuous tuning over the frequency intervals [70].

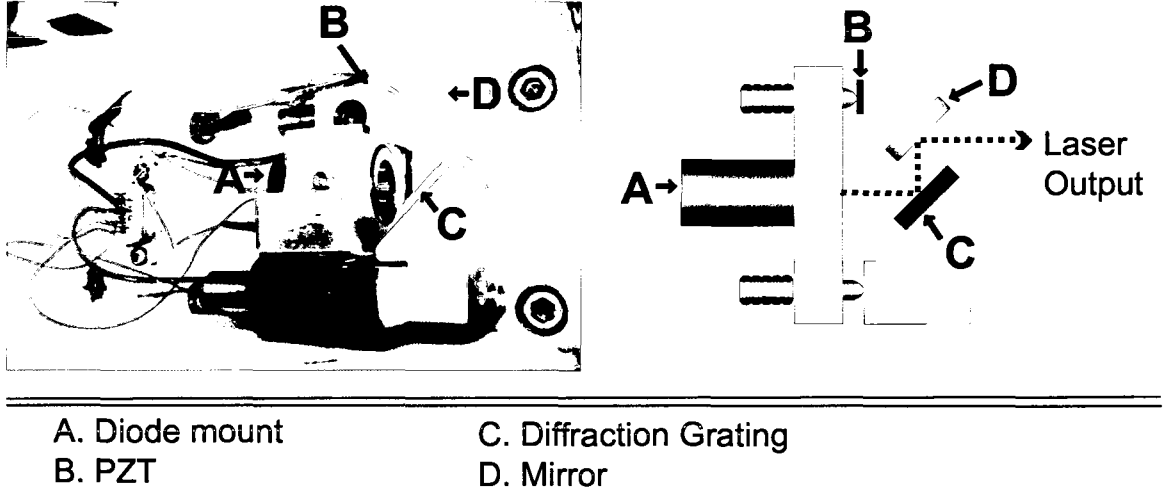


FIG. 10: External-cavity diode laser (ECDL). On the left is a picture of the ECDL box. On the right is the corresponding top view schematic of the ECDL in Littrow configuration.

A common optical feedback method is by the use of a diffraction grating, which can be used in either the Littman-Metcalf configuration [71, 72], or in Littrow configuration [73, 74, 75, 76].

In this experiment, semiconductor diode lasers (Sharp GH0781JA2C, 120 mW CW at 784 nm) were used in the Littrow configuration, as can be seen in Fig. 10. In Littrow configuration, the grating is aligned so that the light diffracted into the first order is sent back to the diode; in this case the external laser cavity is formed by the back facet of the diode's internal cavity and the grating. The output of the laser is given by the zeroth order reflection from the grating (Optometrics LLC., 3-4182, 1800 lines/mm). Following the design by Hawthorn, Weber and Scholten in Ref. [76], a mirror (Thorlabs Inc., BB05-E03, Broadband Dielectric, 750-1100 nm) has been mounted on the arm of the laser cavity, so that it is fixed with respect to the grating; this design produces a compact ECDL with a cavity length of about 12 mm, with a fixed direction output beam. The diode laser is mounted in a collimation tube (Thorlabs Inc., LT230P-B) with an aspheric lens (Thorlabs Inc., A230TM-B $f = 4.55$ mm, 0.54 NA, 600-1050 nm). The collimation tube, grating and mirror are mounted on a modified mirror mount (Thorlabs Inc., KS1D, differential drive). For a given temperature, the laser frequency can be coarsely tuned by adjusting

the injection current using a laboratory-built current controller. Fine tuning of the laser frequency is achieved by placing a low voltage piezoelectric multi-layer actuator (Thorlabs Inc., AE0203D04, Max Displacement $4.6 \mu\text{m}$) between the grating mount and the adjustment screw, thus allowing fine control of the cavity length.

The diode laser is very sensitive to temperature changes for two reasons: the wavelength dependence of the gain curve and the external cavity length are temperature dependent [70]. Temperature control and stability are achieved by mounting the ECDL on a thin aluminum platform attached to a thermoelectric cooler (Marlow Industries Inc., DT12-6-01L), which is itself mounted on a large aluminum base. To ensure good thermal flow all surfaces have been coated with a thermal compound (Arctic Silver 5). The thermoelectric cooler (TEC) is connected to a laboratory-built temperature controller with a servo loop. The feedback to the temperature controller is given by a thermistor (Thorlabs Inc., TH10K, $10 \text{ k}\Omega$), which is placed deep within a hole in the thin aluminum platform, to monitor the temperature close to the TEC and the diode laser mount. The ECDL has been enclosed in an aluminum case (with appropriate holes for reaching the grating's adjustment screws and the beam output), and a Plexiglass cover.

Enclosing the ECDL not only aids in stabilizing the temperature, but also reduces air currents and vibrational disturbances, which also contribute to the destabilization of the laser. To further reduce vibration, a layer of noise dampening material (Nexus DampTek Noise Absorption Material) has been attached to the walls of the aluminum case. However, the most critical element towards vibration control of the whole experimental setup (the diode laser systems, the MOT chamber, the alignment optical elements and the detection system) is given by the optical table (Ealing Vibration Isolation System, Model 245316).

III.1.2 LASER FREQUENCY STABILIZATION AND DOPPLER-FREE SATURATED ABSORPTION SPECTROSCOPY

For this experiment, it is desirable to stabilize the frequency of the lasers at or near an atomic transition resonance for long intervals of time. This is achieved using electronic feedback to lock the frequency to one of the peaks of a ^{87}Rb saturated absorption spectrum (SAS).

In order to understand saturated absorption spectroscopy, it is necessary first to understand the role that the Doppler effect plays on linear spectroscopy. The

particles in a gas at thermal equilibrium moving in a random way can be described by a thermal (Maxwell-Boltzmann) velocity distribution. Consider a laser beam propagating through the thermal gas and an atom at rest relative to the laser which absorbs resonance radiation with a frequency ω_o . When this atom moves towards the laser it will see blue-shifted radiation, and when the atom moves away from the laser it will see red-shifted radiation. This means that the atom will absorb radiation from a range of frequencies centered at ω_o . In the rest frame of the laser, the frequency ω of radiation absorbed is given by $\omega = \omega_o(1 + v/c)$, where v is the velocity of the atom. If v is negative (the atom moves towards the laser), then ω is blue-shifted, and if v is positive (the atom moves away from the laser), then ω is red-shifted [77].

From Maxwell-Boltzmann statistics, neglecting the spectral distribution of the atomic response, it can be shown that the intensity profile as a function of absorbed frequencies ω is given by

$$I(\omega) = I_o e^{-[\frac{c(\omega - \omega_o)}{\omega_o v_p}]^2}. \quad (77)$$

In this equation, $v_p = \sqrt{2k_B T/M}$ is the most probable velocity for a particle of mass M at temperature T , and k_B is Boltzmann's constant [78]. This is a Gaussian intensity profile, for which the full-width at half-maximum (FWHM) is given by

$$\Delta\omega_D = \left(\frac{\omega_o}{c}\right) \sqrt{\frac{8 \ln 2 k_B T}{M}}, \quad (78)$$

also known as the Doppler linewidth. For ^{87}Rb atoms at room temperature (300 K), this means a spectral broadening of 513 MHz. Since the natural linewidth of ^{87}Rb is about 6 MHz, the close spectral lines of the hyperfine structure cannot be resolved using linear Doppler-limited spectroscopy.

In the 1970s, high resolution spectroscopy was possible once powerful, narrow-band, tunable lasers became available. Schawlow, Hänsch, and Bordé developed independently several new methods using nonlinear optics which resulted in Doppler-free spectroscopy [79]. Saturation spectroscopy is a nonlinear method based on the velocity-selective saturation of atomic transitions [78, 80, 81]. Consider two overlapping laser beams with frequency ω equal to an atomic resonance transition, of unequal intensities, propagating in opposite directions through a sample of atoms. In this configuration both beams interact at the same time with the atoms that do not see any Doppler shift, that is, those atoms that travel with a velocity v_z in a direction perpendicular to the laser beams. By itself, the more intense “pump” beam will saturate the transition, reducing the number of atoms with velocity v_z in the ground

state and producing a linear Doppler-broadened spectrum. When the less intense “probe” beam passes through the atom sample, it experiences reduced absorption and a dip appears at the resonant frequency ω on top of the Doppler-broadened absorption spectrum.

Figure 11 shows an example of the saturated-absorption spectroscopy setup used in the present experiment. In this setup, a wedged beamsplitter (Thorlabs Inc., BSP10-B1, BK7 AR coated, 0.5° wedge) picks off a small amount of the output of an ECDL. It is then split using a regular thick glass beamsplitter into three beams: an intense “pump” beam, and two less intense parallel beams, one of which will be used as a probe beam, and the other will be a reference beam. The pump beam is aligned using regular visible Al mirrors to overlap the counterpropagating probe beam. To prevent this counterpropagating beam to couple into the ECDL, an optical isolator (OFR, I0-3-780-LP) is used. This optical isolator produces a magnetic field; there are two layers of μ metal (National Electronic Alloys, Inc., HY Mu 80) around the optical isolator and Rb glass cell to reduce the spectral broadening due to Zeeman splitting in the presence of a magnetic field. A neutral density filter is used to attenuate the intensity of the pump beam and the associated saturation broadening of the SAS. After going through a Rb glass cell at room temperature, the signals from the probe and reference beams are sent by thin regular glass beamsplitters into a laboratory-built photodiode detector (PDD) box with an I/V converter and two separate photodiode detectors (Thorlabs Inc., FGA10), wired so that their balanced signals will subtract. The reference beam by itself produces a linear Doppler-broadened spectrum; by subtracting the signal from the probe beam, a Doppler-free hyperfine spectrum remains.

Figure 12 shows the Doppler-free saturated absorption spectrum of ^{87}Rb for transitions from the ground state $F = 2$ to excited states F' . As can be seen, besides the hyperfine structure, other peaks or dips appear in the spectrum. These are called “crossover” signals. A crossover signal appears whenever two transitions with a common lower or upper level are close enough that their Doppler-broadened spectra overlap. If there are two transitions ω_1 and ω_2 with a common level, at a frequency $\omega_{cross} = (\omega_1 + \omega_2)/2$, the pump and probe beams can be simultaneously in (Doppler-shifted) resonance with two complementary groups of atoms, and therefore have nonlinear absorption. Because two groups of atoms are saturated at the crossover frequency ω_{cross} , the absorption signals can be larger than the individual signals at the ω_1 or ω_2 frequencies.

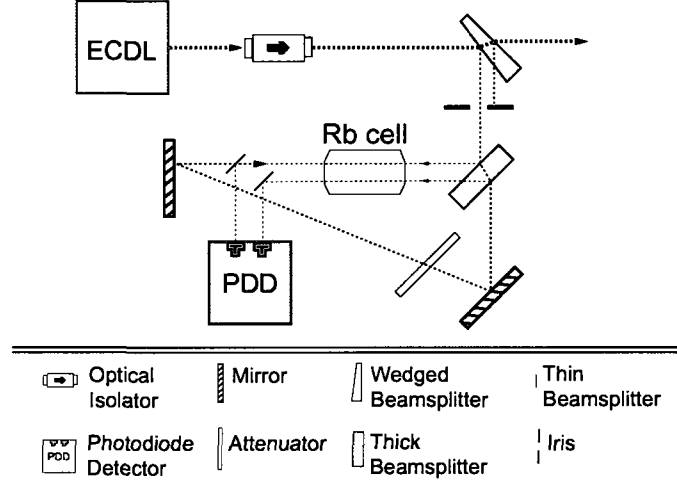


FIG. 11: Saturated-absorption spectroscopy setup. Only a small percentage of the external-cavity diode laser (ECDL) is used for saturated-absorption spectroscopy; the rest is used for the experiment.

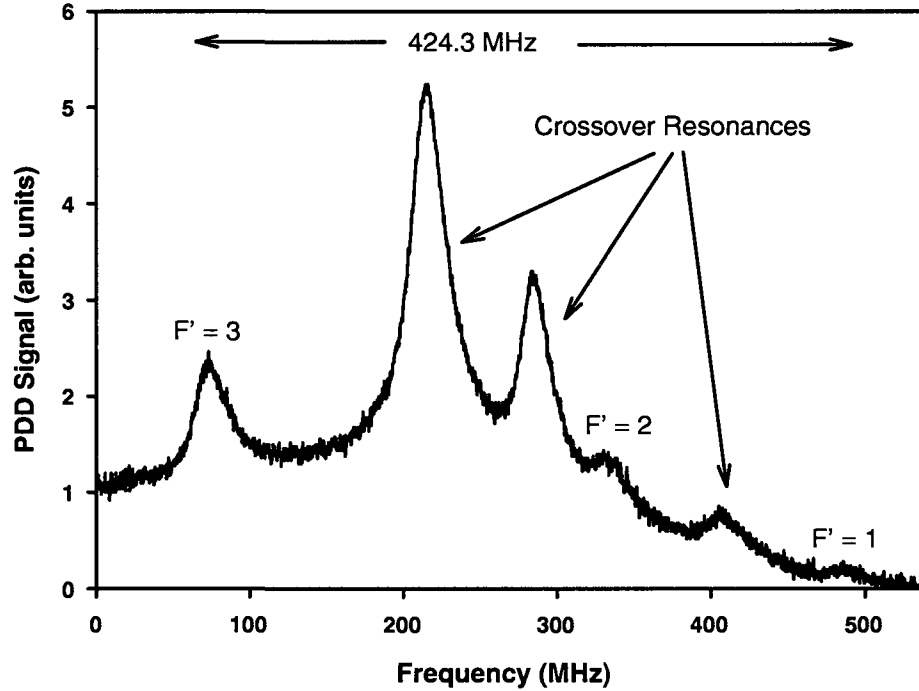


FIG. 12: Saturated-absorption spectrum of ^{87}Rb for transitions from the ground state $F = 2$ to excited states F' . In the frequency axis, the zero crossing point is chosen arbitrarily.

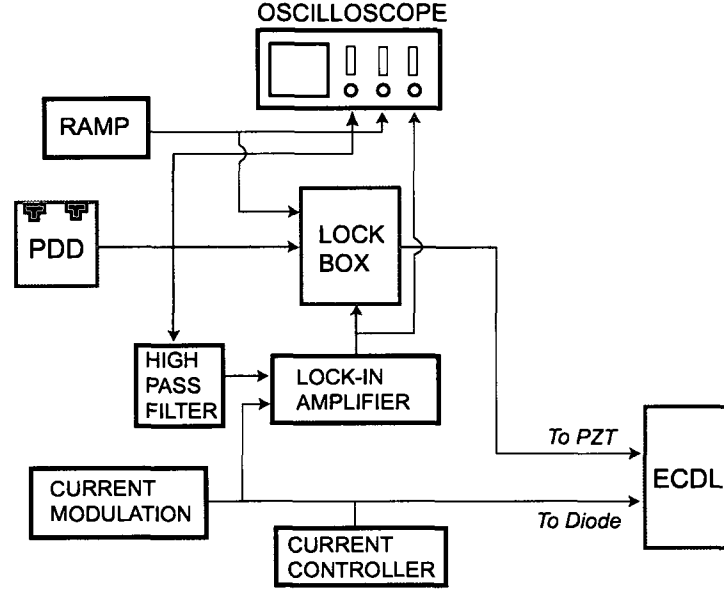


FIG. 13: Flow diagram of the electronic components for the frequency locking setup. PDD stands for photodiode detector, ECDL stands for external-cavity diode laser.

To lock the laser frequency, the SAS is sent to a laboratory-built lock-box, and a lock-in amplifier (Scitec, Model 410), which is a phase-sensitive detector. A laboratory-built high-pass filter is used to block unwanted low frequency noise from the input SAS signal. A sinusoidal wave from a function generator (Exact, Model 119) with a frequency of 10 kHz modulates the laser frequency and provides a reference signal for the lock-in amplifier. The output of the lock-in amplifier is a dispersive error signal, which is similar to the first derivative of the absorption signal. The laser is locked by adjusting the scan ramp gain and offset in the lock-box to a peak of the SAS, which corresponds to the zero-crossing of the dispersive error signal. The lock-box is simply a servo loop circuit which monitors the error signal and continuously adjusts the PZT in the ECDL accordingly [73, 78, 82, 83]. A flow diagram of the locking electronic setup is shown in Fig. 13. The advantage of using a frequency locking technique with a high-frequency modulation signal is that technical noise (which affects the laser stability) decreases with increasing frequency. The disadvantage in this case is that, as the frequency is modulated via the injection current controller, the laser power is also modulated.

III.1.3 LASER POWER AMPLIFICATION

The number of atoms trapped in a MOT is dependent, among other parameters, on the intensity of the trapping laser. When the trapping laser is detuned to the red, the number of atoms with higher velocities that can be Doppler cooled increases, allowing a larger fraction of atoms to be trapped. However, the intensity of the laser has to be high enough to saturate the trapping transition, even when the laser is red-detuned.

In order to obtain a larger power for the MOT trapping laser, a two-diode laser system was used in what is commonly known as a master-slave configuration. In such a system, radiation from a spectrally-narrow, low power master laser is coupled or injected into a spectrally-broad, higher power slave laser [84, 85, 86]. For more detail into injection locking and pulling in oscillators, Ref. [87] is recommended. In the ideal case, as a consequence of optical injection, the broad range of frequencies of a free-running slave diode laser can be forced to collapse to the single-mode frequency of the external master diode laser. In this way, the slave laser frequency will stay locked to the frequency of the master diode laser, while the master laser frequency can be scanned, modulated, or locked to an external reference.

To successfully injection-lock a laser, the following conditions need to be satisfied: the polarization of the master has to match the polarization of the slave output, the spot size of the master must match or be smaller than the slave's, the wavelength of the master must be within the wavelength range of the slave, the alignment of the master must be optimized for injection, and the master laser power must be large enough to be above the coupling or locking threshold.

Figure 14 is a schematic of the master-slave system used in the present experiment. The master laser is an ECDL as described above, which has been frequency locked to a SAS. In order to match (approximately) the spot size of the slave diode laser, a telescope with $M = 3.5$ magnification has been added to shrink the size of the beam (Newport Corp., KPX091 $f = 88.3$ mm, Thorlabs Inc., LD2297 $f = -25$ mm). A half waveplate (Nova Phase, WP12.7-780HM-M) ensures that there is polarization matching between both lasers. A wedged beamsplitter with a back AR coated surface (Thorlabs Inc., BSP10-B1, BK7 AR coated, 0.5° wedge) picks off 0.95 mW of the master laser light, which is enough power to induce injection locking, while allowing most of the slave light to go through. The slave laser is a temperature-stabilized diode laser similar to the master laser (Sharp GH0781JA2C, 120 mW CW at 784

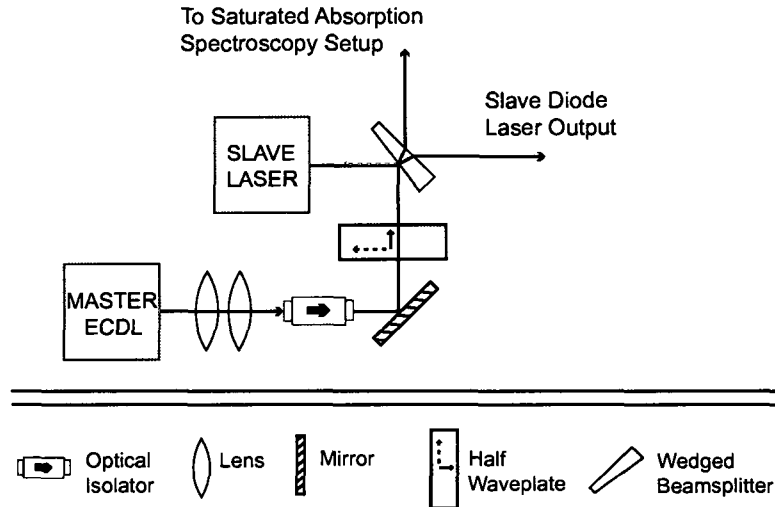


FIG. 14: Schematic of two diode lasers in a master-slave configuration. The master slave is an external cavity diode laser whose beam size and polarization have been modified to optimize optical injection into the slave; it is frequency-locked to an external saturation absorption signal. The slave laser output goes through a wedged beamsplitter with a back AR coated surface to minimize interference fringes and optical losses.

nm), but without the diffraction grating and output mirror, which ensures a higher output power.

III.1.4 LASER FREQUENCY SHIFTING AND ACOUSTO-OPTIC MODULATORS

The MOT trapping beam, the MOT probe and the EIT control beam come from a two-diode laser system in a master-slave configuration, where the master laser has been locked to the $F = 2 \rightarrow F' = (1,3)$ crossover resonance. The MOT repumper and the EIT probe beams come from a different ECDL, locked to the $F = 1 \rightarrow F' = (1,2)$ crossover resonance. These frequencies are not suitable either for creating a MOT, or for the EIT experiment. To produce beams with the desired frequencies, acousto-optic modulator (AOM) systems have been used.

In an AOM, an acoustic wave generated by a radio frequency (RF) source travels through a crystal. The acoustic wave induces a traveling density wave inside the crystal, so that the index of refraction of the crystal is modulated at the frequency Φ of the RF signal. To a first approximation, the crystal behaves as a thick diffraction

grating, and an electromagnetic wave with a wavelength λ traveling through the crystal would experience diffraction according to the equation

$$\sin \theta = \frac{m\lambda}{2(v_s/\Phi)}, \quad (79)$$

where θ is the angle of the diffracted beam with respect to the normal of the crystal, $m = 0, \pm 1, \pm 2, \dots$ is the diffraction order, and v_s is the speed of sound in the crystal. This equation is similar to that for Bragg diffraction, $\sin \theta = \frac{m\lambda}{2d}$. Thus, by using an AOM, a laser beam may be deflected by a controlled amount by varying Φ , or by switching the RF source on and off.

Since the acoustic waves are moving with respect to the laser beam, the diffracted beam experiences a Doppler frequency shift equal to $\pm m\Phi$; thus it is possible to scan the laser frequency in a small range about a center frequency $\pm m\Phi$ by scanning the RF frequency [88, 89].

Figure 15 shows the laser and AOM systems used in this experiment. For all lasers, as described previously, an optical isolator is used to prevent retroreflections from destabilizing the laser, and a small percentage of the main (master) beam is picked off using a wedged beamsplitter to lock the frequency of the laser.

In Figure 15(a) a percentage the master laser (depicted here as ECDL 1), which is locked to the $F = 2 \rightarrow F' = (1,3)$ crossover resonance, is injected into the slave. Since the slave laser's beam size is greater than the optical isolator aperture, two lenses (Newport Corp., $f = 62.9$ mm; Thorlabs Inc., LD2297-B $f = -25$ mm) have been used to reduce the beam size and thus the loss of power derived from this laser. The polarization of the main beam is adjusted using a half waveplate (Thorlabs Inc., WPMH05M-780). The laser is then focused using a lens (Thorlabs Inc., LA1509-B $f = 100$ mm) into a 200 MHz AOM (Brimrose Corporation of America, TEM-200-50-.780). The laser is diffracted into the first order with an efficiency of about 54%. The specific frequency is set using a voltage-controlled oscillator (Mini-Circuits, ZOS-300) to the ^{87}Rb MOT trap frequency. The output beam is collimated using a lens (Thorlabs Inc., LA1509-B $f = 100$ mm) and is then sent into a polarization preserving fiber; for a proper launch into the fiber the size of the beam is readjusted by using another two lenses (Thorlabs Inc., LA1131-B $f = 50$ mm, LD2297-B $f = -25$ mm).

The AOM may be switched off (Mini-Circuits, ZYSWA-2-50DR), in which case the un-diffracted beam simply goes through the AOM crystal; this beam is similarly focused into another 200 MHz AOM (Brimrose Corporation of America, TEM-200-50-.780), collimated and sent to a polarization preserving fiber. By taking the beam

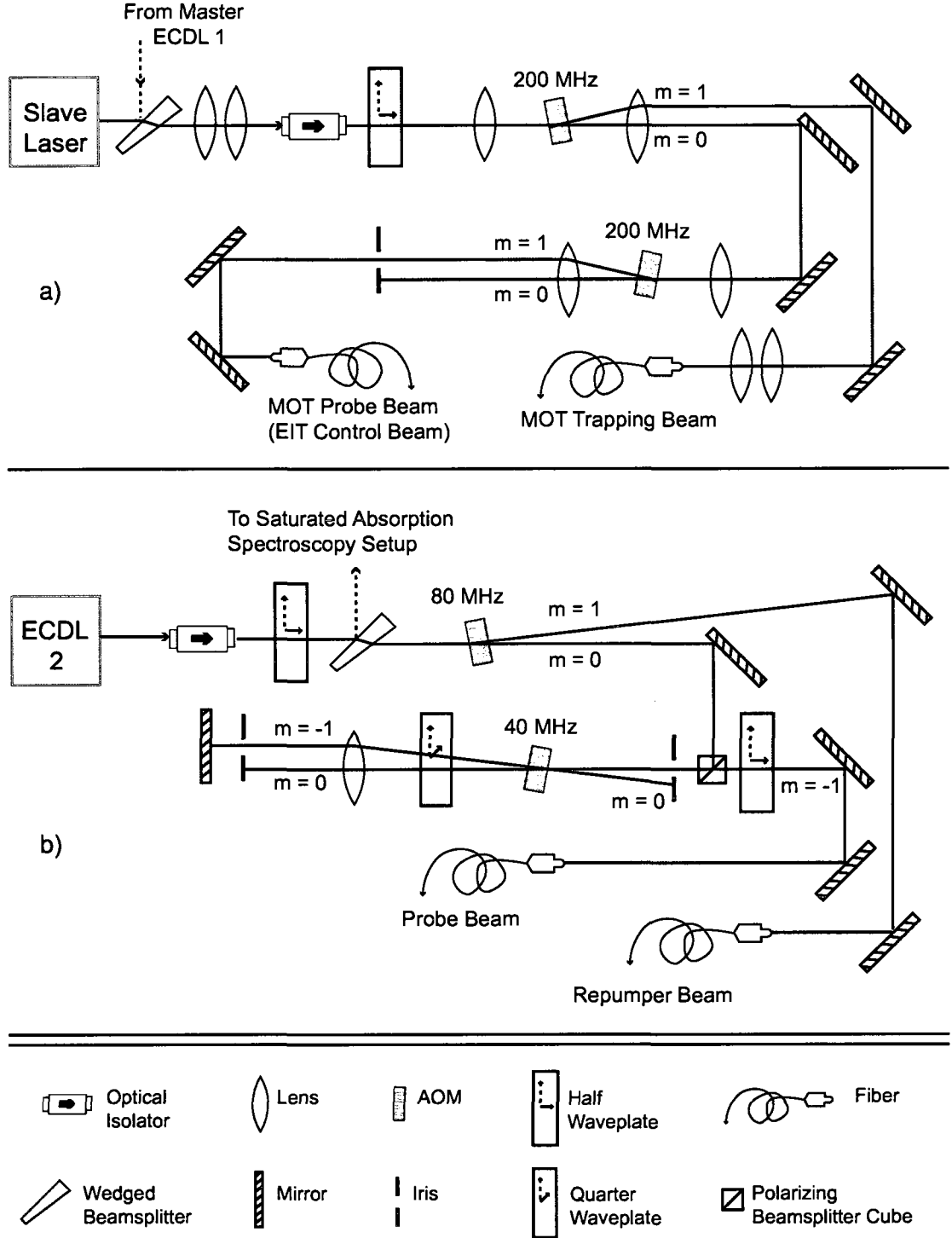


FIG. 15: Laser beam and AOM optical systems. (a) MOT trapping beam and MOT probe are shown in this schematic; when the angle of the second AOM is reversed, the beam at $m = -1$ is the EIT control beam. (b) The EIT probe beam in double-pass configuration and the repumper beam are shown.

diffracted at $m = +1$, the frequency may be scanned about the MOT trap frequency, hence this beam is an ideal MOT probe. On the other hand, if the beam is diffracted to the $m = -1$ order, the frequency of this beam may be set to the $F = 2 \rightarrow F' = 1$ resonance, and may serve as an EIT control laser.

In Figure 15(b) an external-cavity diode laser (depicted here as ECDL 2) is locked to the $F = 1 \rightarrow F' = (1,2)$ crossover resonance. Since the power derived from this laser is much greater than needed, no special care has been taken to reduce the beam size before the optical isolator. A half waveplate (Edmund Optics, NT38-396) is used to ensure that the laser has vertical linear polarization. The main beam is sent to an 80 MHz AOM (Neos Technologies Inc., 23080-1), and is diffracted into the $m = +1$ order with an efficiency of about 64%; a voltage-controlled oscillator (Mini-Circuits, ZOS-100) fine-tunes the frequency to the $F = 1 \rightarrow F' = 2$ resonance. This beam is sent to a single-mode fiber and is used as a MOT repumper laser.

When the AOM is switched off, the full un-diffracted beam is sent to an AOM in a double-pass configuration. A detailed description of the double-pass configuration can be found in Ref. [88]. The laser is reflected by a polarizing beamsplitter cube (Melles-Griot, 03 PBS 053) and is sent to a 40 MHz AOM (Datalight Inc., DLM-5VS), a quarter waveplate (Thorlabs Inc., WPMQ05M-780), and a lens (Newport Corp., KPX109 $f = 250$ mm). The negative first-order diffracted beam is retroreflected by a mirror (Thorlabs Inc., BB1-E03, fused silica substrate). As can be seen from Eq. (79), the diffraction angle depends on the specific radio frequency Φ ; using a lens-mirror combination ensures that the beam is retroreflected regardless of Φ , thus eliminating the need for beam steering and re-alignment when Φ is scanned. As the beam goes through the quarter waveplate for a second time, the light acquires a linear polarization orthogonal to the original polarization. As the laser goes for a second time through the AOM, the frequency is shifted again by the RF signal, and the resulting negative first-order diffracted beam overlaps the incident beam. This double-shifted beam goes through the polarizing beamsplitter into a half waveplate (Thorlabs Inc., WPMH05M-780) which rotates the laser's polarization to its original state, and is then coupled to a polarization preserving fiber. The center frequency of this laser is set to the $F = 1 \rightarrow F' = 1$ resonance and may be scanned using a voltage-controlled oscillator (Mini-Circuits, ZOS-50+); the overall efficiency of the double-pass configuration is about 25%. This beam served as the EIT probe.

III.2 THE VACUUM CHAMBER SYSTEM

In order to cool and trap a monatomic sample of ^{87}Rb atoms, a vacuum chamber system is used. In this context, vacuum refers to a space in which air and other gases are almost completely absent, and any air or gas pressure in the environment is much lower than atmospheric pressure [90]. By reducing the density of background gases below the vapor pressure of Rb, the loss of trapped Rb atoms due to collisions with background gases is minimized. The design, assembly and pumping of the vacuum chamber followed the guidelines of Ref. [91].

A combination of pumping methods has been used: first, a turbomolecular pump decreased the gas pressure from atmospheric pressure to below 10^{-4} Torr, then a further decrease of pressure was achieved by “baking” the system while using an ion pump. Outgassing is the process of evaporation and sublimation into a vacuum. As the chamber system is built and open to air, gases in the atmosphere and surrounding environment may attach to the walls, or are trapped in the welding process. As these gases evolve from the surfaces into the vacuum, they produce the same effect as a leak, in that they can limit the achievable vacuum. Outgassing depends on the adsorbed gases, the temperature of the surface, and the time of exposure to the vacuum. Raising the temperature of the system (baking) and thus raising the vapor pressure of such gases, can speed the outgassing process so that most of these particles can be pumped out. In this case, several different heaters were used to raise the temperature of the chamber, ion pump and valve to an average of $200\text{ }^{\circ}\text{C}$. In this way, a pressure below 10^{-8} Torr was achieved. Pressures of 10^{-9} Torr to 10^{-12} Torr are known as ultra high vacuum.

The chamber itself is a custom-made stainless steel cylindrical chamber (Huntington Mechanical Laboratories, Inc.) with a diameter of 15.24 cm, and a height of 5.08 cm. It has ten 2.75" outside diameter CF flange ports, as displayed in Fig. 16. Eight of the windows, including six for the MOT beams and two for detection are regular 7056 glass windows, while the two windows for the EIT copropagating beams are AR/AR coated wedged windows (CVI Laser Optics, W2-IF-025-C-780-0, 30 arcmin wedge, BK7 Glass) mounted on CF flange flexible coupling fittings, to prevent interference effects from multiple internal reflections as light is transmitted through. All CF flanges have been sealed using copper gaskets. Coupling to the turbomolecular pump and, in general, to the outside environment is possible using an all-metal bakeable valve (Nor-Cal Products, Inc., 1.5OD port, 2.75 CFF).

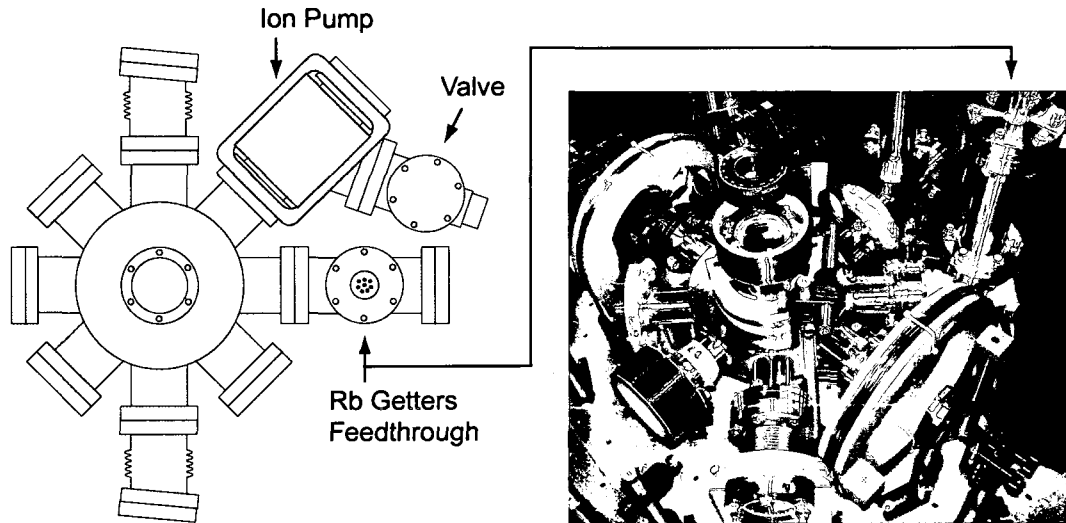


FIG. 16: Rb vacuum chamber. A top view schematic of the vacuum chamber is shown on the left. A picture of the vacuum chamber, shim coils and some optical elements is on the right side; the valve and ion pump are not shown.

Attached to a MOT beam chamber port is a 20 l/s ion pump (Varian Inc.) controlled via a VacIon 921-0062 Pump Control Unit.

Finally, an 8-pin electrical feedthrough has been attached to the vacuum chamber system. To this feedthrough, ten Rb dispensers (SAES Getters USA Inc., Rb/NF/3.4/12 FT 10 + 10) have been welded (three pairs and a quadruple). As current flows through, the dispensers outgas Rb to the desired vapor pressure. For this system, it has been found that to maximize the size and stability of the MOT a current of 3.2 A is needed through a pair of Rb dispensers.

III.3 THE MAGNETO OPTICAL TRAP CONFIGURATION

The optical setup of the magneto optical trap consists of three pairs of counterpropagating trap beams, and three pairs of counterpropagating repumper laser beams, as can be seen in Fig. 17. The trap beams come from an external cavity diode laser, which is coupled to a polarizing maintaining optical fiber cable (OZ Optics, 3 mm OD jacketed, 850 nm, 5/125 μ m PM patchcord), with a polarization extinction ratio (PER) of 28 dB. The repumper beam comes from a separate external cavity diode laser, which is coupled to a single mode optical fiber cable (OZ Optics, 3 mm OD

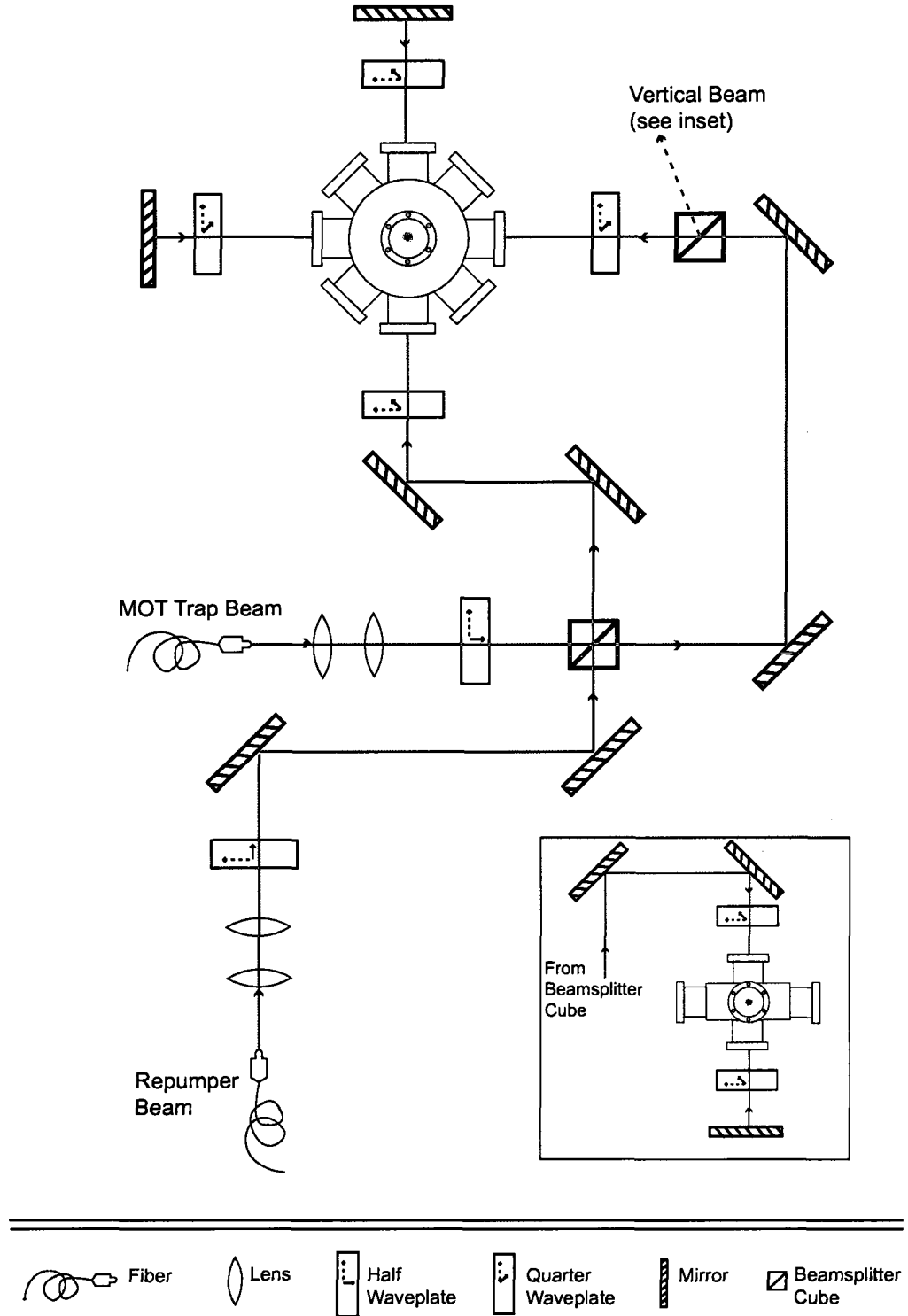


FIG. 17: Magneto optical trap setup. The inset shows the side view of the MOT and the vertical counterpropagating beams. The trapping anti-Helmholtz magnetic field coils and shim coils are not shown.

jacketed, 780 nm, 5/125 μm SM patchcord). Using optical fibers allows the transmission of a single frequency mode as well as preserving the polarization properties of the laser light in the case of the trap beams; it also simplifies the process as the beams are aligned into the vacuum chamber setup. The output from the optical fibers is collimated using an aspheric lens (Thorlabs Inc., C260TM-B $f = 15.36$ mm, 0.16 NA).

The collimated trap beam has an output power of 23.5 mW. It is expanded using a telescope lens system (Thorlabs Inc., LC1054-B $f = -25$ mm and LA1131-B $f = 50$ mm) to a $1/e^2$ radius of 6.3 mm. The polarization of the trap beam is then adjusted using a half waveplate (Thorlabs Inc., WPMH05M-780) in such a way that as the beam proceeds to a polarization beam splitter cube (Melles-Griot, 03 PBS 053, Polarization Laser-Line Beamsplitter Cube for 780 nm) the beam will be split into two beams with an intensity ratio of 1:2. Thus, 1/3 of the beam is directed into the vacuum chamber, and the remaining 2/3 is directed into a 50:50 beam splitter cube (Melles-Griot, 03 BSC 029, Hybrid NIR Broadband). The split beams now have 1/3 of the intensity of the original trap beam and they are directed through different routes into the vacuum chamber. All the mirrors used for beam steering and alignment are NIR Broadband Dielectric (Thorlabs Inc., BB1-E03, fused silica substrate).

Before entering the vacuum chamber, the polarization of the trap beams needs to be adjusted to the necessary circular polarization. This is accomplished using quarter wave plates (Altechna Co. Ltd. $\lambda/4$ phase waveplate for 780 nm AR/AR coated at 780 nm). Once the beams exit the vacuum chamber they are retro reflected using mirrors, and their polarization is also adjusted using quarter wave plates. Considering the incident and retro reflected beams, the estimated trapping laser intensity at the center of the trap is $\simeq 40$ mW/cm²; to have a saturation parameter of 1 the MOT trap laser has been red-detuned by $\frac{5}{2}\Gamma_L$.

The collimated repumper beam has an output power of 200 μW . It is expanded using a telescope lens system (Thorlabs Inc., LC1054-B $f = -25$ mm and LA1131-B $f = 50$ mm) to a $1/e^2$ radius of 0.6 cm, to match the trap beam size. The repumper beam is then directed into the polarization beam splitter cube. Since the polarization of the repumper beam has not been preserved so far, it is split unevenly by the polarization beam splitter. The split beams then overlap and follow the path of the corresponding trap beams.

The magnetic field gradient is created by an anti-Helmholtz coil pair, which is attached externally to the vacuum chamber. These coils are laboratory-built using 35 turns of AWG 14 Cu magnet wire, with an average coil diameter of 8 cm. They are separated a distance of 6.35 cm. For a current of 7.0 A, they can produce at the center of the anti-Helmholtz pair configuration a longitudinal field gradient of 10 G/cm, and a radial field gradient of 5 G/cm. The current can be adjusted; it is delivered by a MASTECH HY3010E variable DC power supply (0 - 30 V / 0 - 10 A), and can be switched on and off using a laboratory-built B-field switch controlled by a pulse generator (Quantum Composers 9614, 100 ns resolution).

There are several stray magnetic fields, such as the earth's field, the residual field from the ion pump, a field due to the gradual magnetization of the optical table and optic mounts and bases over time, fields due to the optical isolators, a field due to the current through the Rb dispensers, and others. These stray magnetic fields can alter the physical location and stability of the MOT, as well as breaking the degeneracy of the relevant ^{87}Rb energy levels, and ultimately alter the EIT lambda scheme. From measurements of the magnetic field surrounding the vacuum chamber, it is estimated that the field at the center of the chamber is less than 1 G. To eliminate it, five shim coils were added, each with a separate power supply. The current through the coils is determined as to balance the residual magnetic field, while balancing its corresponding field gradient.

III.4 CHARACTERIZATION OF THE ULTRACOLD GAS

For quantitative purposes, it is important to determine the shape and size of the ^{87}Rb atomic cloud confined by the MOT, the approximate number of atoms trapped, the temperature achieved by the cooling processes, and the optical depth.

To determine these numbers, the following sets of measurements were performed: fluorescence imaging, absorption imaging, and time-dependent fluorescence.

III.4.1 FLUORESCENCE IMAGING

The detection setup for fluorescence and absorption imaging is shown in Fig. 18. In this setup a 2" achromatic doublet lens (Thorlabs Inc., AC508-150-B $f = 150$ mm) in a 2f - 2f configuration produces an inverted 1 to 1 image of the MOT at location "A" outside of the vacuum chamber; by imaging the MOT we avoid unwanted far-field

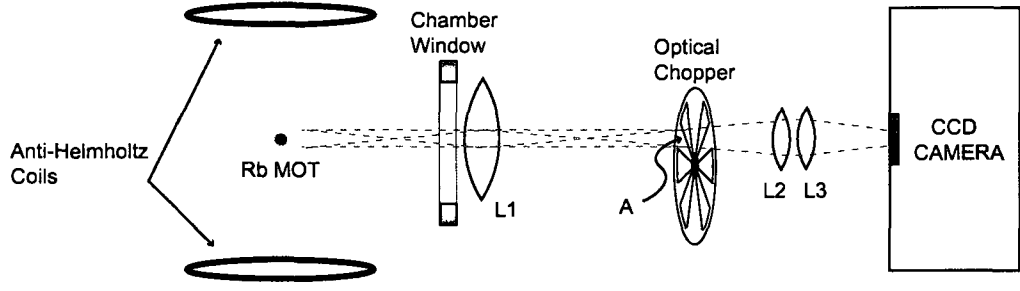


FIG. 18: Detection setup for MOT fluorescence and absorption imaging. L1 is an imaging lens, lenses L2 and L3 capture the image from the chopper location “A” and focus it into the camera. Objects are not to scale.

diffraction effects. An optical chopper (New Focus, Inc. 3501) is placed at location “A” to block, in a controlled manner, any unwanted light into the camera. Two lenses (Thorlabs Inc., LA1608-B $f = 75$ mm) capture the light from location “A” and focus it into a CCD camera with an internal shutter (Princeton Instruments, PIXIS-X0:1024B CCD e2v 1024 * 1024). The image of the cloud is along the radial and axial symmetry directions of the anti-Helmholtz coils.

For the fluorescence imaging measurements, the MOT was on at all times, and the amount of background Rb gas was varied. This was done in order to determine the regime where the vapor pressure was high enough to trap a large number of atoms, but low enough so that collisions were negligible and the density profile can be described by

$$\varrho(r) = \varrho_o e^{-\left(\frac{r^2}{2R_o^2}\right)}, \quad (80)$$

where ϱ_o is the peak density and R_o is the Gaussian radius of the MOT.

Figure 19 shows the cross sections through the center of the MOT image in two orthogonal directions; the left inset is a fluorescence image of the MOT. As can be seen, the MOT is fairly Gaussian, although there is some asymmetry that could be attributed to an imbalance in the radiation forces, an asymmetry of the B-field gradient, or the flow of the Rb atoms from the dispenser. The Gaussian radius $R_o = 0.3$ mm can be determined by a fit of Eq. (80) to this data; this method can only give a first estimate of the Gaussian radius.

As a next step, the ballistic expansion or evolution of the atoms was observed by fluorescence imaging. In these measurements, the MOT trap and repumper lasers,

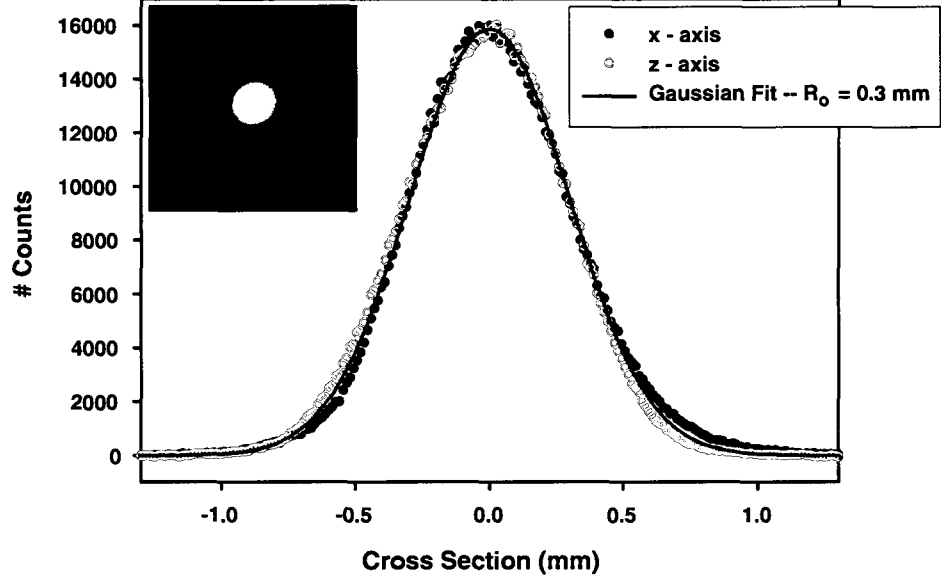


FIG. 19: MOT spatial density distribution. The left inset shows a fluorescence image of the MOT taken by the CCD camera. The cross sections through the center of the Rb cloud in two directions are plotted; a fit of these data demonstrates the Gaussian nature of the density profile, where the Gaussian radius R_0 is estimated to be 0.3 mm.

as well as the trapping magnetic field gradient were turned off, and the cloud was allowed to expand ballistically. After different expansion times, the MOT trap and repumper lasers were turned on for $10 \mu\text{s}$ and the fluorescence from this interaction with the atomic cloud was imaged into the camera. The duty cycle is given by the optical chopper, which for this measurement allowed light into the camera at a rate of 25 Hz.

The expansion of the atomic cloud with respect to time provides a means of measuring the average velocity or kinetic energy of the atoms in the MOT. This in turn provides a definition for the temperature of the atomic cloud. It is important to note that a temperature in a strict thermodynamic sense cannot be ascribed to the MOT, as it is not in thermal equilibrium with its surroundings. However, one can think of an atomic cloud with an average kinetic energy reduced by laser light interactions and that can be naturally described in one dimension as

$$\langle E_k \rangle = \frac{1}{2} k_B T, \quad (81)$$

where k_B is Boltzmann's constant, and T is the temperature [46].

Assuming that the atoms have a Gaussian spatial density distribution as described by Eq. (80) and a Maxwell-Boltzmann velocity distribution $P(v)$ given by

$$P(v)d^3v = \left(\frac{M}{2\pi k_B T}\right)^{\frac{3}{2}} \exp\left(\frac{-m\vec{v}^2}{2k_B T}\right) d^3v, \quad (82)$$

where M is the ^{87}Rb atomic mass, and \vec{v} is the velocity of a particle originating at a point r_o within the atomic cloud at time $t = 0$, then the atomic spatial density can be determined as a function of time by the convolution of these two Gaussian functions [55, 92]. The radius of the expanding cloud as a function of time is given by:

$$R(t) = \sqrt{R_o^2 + (vt)^2}, \quad v = \sqrt{\frac{k_B T}{M}}, \quad (83)$$

from whence the temperature T can be extracted. In addition, we can use this equation to estimate in a more precise way the Gaussian radius R_o at time $t = 0$ of the MOT. Figure 20(a) is a plot of the Gaussian radii of the expanding cloud in the radial (x) and axial (z) directions as a function of time, and the fit to Eq. (83). From this data the temperature is estimated to be on average $77 \mu\text{K}$, below the Doppler limit, and R_o is estimated to be 0.27 mm . Figure 20(b) shows images of the MOT fluorescence taken at different expansion times; the ballistic evolution of the atomic cloud can clearly be seen.

III.4.2 ABSORPTION IMAGING

For the absorption imaging measurements an additional laser beam, a MOT probe beam, was used. It has a $1/e^2$ Gaussian radius of 1.8 mm (much larger than the MOT), linear polarization, and a very low intensity ($I \sim 10^{-3} I_s$). This beam enters the chamber through the window opposite the CCD camera, goes through the cloud of atoms and into the camera.

As the laser's frequency is tuned near the trapping $F = 2 \rightarrow F' = 3$ transition, the atoms will become excited by absorbing light, and the intensity of the MOT probe beam will decrease accordingly. The Lambert-Beer law of linear absorption states that light with an intensity I traveling along a direction z through an absorbing medium with an absorption cross section σ and a density distribution function ρ will be absorbed in the following way:

$$\frac{dI}{dz} = -\rho\sigma I. \quad (84)$$

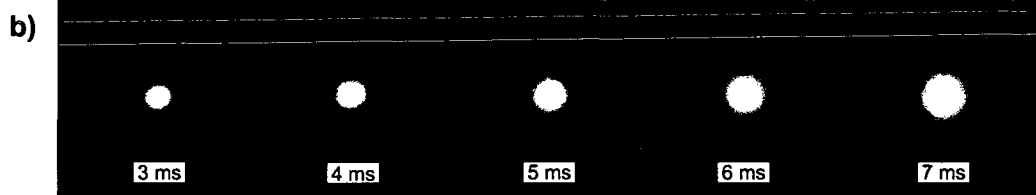
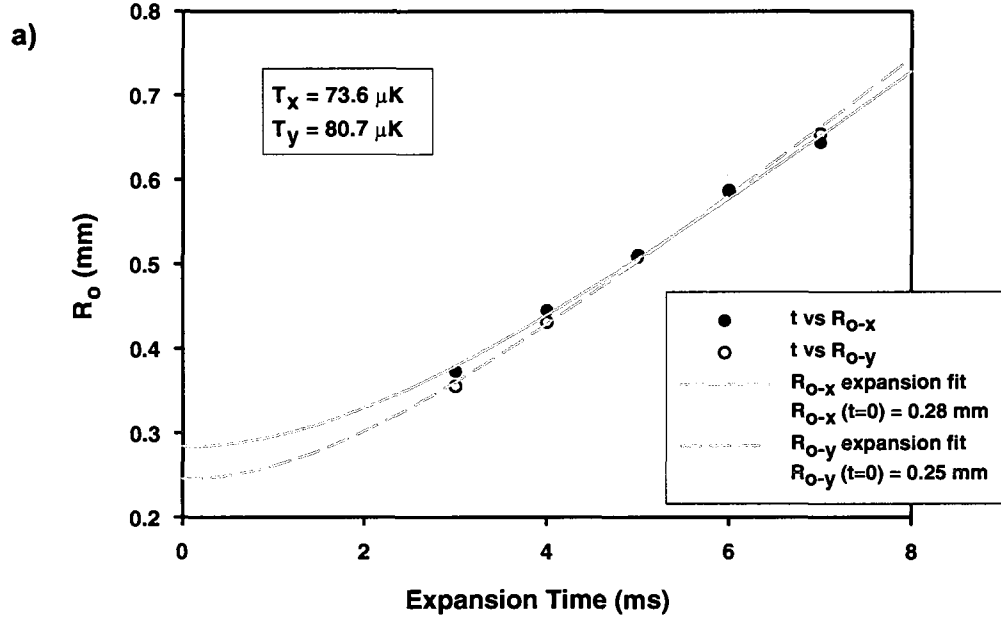


FIG. 20: The ballistic expansion of the ^{87}Rb atomic cloud. (a) The Gaussian radii of the atomic cloud in the radial (x) and axial (z) directions as a function of time. (b) MOT fluorescence for different expansion times.

Solving this equation yields

$$\frac{I}{I_o} = e^{-b'}, \quad b' = \int \varrho \sigma dz. \quad (85)$$

Considering the light that goes through the center of the MOT, where the atom density ϱ_o is highest, and the length of the path traveled by the MOT probe beam is known (given R_o), then the “peak” optical depth can be defined as a function of the resonance detuning-dependent absorption cross section σ :

$$b = \sqrt{2\pi} \varrho_o \sigma R_o, \quad \sigma = \frac{\sigma_o}{1 + 4(\frac{\Delta_L}{\Gamma_L})^2}. \quad (86)$$

Thus, it is possible to measure the optical depth by dividing two CCD images: one of the MOT probe absorption, and one of the MOT probe beam in the absence of the MOT. The MOT probe absorption was taken as follows: the magnetic field gradient, the MOT trap laser and the repumper laser were turned off for a 3 ms to allow fluorescence and scattered light to die away (to minimize background light); then the MOT probe beam was turned on for 5 μ s. and imaged into the camera. The repumper beam was turned on at the same time as the MOT probe beam to prevent optical pumping of the atoms to the $F = 1$ ground state. The duty cycle was given by the optical chopper, which allowed light into the camera at a rate of 40 Hz. This measurement was taken for several MOT probe detunings.

Figure 21(a) shows an image of the MOT probe beam absorption (intensity I), an image of the probe (intensity I_o), and an image of their division (pixel by pixel) I/I_o with the x and z cross sections. From this last image a value for “peak” absorption I/I_o at the center of the atomic cloud can be extracted. Figure 21(b) is a plot of I/I_o as a function of the MOT probe detuning from resonance; a fit to this data according to Eqs. (85) and (86) yields a value of $b = 4.2$ for the optical depth after the MOT has expanded 3 ms. By accounting for the difference in the Gaussian radius of the MOT at $t = 0$ vs. $t = 3$ ms, it is estimated that the maximum optical depth of the MOT at $t = 0$ is $b \simeq 8$.

III.4.3 TIME-DEPENDENT FLUORESCENCE

The detection setup for time-dependent MOT fluorescence measurements is shown in Fig. 22. The MOT trapping and repumper beams and the B-field gradient are turned off. After 1 ms the MOT Probe beam described above is turned on for 15 μ s, with an intensity $I \sim 10^{-2} I_s$. Fluorescence from the Rb cloud is collected by a lens

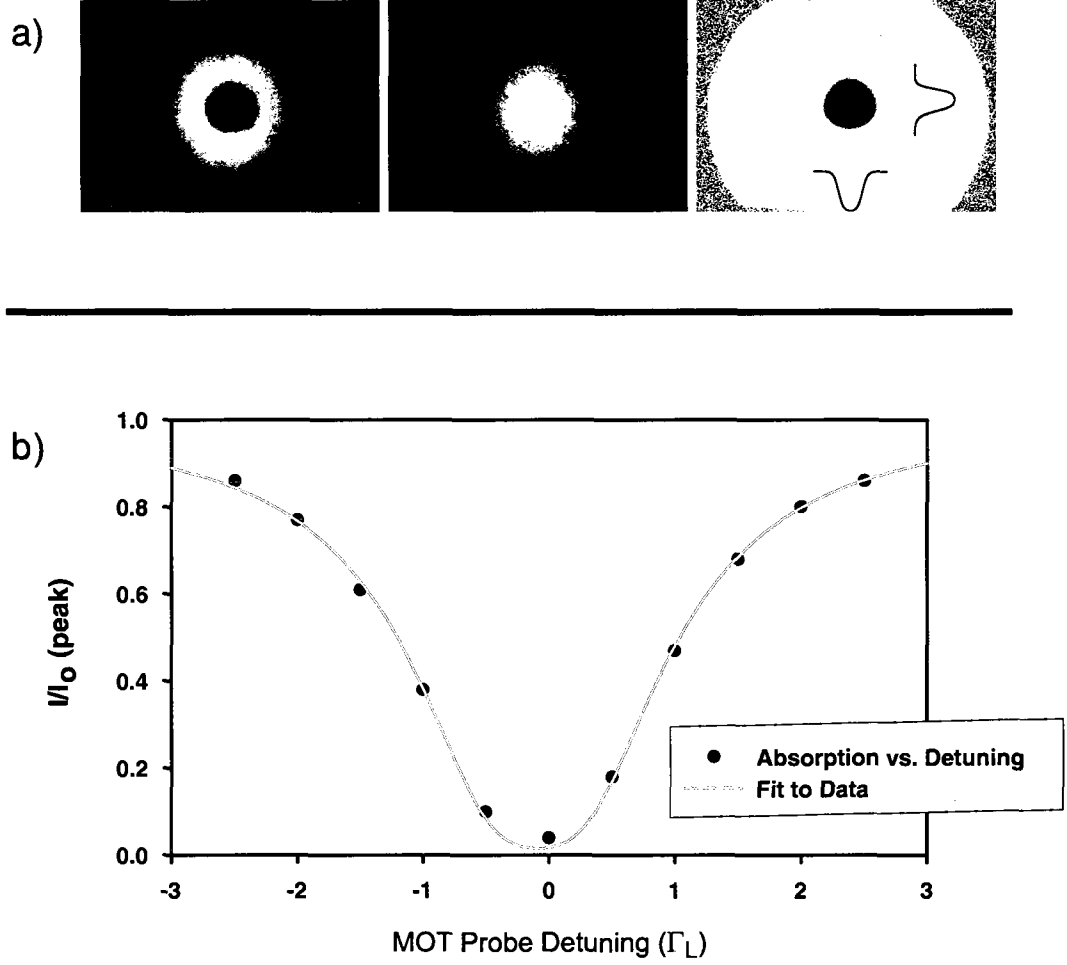


FIG. 21: Detuning-dependent MOT probe absorption measurements. (a) Images of the MOT probe beam absorption (intensity I), the MOT probe beam (intensity I_o), and I/I_o with the x and z cross sections. (b) I/I_o measurements as a function of MOT probe laser resonance detuning; the data was collected after 3 ms MOT expansion time.

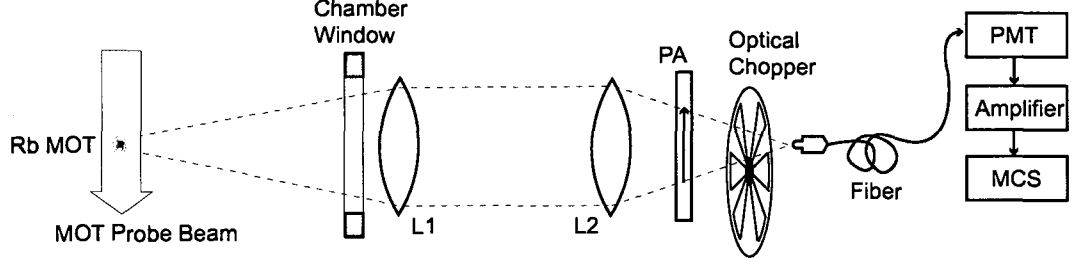


FIG. 22: Time-dependent MOT fluorescence detection setup. L1 and L2 are lenses collecting light from the MOT and focusing it into a fiber. PA is a polarization analyzer, PMT is a photomultiplier tube, MCS is a multichannel scaler.

L1 (Thorlabs Inc., LA1256-B $f = 300$ mm), while a second lens L2 (Thorlabs Inc., LA1401-B $f = 60$ mm) focuses this light into a fiber (Thorlabs Inc., M28L02, $400 \mu\text{m}$, 0.37 NA) which directs it to a GaAs photomultiplier tube (PMT). The signal is then amplified (Phillips Scientific Amplifier Model 778) and time-resolved using a multichannel scaler (Stanford Research Systems SR430). As before, the duty-cycle is given by the optical chopper, which allowed fluorescence to be collected by the fiber at a rate of 40 Hz.

Linearly polarized light incident on an otherwise symmetric ensemble does not cause orientation but it causes alignment of the atomic ensemble. In order to obtain measurements of fluorescence insensitive to the alignment anisotropy, a polarization analyzer at the magic angle $\Theta_M = 54.7^\circ$, with respect to the angle of polarization of the incident light, is placed before the detector [93, 94].

Equation (85) determines the detuning-dependent transmitted intensity of the MOT Probe beam after it has interacted with the Rb atoms in the MOT, which have a Gaussian density distribution. The propagating MOT Probe beam defines an axis of symmetry which makes it convenient to use cylindrical coordinates (ρ, ϕ, z) to describe the system. Since the MOT Probe beam radius is much larger than the MOT radius, it can be approximated by a plane wavefront propagating along the symmetry (z) axis. Thus, the intensity of light after absorption can be found by integrating over z :

$$I(\rho, z) = I_o e^{-be \frac{\rho^2}{2R_o^2}}, \quad (87)$$

where b is the detuning-dependent optical depth defined by Eq. (86).

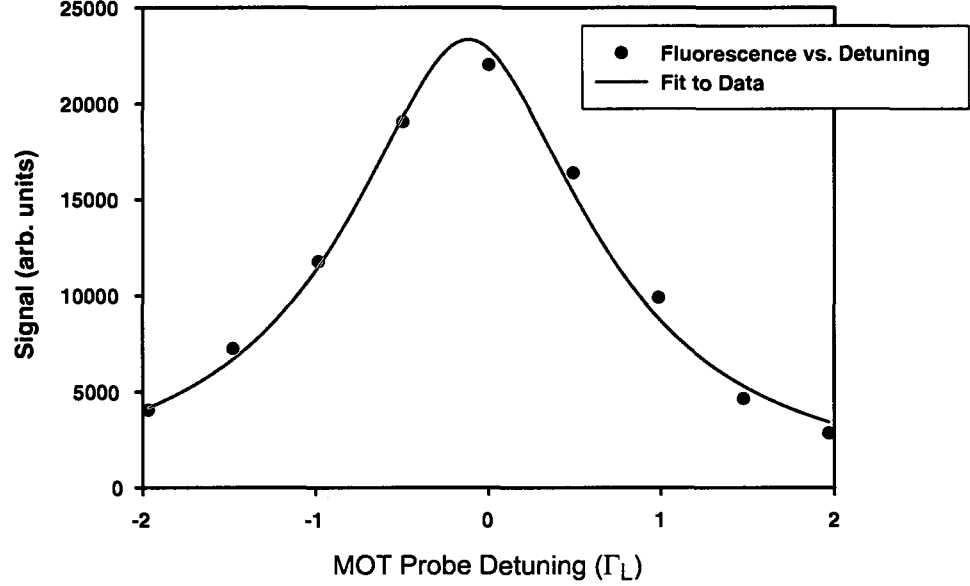


FIG. 23: Detuning-dependent MOT probe fluorescence measurements. The data was collected after 1 ms MOT expansion time. The peak optical depth of the MOT ($b \simeq 8$) can be estimated by fitting this data to Eq. (89). The error bars due to statistical noise are smaller than the data symbols.

The total fluorescence, which is the light absorbed and re-emitted in all directions by the Rb atoms, is given by P , where

$$P = \int \int (I_o - I(\rho, z)) \rho d\rho d\phi. \quad (88)$$

By solving Eq. (88) it can be seen that the fluorescence depends on the optical depth as:

$$P \sim \sum_{m=1}^{\infty} (-1)^{m+1} \frac{b(\Delta_L)^m}{m \cdot m!}. \quad (89)$$

Figure 23 is a plot of the fluorescence signal detected as a function of the MOT Probe laser detuning from the $F = 2 \rightarrow F' = 3$ resonant transition. By fitting Eq. (89) to this data, and accounting for the 1 ms MOT expansion, it is estimated that the peak optical depth of the MOT at $t = 0$ is $b \simeq 8$, in agreement with the result found via the absorption-imaging measurements.

Once the radius R_o and the optical depth b of the MOT are known, it is possible to estimate the peak atomic density ρ_o of the MOT from Eq. (86). For a radius $R_o = 2.7$ mm, $b = 8$, and a resonant cross section $\sigma_o = 1.36 \times 10^{-9}$ cm² (for linearly

polarized light on the $F = 2 \rightarrow F' = 3$ transition), the peak atomic density is $\varrho_o = 8.7 * 10^{10}$ atoms/cm³.

By performing a volume integral over the atomic density distribution given by Eq. (80), the total number of atoms trapped by the MOT can be calculated:

$$N_{tot} = \int \int \int \varrho(r) d^3r = (2\pi)^{\frac{3}{2}} \varrho_o R_o^3, \quad (90)$$

which is found to be $N_{tot} = 2.7 * 10^7$ atoms.

The operation and characterization parameters of the MOT are summarized in Table 3.

TABLE 3: Operation and characterization parameters of the MOT.

MOT Parameter	Value
Trapping Wavelength	780.24 nm
Trapping Laser Intensity	37.7 mW/cm ²
Trapping Laser Detuning	$(\frac{5}{2})\Gamma_L$
Longitudinal B-Field Gradient	10 G/cm
Temperature	77 μ K
Gaussian Radius R_o	0.3 mm
Number of Atoms Trapped N_{tot}	$2.7 * 10^7$
Peak Optical Depth b	8
Peak Atomic Density ϱ_o	$8.7 * 10^{10}$ atoms/cm ³

CHAPTER IV

DATA ACQUISITION AND RESULTS

Since the first beautiful observations of EIT in an ultracold gas [31], the main objective of many experiments has been to achieve propagation of a light pulse, under the best possible conditions, through an EIT prepared medium. Attaining the best possible conditions in the laboratory is not always feasible, hence the relevance of this comparative study, where coherence loss mechanisms, such as diffusion and absence of phase-locking between the control and probe lasers, are taken into account. In this chapter the setup for data acquisition and results will be discussed. In the first section, the laser beams to be used in the EIT measurements are considered, as well as the time sequence for the measurements. The next section presents measurements of a probe light source as it propagates (forward scattering) through an electromagnetically induced transparent Rb vapor cloud. The last section in this chapter presents measurements of the fluorescence (diffusely scattered) light as the same probe light source interacts with the electromagnetically induced transparent medium.

IV.1 INITIAL CONSIDERATIONS FOR EIT MEASUREMENTS

For this project, the three-level Λ scheme used is shown in Fig. 24. The atoms are assumed to be, to an excellent approximation, initially in the $F = 1$ ground state,

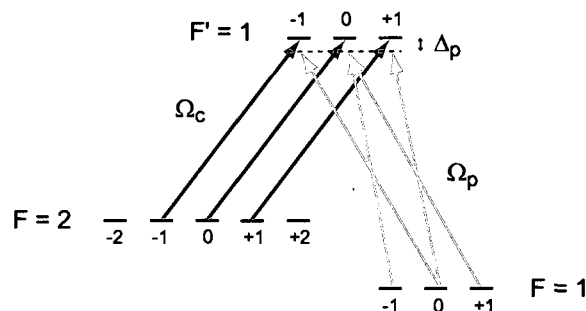


FIG. 24: Relevant hyperfine lambda scheme. The resonant strong coupling laser has Rabi frequency Ω_c . The much weaker probe laser has Rabi frequency Ω_p , and detuning from the atomic resonance of Δ_p .

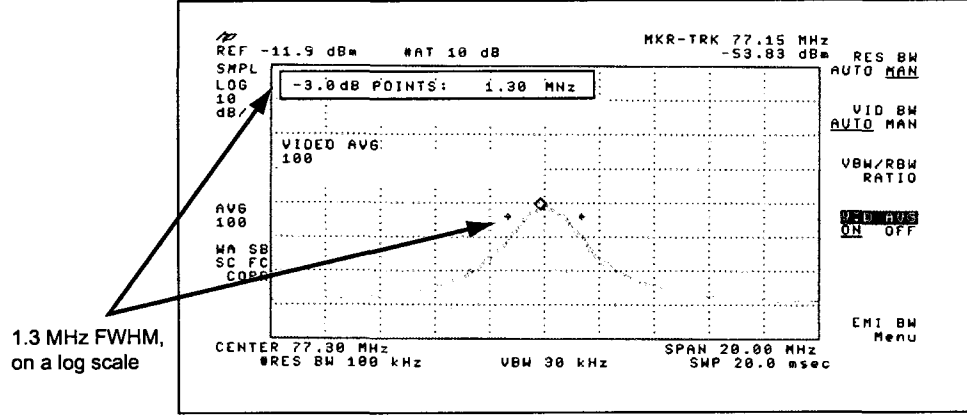


FIG. 25: The coupling and probe laser beams combined bandwidth. The bandwidth is measured by observing their beat note, 1.3 MHz. Shown is a 20 MHz span, averaged 100 times, with a 100 kHz resolution, where the full-width half-maximum (FWHM) value is 1.3 MHz. The data is shown on a logarithmic scale.

through the process of optical pumping. An intense linearly polarized laser beam with Rabi frequency Ω_c couples the $F = 2$ ground state to the $F' = 1$ excited state, and a weak probe pulse with orthogonal linear polarization and Rabi frequency Ω_p is sent through the EIT prepared medium. The frequency of the coupling laser is set to resonance with the atomic transition ($\Delta_c = 0$), while the frequency detuning of the probe laser from the atomic resonance is given by Δ_p .

It must be noted that since the control and probe beam come from separate ECDL beams, they are not phase locked. However, for short enough time durations their relative phase is approximately constant. In this situation, the bandwidth of the lasers becomes relevant. By measuring their beat note, using the optical heterodyning technique [78], it is estimated that the combined bandwidth is 1.3 MHz, as can be seen in Fig. 25. This measurement is performed using a Hewlett Packard Spectrum Analyzer (8595E 9 kHz - 6.5 GHz), and using a 1 GHz photodetector (New Focus, 1601). It is assumed that both lasers have approximately the same frequency profile, since they are both ECDLs built with similar optics, driven by similar electronics and operated under similar conditions. For a Gaussian spectral profile the frequency bandwidth of each laser is 1 MHz.

Since the combined bandwidth of the probe and coupling lasers is $\Delta\nu = 1.3$ MHz, it can be expected that their mutual coherence will decay in $\Delta\tau = \frac{1}{2\pi\Delta\nu} \simeq 120$ ns.

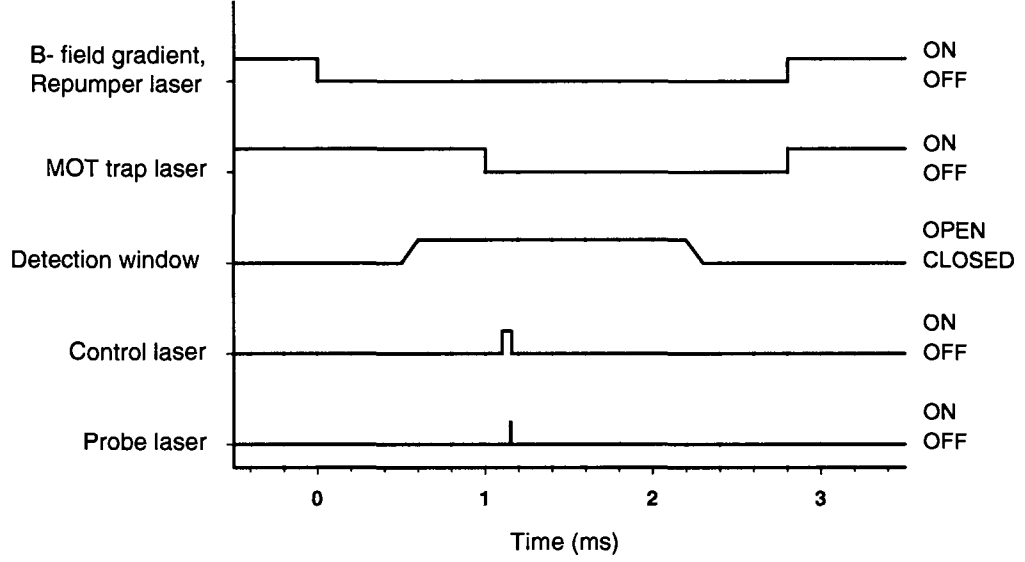


FIG. 26: Data acquisition time sequence. Initially the repumper laser and B-field gradient are turned off for 2.8 ms. After 1 ms the MOT trapping laser is turned off for 1.8 ms. The detection window is open from 0.6 ms to 2.2 ms. At 1.1 ms the control laser is turned on for 60 μ s. The probe pulse is turned on at 1.15 ms, with variable duration.

Thus, a data-acquisition resolution on the order of nanoseconds is needed.

The coupling or control beam has a Gaussian spatial intensity profile, with a radius of $r_{\omega c} = 0.9$ mm, larger than the MOT Gaussian radius ($R_o = 0.3$ mm), so that EIT may be established all through the atomic vapor. The probe beam has a Gaussian spatial intensity profile, and a radius of $r_{\omega p} = 0.2$ mm, smaller than the MOT Gaussian radius, so that this laser can probe through the center of the MOT, where the optical density is largest.

The Rb atoms collected in the MOT are in the $F = 2$ higher energy ground hyperfine level; to transfer them to the $F = 1$ ground level they are optically pumped for 1 ms. The data acquisition sequence is shown in Fig. 26; it begins by turning off the repumper laser and the current to the anti-Helmholtz coils providing the trapping magnetic field gradient for 2.8 ms. The MOT trapping laser remains on 1 ms longer; in this period approximately 86% ($1/e^2$) of the atoms are transferred to the $F = 1$

ground level. The data acquisition window opens as the chopper blades move before the detector, and data acquisition can begin at 0.6 ms for a period of 1.6 ms. The control laser is turned on 100 μs after the MOT trap laser is off, at 1.1 ms; the control pulse is 60 μs long. As mentioned in Chapter II, this control or coupling field prepares the system in a dark or non-coupling state $|NC\rangle$, as given by Eq. (38), where $\Omega_p = 0$. Finally, the probe pulse (of variable duration) is turned on 50 μs after the control pulse, at 1.15 ms. The duty cycle is given by the chopper, with a frequency of 40 Hz.

IV.2 TRANSMISSION OF A PROBE PULSE PROPAGATING THROUGH A COHERENTLY PREPARED RB CLOUD

This comparative study begins by observing the behavior of a probe pulse transmitted through a ^{87}Rb vapor cloud under conditions of EIT.

A schematic setup for the detection of a transmitted probe pulse is shown in Fig. 27. A coupling laser with frequency ω_c prepares the system in a dark state, while a weak laser pulse with frequency ω_p probes the system. To avoid saturation of the detector, the coupling laser has been offset by 2° from the probe pulse propagation axis. A polarization analyzer PA (Newport, Polacor 10P109AR.16) selects light with the same polarization as the incident probe pulse. A lens L1 (Thorlabs Inc., LA1401-B $f = 60$ mm) focuses the transmitted light into a fiber (Thorlabs Inc., M28L02, 400 μm , 0.37 NA) which directs it to a GaAs PMT. The signal is then

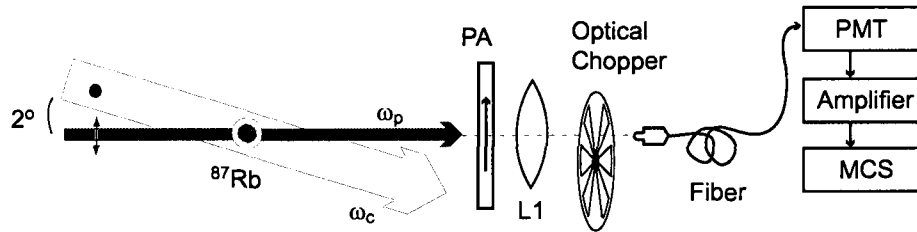


FIG. 27: Experimental setup for detection in transmission of a probe pulse through the EIT prepared medium. The coupling laser has a frequency ω_c . The probe laser has a frequency ω_p . A lens L1 collects the probe pulse transmitted through the Rb cloud and launches the beam into a fiber. PA is a polarization analyzer, PMT is a photomultiplier tube, MCS is a multichannel scaler.

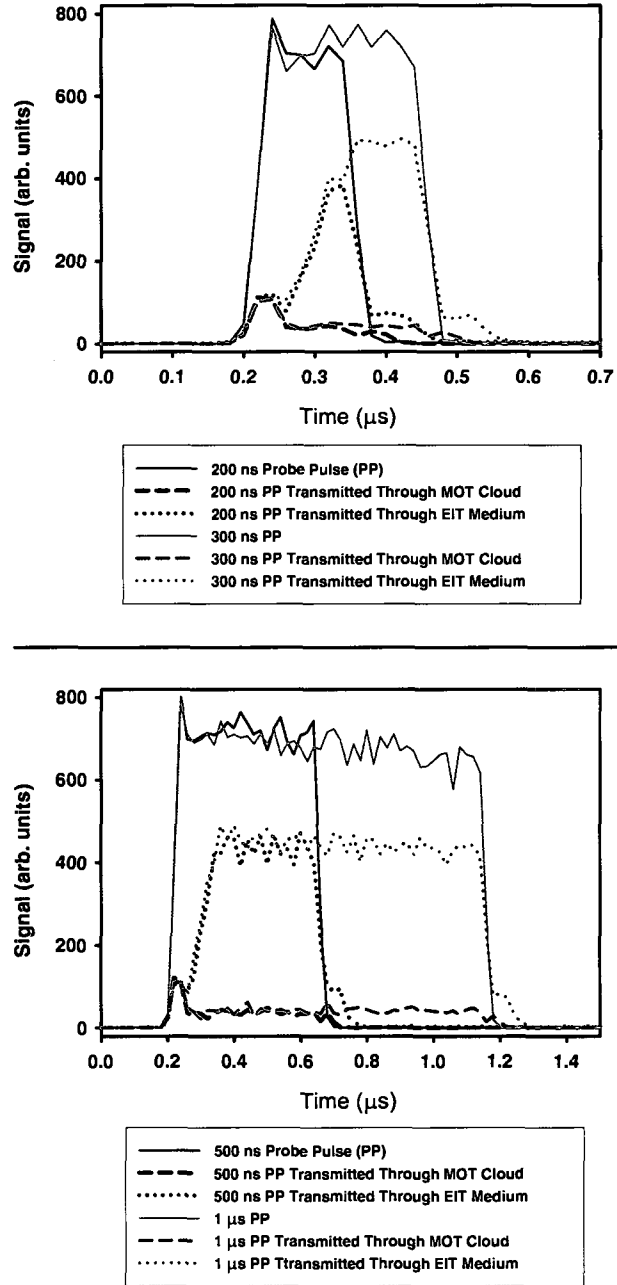


FIG. 28: Relative signal comparison for variable probe pulse duration. $\Omega_c = 1.1 \Gamma_p$, $\Delta_p = 0$. For each pulse duration three sets of data were taken: detection of the probe pulse, transmission of the probe pulse through the MOT cloud, and transmission of the probe pulse through the atomic cloud when the coupling laser had been previously turned on. The control field is turned on 50 μs before the probe pulse, and stays on for 60 μs .

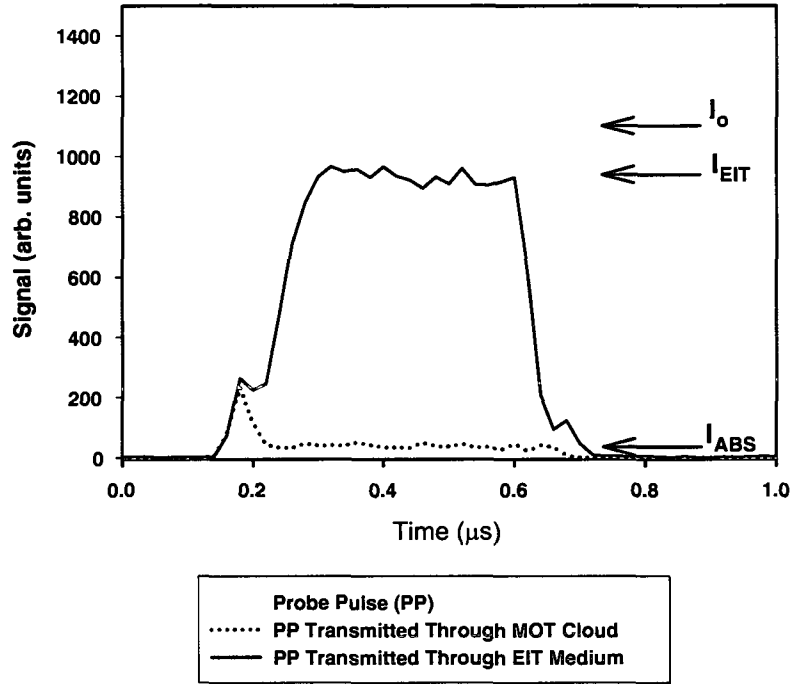


FIG. 29: Calibration set of measurements. Three measurements were taken daily for calibration purposes: the probe pulse, the same pulse after absorption by the MOT cloud, and the probe transmitted through an EIT prepared cloud. The optical depth and transparency of the cloud can be determined by comparison of the steady-state intensity values I_o , I_{ABS} , and I_{EIT} . This set of measurements was taken for a 500 ns pulse, $\Omega_c = 1.45 \Gamma_p$, $\Delta_p = 0$. The control field is turned on 50 μs before the probe pulse, and stays on for 60 μs .

amplified (Stanford Research Systems SR445A - 350 MHz Preamplifier) and time-resolved using a multichannel scaler (Stanford Research Systems SR430).

The first observations of EIT in transmission had probe pulses of different lengths; the results are presented in Fig. 28. For these measurements, both lasers were tuned to the resonance of their respective (unperturbed) atomic transition. It is useful to express the Rabi frequency in terms of the natural linewidth of the atomic transition, $\Gamma_p = 6.1$ MHz. The coupling laser had a Rabi frequency of $\Omega_c = 1.1 \Gamma_p$. For each instance three sets of data were taken. The first was a measurement of the undisturbed probe pulse, the second was a measurement of the transmission of the probe pulse through the MOT ^{87}Rb cloud, and the third was a measurement

of the transmission of the probe pulse when the Rb cloud had been prepared for transparency by the coupling laser. It is clear from these measurements that a 200 ns pulse is not of enough duration to establish a steady-state transparency through the atomic cloud; a 300 ns pulse is long enough for a steady-state transparency to develop, although a 500 ns pulse would provide better steady-state statistical averaging. No new information is acquired by longer probe pulses. The time resolution of this data is 20 ns.

Before any group of measurements, an initial set of three measurements was taken for calibration measurements. The first one is the probe pulse, which is too weak to be detected by the power meters available. The second one is the probe transmitted through the MOT atomic cloud (suffering regular absorption). This measurement is necessary in order to determine the optical depth of the cloud through which the probe is transmitted, since the location and density of the MOT may vary day to day due to acoustic, magnetic, and environmental noise. The third measurement is the transmission of the probe when the coupling laser has been turned on, to measure the transparency. Figure 29 shows one such set of measurements, with a 20 ns resolution. Comparison of the steady-state average of the absorbed pulse through the MOT cloud (I_{ABS}) with the steady-state average probe pulse intensity (I_o), and recalling Eq. (85), shows that the optical depth of the atomic cloud was $b = 3.4$ for this particular set of measurements. Likewise, comparison of the steady-state EIT signal detected I_{EIT} to I shows an 84% transparency.

It should be noted that the incident probe pulse is not exactly temporally square; it has an estimated rise and fall time of 40 ns. The pulse initially overshoots (about 10% above the main signal), this is due in part to initial overshooting of the AOM that controls the switching on of the pulse. This overshoot does not take place when the AOM switches off. Another effect contributing to the signal when the probe pulse switches on/off could be a Sommerfeld-Brillouin optical precursor [95, 96]. When a step-modulated monochromatic pulse is abruptly turned on, because of the finite response time its leading edge ideally does not interact with the medium, traveling through at speed c . The front wave is followed by high and low frequency components that form a transient wave, known as an optical precursor. The precursor intensity decay time is given by $\tau_{op} = \frac{1}{2\Gamma_p} \simeq 80$ ns; this effect also happens when the pulse is switched off. The leading edge feature is particularly apparent in Fig. 29 for a probe pulse transmitted through a MOT cloud experiencing regular absorption.

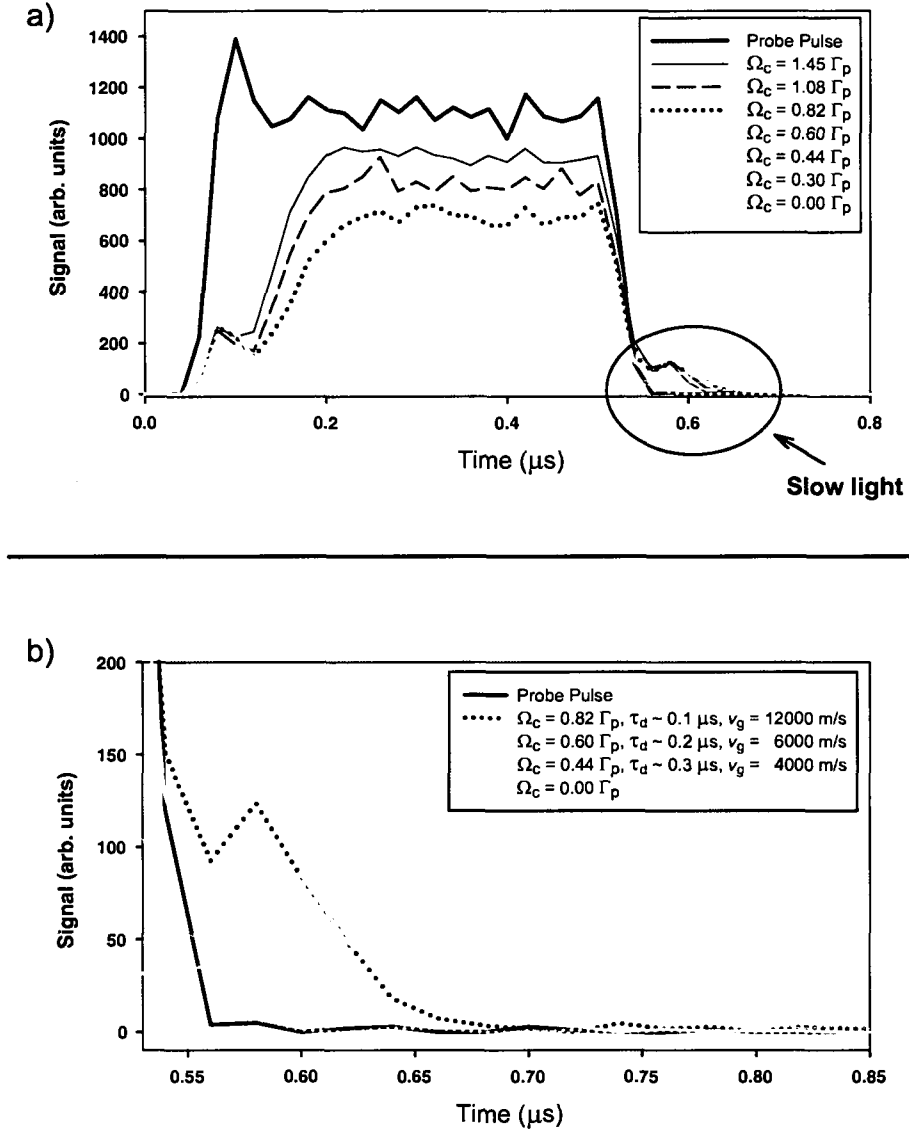


FIG. 30: EIT signal as a function of Ω_c . (a) Time evolution of the transmitted EIT pulse for varying Ω_c . The pulse is 500 ns long, on resonance ($\Delta_p = 0$). The slow light components usually associated with optical information storage can be seen. (b) Expansion of the slow light pulses for some Ω_c , and their approximate delay time τ_d . The probe pulse in the absence of a sample, and the probe pulse when there is no coupling laser ($\Omega_c = 0$), are included for comparison. The group velocity corresponding to traveling through an atomic sample with Gaussian radius $r_o = 0.3$ mm in a time τ_d is included as well. The control field is turned on 50 μs before the probe pulse, and stays on for 60 μs .

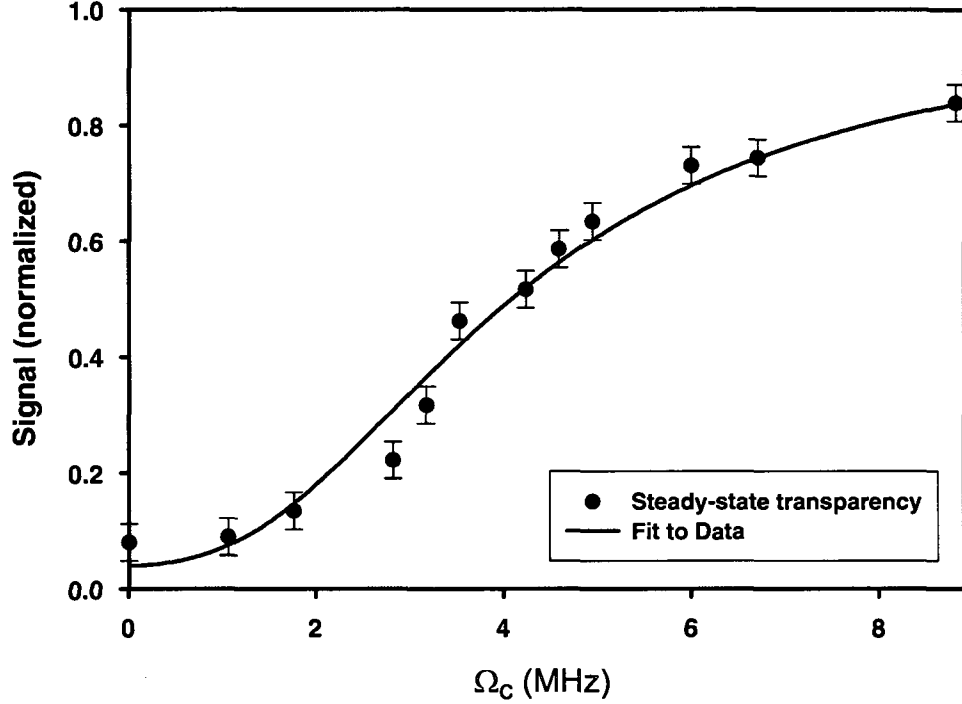


FIG. 31: Intensity of the steady-state transmitted EIT signal as a function of Ω_c . The probe field is on resonance ($\Delta_p = 0$). The signal is normalized to the peak intensity of the undisturbed probe pulse.

For an optical depth of $b = 3.4$, measurements were taken to compare the time evolution and intensity of the transparency as a function of the intensity, or Rabi frequency Ω_c , of the control laser. The measurements have a 20 ns resolution.

In Figure 30(a), the time evolution dependence is presented, for a resonant probe $\Delta_p = 0$. Clearly, the transparency develops in all cases regardless of the coupling field strength, but it reaches a steady state faster for higher values of Ω_c , as was pointed out by Jyotsna and Agarwal [97]. In these data the delayed pulses associated with slow light or coherent optical information storage can be seen as well. Figure 30(b) shows some of the slow light pulses. The slow light pulses associated with low values of Ω_c are not included because the signal is too weak and extended in time to make any qualitative observations, and the slow light pulses associated with high values of Ω_c are not included because the pulse has an estimated time delay shorter than the time τ_{op} it takes an optical precursor to decay. The probe pulse in the absence of a sample, and the probe pulse when there is no coupling laser ($\Omega_c = 0$), are included

for comparison. It can be observed that for a weaker coupling laser or lower Ω_c the delay is greater, and the delayed light propagates slower with a group velocity v_g given by Eq. (67). A pulse propagating with this slow group velocity through a sample with Gaussian density distribution, given by Eq. (80), and optical depth b , will experience a time delay with respect to the probe pulse in the absence of a sample of $\tau_d = b\Gamma_p/|\Omega_c|^2$. The time delay shown for the slow light pulses is just an approximation, since this formula ignores the laser's bandwidth and the ground states decoherence rate. A 500 ns pulse traveling at the speed of light is 150 m long. Considering that the pulse gets compressed by a ratio c/v_g , that means that the pulse is compressed to a few mm.

Figure 31 is a comparison of the steady-state transparent light transmitted as a function of the coupling field Rabi frequency Ω_c . The signals have been normalized to the peak intensity of the undisturbed probe pulse; this would correspond to a 100% transparency. The main source of uncertainty are laser intensity fluctuations; statistical noise is smaller than the data symbols. A fit of this data to Eq. (60), where $z \rightarrow \sqrt{2\pi}r_o$ for a Gaussian atomic density distribution, and χ_i is given by Eq. (59), yields a ground states decoherence rate of $\Gamma_g = 0.4 \text{ MHz} = 0.07 \Gamma_p$. The phase fluctuations of the lasers are reflected in the ground states decoherence rate Γ_g ; this smaller value of Γ_g supports the earlier claim that for pulses of short duration (hundreds of nanoseconds), and lasers of similar characteristics (bandwidth, wavelength, electronic and environmental conditions) the relative phase between the control and probe lasers is relatively stable.

Next, measurements were taken to determine the transparency dependence with respect to the probe detuning Δ_p , and are presented in Fig. 32; the data has been normalized to the intensity of the probe pulse, which would correspond to 100% transparency. For an optical depth of $b = 5.5$, and a coupling laser Rabi frequency $\Omega_c = 0.69 \Gamma_p$, the sub-natural transparency width can be readily seen in Fig. 32(a). That the medium is not even more highly transparent is a result of a non-zero ground states decoherence rate Γ_g . In the second set of measurements, Fig. 32(b), for a higher coupling laser Rabi frequency $\Omega_c = 1.45 \Gamma_p$, and an optical depth of $b = 3$, it can be seen that as the control laser intensity is increased the width of the transparency window increases, in accordance with Eq. (62), and the medium becomes more transparent, for the same ground states decoherence rate. This second set of measurements satisfies the requirement that $|\Omega_c| \gg \Gamma_g$, so Eq. (62) can be used

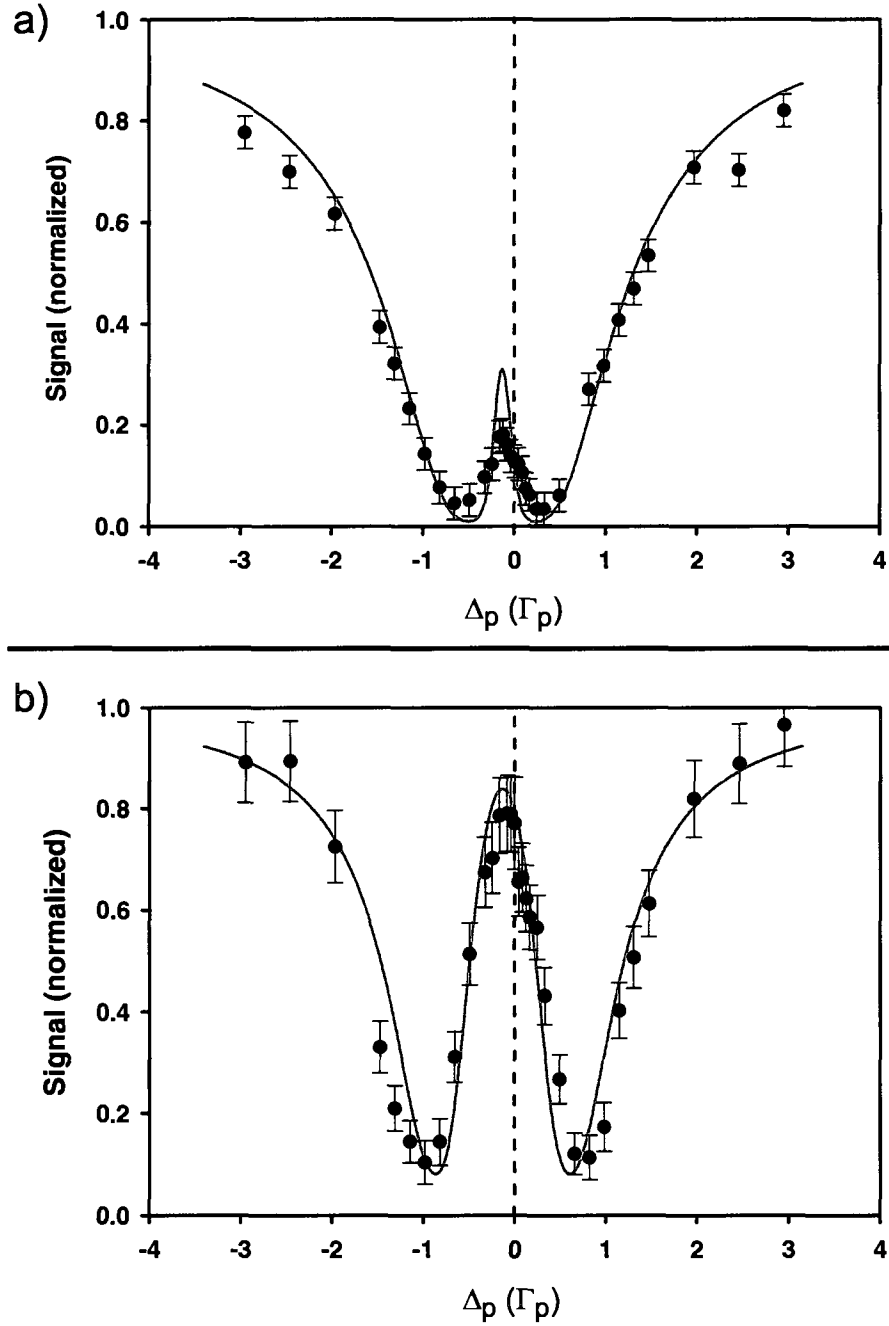


FIG. 32: Probe frequency detuning dependence of the EIT transmission signal. (a) $b = 5.5$, $\Omega_c = 0.69 \Gamma_p$. (b) $b = 3$, $\Omega_c = 1.45 \Gamma_p$. The circles correspond to data normalized to the probe pulse intensity. The solid lines are calculated for the specified Ω_c , b , and $\Gamma_g = 0.07 \Gamma_p$, for an ideal three-level atom.

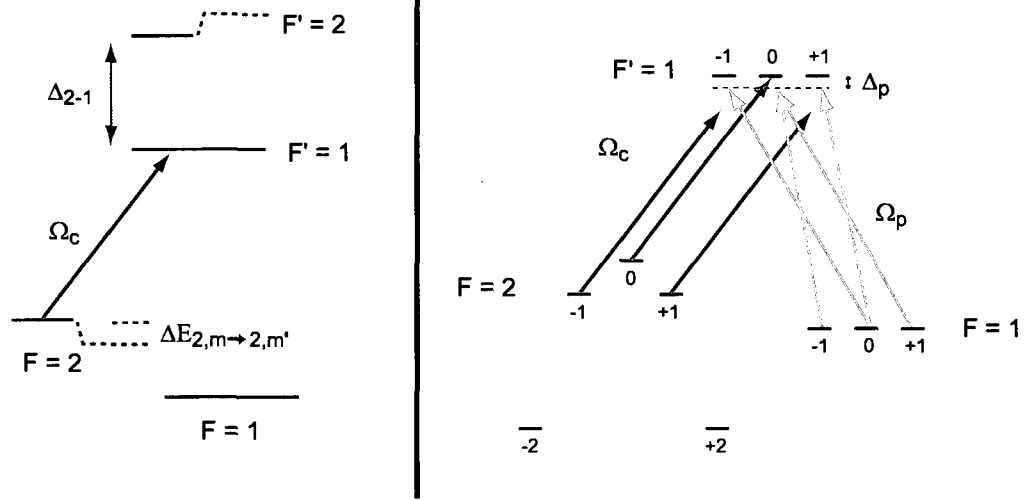


FIG. 33: Light shift of the $|2\rangle \rightarrow |1\rangle$ transition caused by the control laser field coupling the $|2\rangle \rightarrow |2\rangle$ transition. As a result of the shift in the Zeeman levels, some EIT Λ 's will be red detuned, and their contribution to the total transparency will be less than that for the ideal case when $\Delta_p = \Delta_c = 0$.

to estimate the FWHM of the transparency; the predicted value is $\Delta_{EIT} = 0.7 \Gamma_p$, which is in good agreement with the data.

The solid lines in Fig. 32 are calculated probe detuning dependent EIT transmission curves, for an ideal three-level atom, with the indicated experimental parameters. It can be seen that in both sets of measurements the transparency center is shifted to frequencies below $\Delta_p = 0$ (red-detuned), and it is wider than the calculated transparency. The reason behind this discrepancy is that ^{87}Rb is not an ideal three-level atom, and in a realistic EIT scheme the hyperfine and Zeeman structures of the atom become relevant.

Figure 33 shows how the hyperfine structure affects the transparency. Consider for example the effect of the coupling laser on the $F = 2 \rightarrow F' = 2$ transition. The level $F' = 2$ is detuned by Δ_{2-1} from the $F' = 1$ level. The interaction between the atom and the control laser will induce a light shift given by

$$\Delta E_{2,m \rightarrow 2,m'} = \frac{\hbar}{2} \left(-\Delta_{2-1} \mp \Omega'_{2,m \rightarrow 2,m'} \right), \quad (91)$$

where $\Omega'_{2,m \rightarrow 2,m'} = \sqrt{\Omega_{2,m \rightarrow 2,m'}^2 + \Delta_{2-1}^2}$, and $\Omega_{2,m \rightarrow 2,m'}$ depend on the ground and excited Zeeman levels being coupled by the control field. For this particular case, the $|F = 2, m = 0\rangle \rightarrow |F' = 2, m' = 0\rangle$ transition is not dipole-coupling allowed,

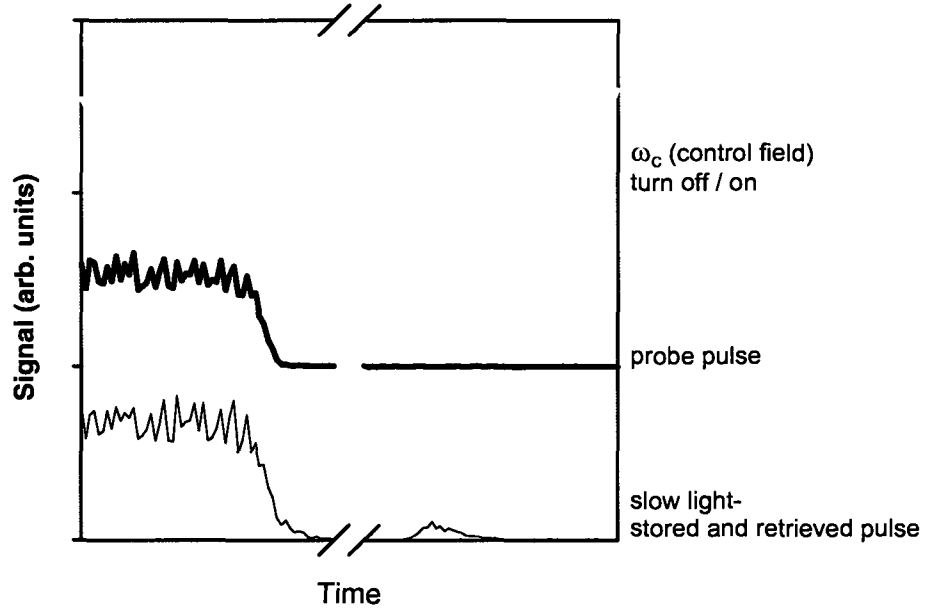


FIG. 34: Slow light storage and retrieval representative timing diagram. The relative timing of the control and probe fields with respect to a representative stored and retrieved slow light signal is shown.

so the $m, m' = 0$ levels are not shifted. The $|F = 2, m = \pm 1 \rangle \rightarrow |F' = 2, m' = \pm 1 \rangle$ coupling is allowed, and results in a light shift of the $m, m' = \pm 1$ levels. Likewise, the $|F = 2, m = \pm 2 \rangle \rightarrow |F' = 2, m' = \pm 2 \rangle$ transition is allowed, and the $m, m' = \pm 2$ levels are light shifted by a larger amount. The presence of other hyperfine levels produce qualitatively similar results (see Fig. 6 for the ^{87}Rb hyperfine structure). As a consequence of these differing sublevel light shifts, the different Λ schemes contribute in a more complex way to the transparency. Some Λ 's will be shifted to frequencies below $\Delta_p = 0$, which results in the transparency window red-shifts observed in Fig. 32. The transparency produced by the red-shifted Λ 's will not be as large as that of the ideal case, when $\Delta_p = \Delta_c = 0$. This splitting of the transparency as a function of Δ_p accounts for the larger transparency width and wings observed in Fig. 32.

Finally, a set of measurements was taken to determine the system's capabilities for storage and retrieval of light pulses. Figure 34 shows qualitatively the relative timing of the control and probe pulses with respect to the stored and retrieved slow light signal. The control field (ω_c) and the probe pulse are turned off at the same

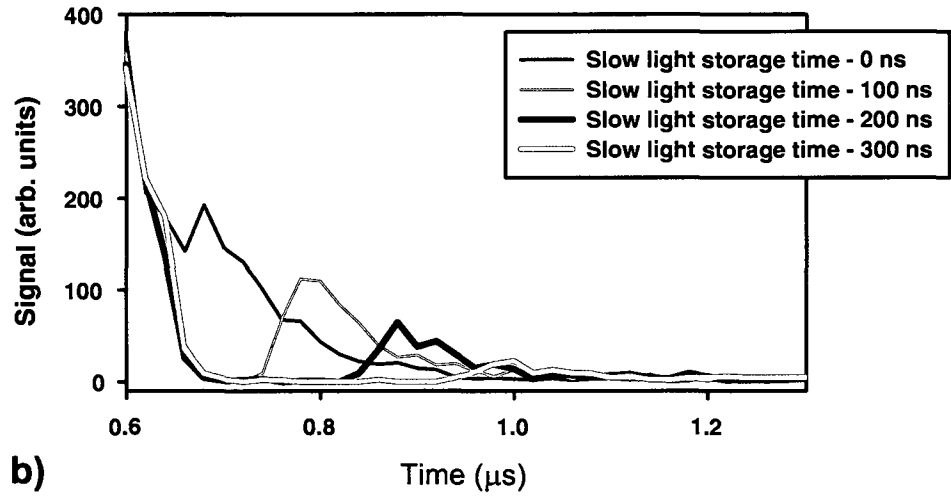
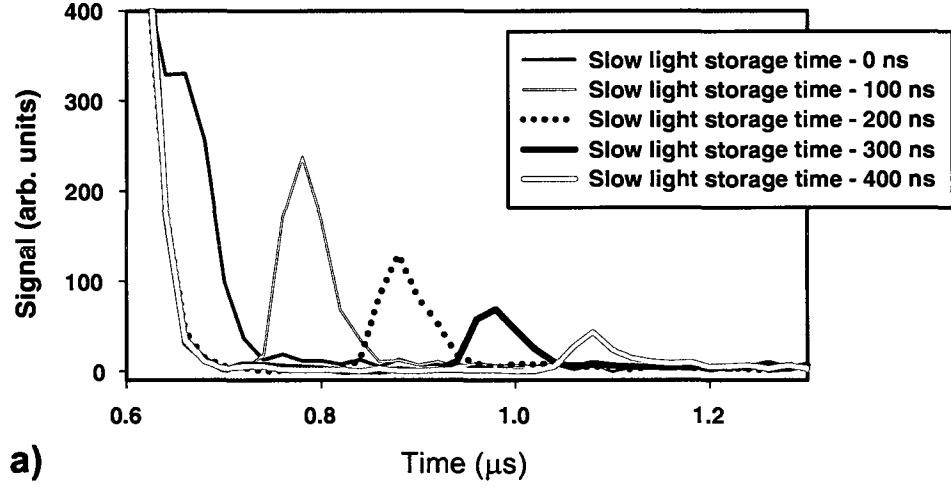


FIG. 35: Slow light storage and retrieval with variable delays. (a) $\Omega_c = 1.45 \Gamma_p$, (b) $\Omega_c = 0.69 \Gamma_p$.

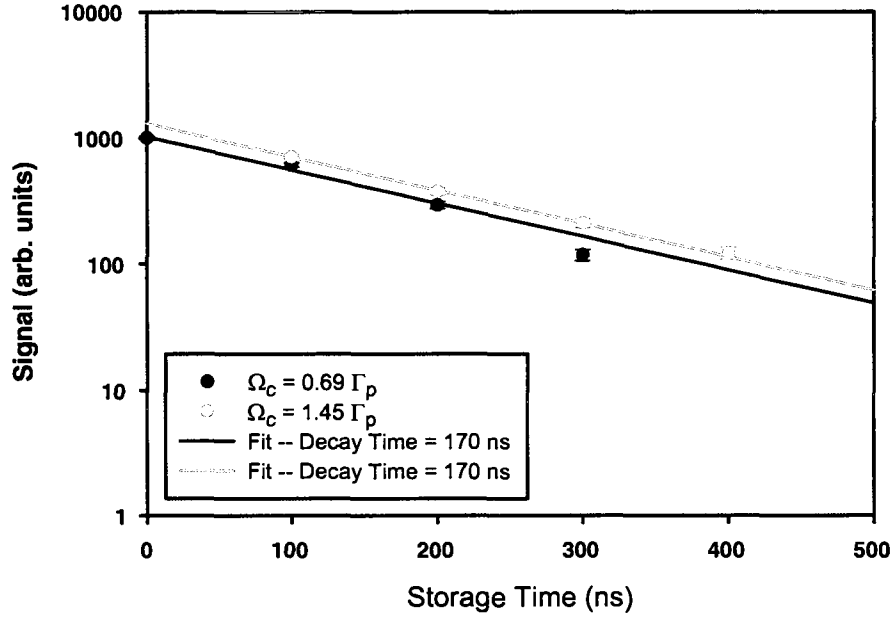


FIG. 36: Slow light retrieval signal for variable storage times. The data is taken for $\Omega_c = 1.45 \Gamma_p$, and $\Omega_c = 0.69 \Gamma_p$. The solid lines are fits to the data, which yield a $1/e$ decay rate of the atomic coherence of 170 ns.

time, and the control field is switched back on after some time interval. When the control field is turned back on, the stored slow light pulse is retrieved, as can be seen in this figure. It is important to notice that the control field does not overshoot when it turns on, as opposed to the probe field, and that it turns off slightly faster than the probe pulse.

For an optical depth of $b = 2.9$, and $\Delta_p = \Delta_c = 0$, measurements were taken for two different control field intensities. The data in Fig. 35(a) is taken for a control laser Rabi frequency of $\Omega_c = 1.45 \Gamma_p$, while for Fig. 35(b) the Rabi frequency is $\Omega_c = 0.69 \Gamma_p$. For these measurements, the control field was switched off at $t = 0.6 \mu\text{s}$, and switched back on with variable time delays. The regenerated slow light pulses demonstrate that a polariton was stored in the atomic sample, and that it can be retrieved. To our knowledge this is the first report of storage and retrieval of light pulses with phase unlocked control and probe lasers, i.e. with non-negligible ground state decoherence rate Γ_g . Although the incident probe pulse is an approximately square pulse, the output pulse is not, in agreement with Datsyuk et al. [43], due

to the dispersion of the medium and the interaction with an atomic medium with Gaussian density distribution. For these measurements, the condition for adiabatic evolution of the system, given by Eq. (41), during the turn-off of the control and probe pulses is satisfied, according to our estimates which are presented in Appendix B.

Figure 36 is a plot of the transmission of the probe pulse versus storage time for the two sets of measurements shown in Fig. 35. The solid lines are fits to the data, which give a $1/e$ decay time of the atomic coherence of 170 ns, or a decoherence rate of 0.9 MHz ($0.15 \Gamma_p$). We associate this larger decoherence rate to the linewidth (1 MHz) of the control laser, which becomes relevant when the control field is switched back on.

IV.3 FLUORESCENCE OF A PROBE PULSE PROPAGATING THROUGH A COHERENTLY PREPARED RB CLOUD

The sets of measurements taken for fluorescence detection of a probe pulse propagating through an EIT prepared medium follow closely those measurements taken for transmission. The data was self-calibrated with measurements of the probe fluorescence from the MOT right before and after each data point.

A schematic setup for the detection of fluorescence is shown in Fig. 37. A control laser with frequency ω_c prepares the system in the dark state $|NC\rangle$, while 50 μ s later a weak laser pulse with frequency ω_p probes the system. The probe and control lasers have linear mutually orthogonal polarization. A polarization analyzer PA (Newport, Polacor 10P109AR.16) selects light with the same polarization as the control laser, as can be seen in this figure. A lens L1 (Thorlabs Inc., LA1256-B $f = 300$ mm) collects and collimates fluorescence coming from the location of the MOT, and a lens L2 (Thorlabs Inc., LA1401-B $f = 60$ mm) focuses the fluorescence into a fiber (Thorlabs Inc., M28L02, 400 μ m, 0.37 NA) which directs it to a GaAs PMT. The signal is then amplified (Stanford Research Systems SR445A - 350 MHz Preamplifier) and time-resolved using a multichannel scaler (Stanford Research Systems SR430).

The fluorescence generated by the probe pulse as it is scattered by the coherently prepared Rb sample, as a function of the control field Rabi frequency Ω_c , is presented in Fig. 38.

First, consider the fluorescence signal when the coupling laser Rabi frequency is $\Omega_c = 0$. The decay of scattered light from an optically thick cloud has been studied

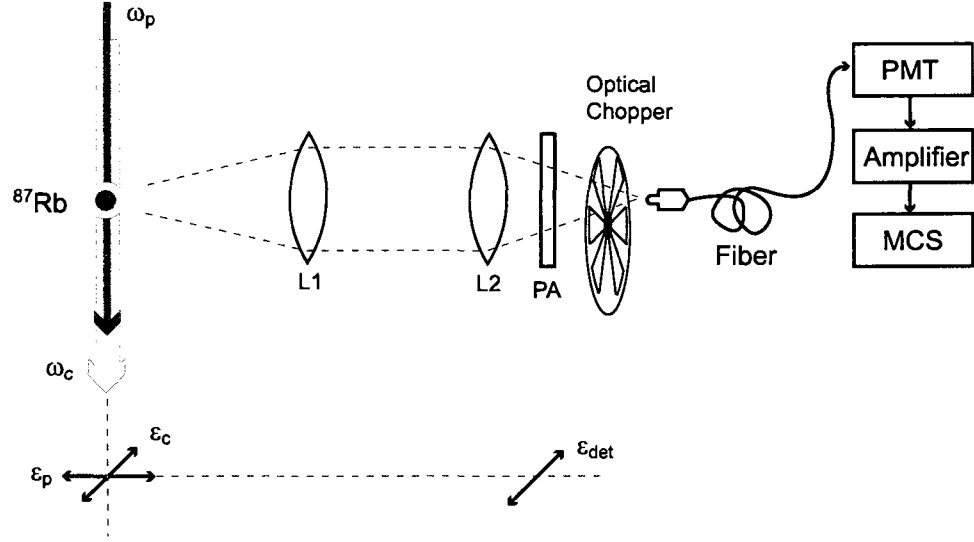


FIG. 37: Experimental setup for detection of fluorescence from a probe pulse propagating through the EIT prepared medium. The coupling laser has a frequency ω_c . The probe laser has a frequency ω_p . A lens L1 collects fluorescence emitted from the atomic cloud, while a lens L2 focuses this light into a fiber. PA is a polarization analyzer, PMT is a photomultiplier tube, MCS is a multichannel scaler. The probe and control lasers have linear mutually orthogonal polarization. The detected polarization is parallel to the control field polarization. ϵ_p , ϵ_c , and ϵ_{det} are the probe, control, and detected light polarization vectors respectively.

by Labeyrie et al. [67]. For an inhomogeneous Gaussian density sample, with optical depth $b \gg 1$, the fluorescence will decay in a time τ_f given by

$$\tau_f \simeq \frac{3b^2\tau_{nat}}{5.35\pi^2}, \quad (92)$$

where τ_{nat} is the natural lifetime of the atomic transition. This equation is strictly applicable to media with large b ; we use it here to estimate an upper limit of the optical depth b of the sample. From the previous equation, and a fit to the decay of the probe fluorescence ($\Omega_c = 0.00 \Gamma_p$, Fig. 38) an upper limit of $b = 6$ can be obtained. In general, the measured optical depth is $b = 4(1)$.

Second, in Fig. 38 the transient turn-on of the fluorescence signals for $\Omega_c > 0$ does not exhibit the sharp increase observed in the transmission signals (see Fig. 30). For the transmission data, it was suggested that this feature could be associated with

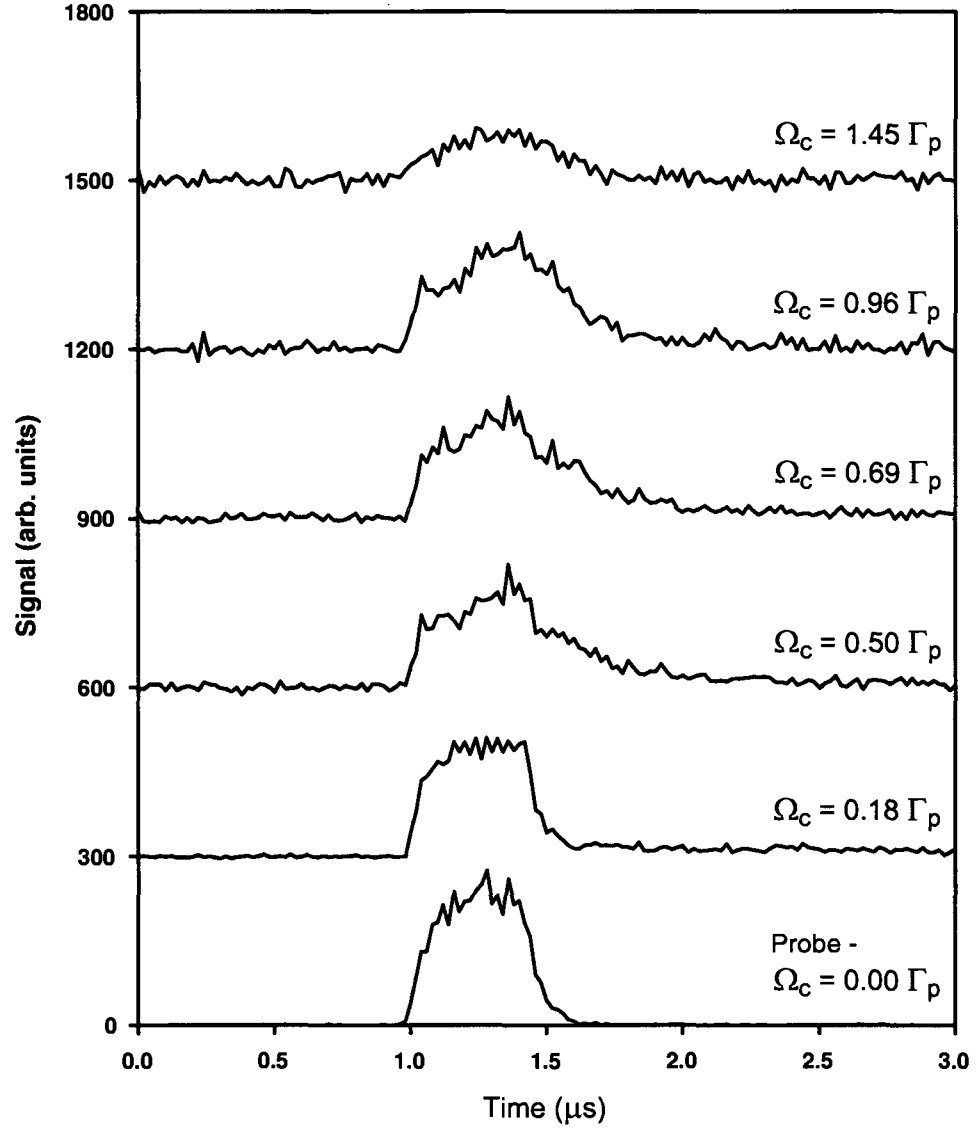


FIG. 38: Probe fluorescence from an EIT Rb cloud as a function of the control laser Rabi frequency Ω_c . The probe pulse is 500 ns long, on resonance ($\Delta_p = 0$). When $\Omega_c = 0$ we get a regular probe fluorescence signal, shown here for comparison. The control field is turned on 50 μ s before the probe pulse, and stays on for 60 μ s.

a Sommerfeld-Brillouin optical precursor. However, no optical precursor is expected to be seen in an observation of fluorescence. The slight overshoot of the probe field as it is turned on can be seen in the fluorescence signal. For a control field with a low intensity ($\Omega_c < \Gamma_p$), a slower build up of fluorescence is initially observed, but the transparency is small and it has a narrow frequency width, so the main contribution to the fluorescence signal comes from light scattered from atoms where no EIT conditions have been established. On the other hand, for large coupling field intensities ($\Omega_c > \Gamma_p$) the medium is more quickly driven into EIT conditions, and develops a high percentage of transparency for a wide frequency range (see Figs. 30, 32), and this results in a suppression of fluorescence clearly observed in Fig. 38.

For weak (but nonzero) control field Rabi frequencies (e.g. $\Omega_c = 0.69 \Gamma_p$) Fig. 38 exhibits an intriguingly slow decay of the fluorescence signal, which seems to become longer for weaker Ω_c . To explore this slow decay, a “storage and retrieval” of the slow fluorescence light was attempted; the relative timing of the probe and control pulses with respect to the observed fluorescence signal is similar to the timing for the transmission storage-and-retrieval measurements (see Fig. 34). The results are displayed in Fig. 39, with 5 ns resolution. For a coupling field Rabi frequency of $\Omega_c = 0.69 \Gamma_p$, the control field was turned off at $0.5 \mu\text{s}$ (any excitation traveling with the slow group velocity associated with EIT would be stored in the atomic medium), and turned back on with variable time delays (to retrieve the slow light pulse). According to the results presented in Fig. 36, the slow light retrieved signal has a $1/e$ decay rate of 170 ns; thus we expect no signal to be “retrieved” after a time delay on the order of μs . In contrast to this previous result, Fig. 39 shows that even after a $1 \mu\text{s}$ delay time, a signal is obtained upon switching the control field back on, with no apparent amplitude decay. This result is confirmed by a similar set of measurements, taken for a coupling field Rabi frequency of $\Omega_c = 0.18 \Gamma_p$, with a 80 ns resolution, presented in Fig. 40, where the control field has been turned off at $t = 6 \mu\text{s}$ and turned back on after variable time delays. In this plot a measurement for the case when there is no probe field and the control field is turned on/off for $5 \mu\text{s}$ is included for reference; this measurement demonstrates that the slowly decaying signal observed, when the control field is turned back on, is a result of the coherent processes that occur when the control and the probe field are on simultaneously.

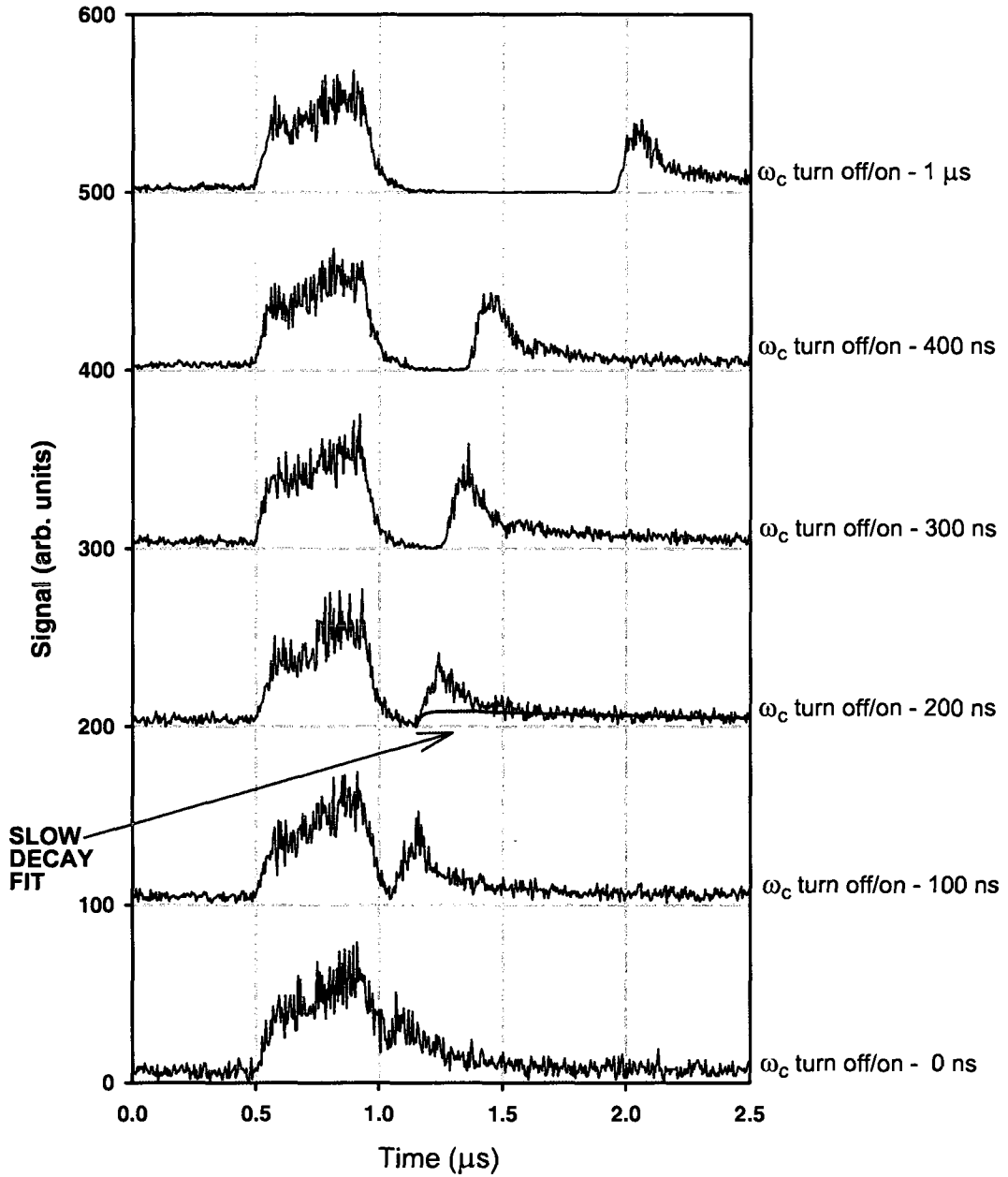


FIG. 39: Probe fluorescence as the control field ($\Omega_c = 0.69 \Gamma_p$) is turned off/on for various time delays. The probe pulse frequency is on resonance ($\Delta_p = 0$). The slowly decaying signal observed could be a result of optical pumping of atoms into the $F = 1$ level by the less-than-ideal control field; a fit of the data based on this process is shown.

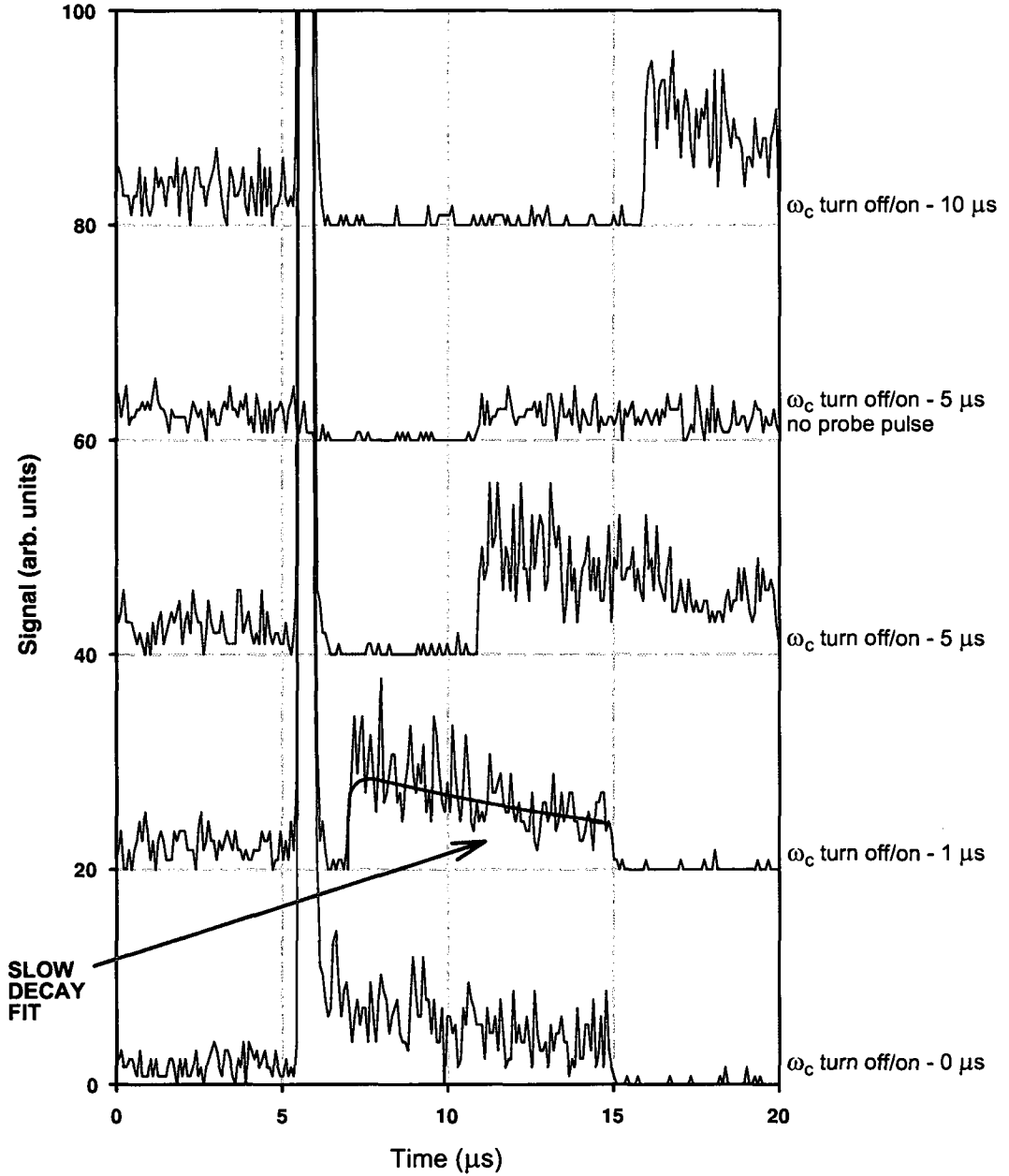


FIG. 40: Probe fluorescence as the control field ($\Omega_c = 0.18 \Gamma_p$) is turned off/on for various time delays. The probe pulse frequency is on resonance ($\Delta_p = 0$). The slowly decaying signal observed could be a result of optical pumping of atoms into the $F = 1$ level by the less-than-ideal control field; a fit of the data based on this process is shown. A measurement for the case when there is no probe field and the control field is turned on/off for 5 μs is included for comparison.

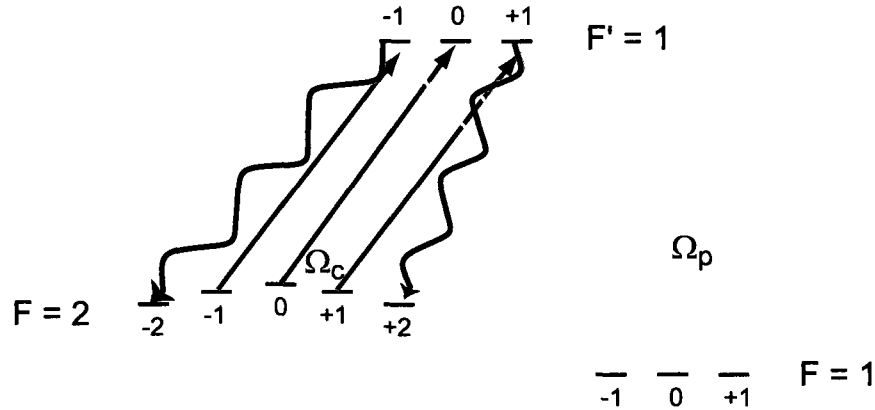


FIG. 41: Coherent optical pumping. This process is responsible for a small population leak into the $F = 2, m = \pm 2$ sublevels, which are not directly involved in an EIT Λ scheme.

We believe the long-lived signals observed after the control beam is turned back on are the result of coherent optical pumping (COP), and optical pumping upon the control field switch on. Coherent optical pumping is a process which occurs as a consequence of establishing EIT in a realistic system, where both EIT (or CPT) and optical pumping are present [98, 99]. Although most of the atoms remain in the dark state $|NC\rangle$, because of the decoherence of the ground states and the imperfect transparency established by the light-shifted Λ 's, there is a small leak of atomic population to the hyperfine sublevels not involved in a Λ scheme ($F = 2, m = \pm 2$), as is illustrated by Fig. 41. Approximately 0.1% of the control beam is linearly polarized orthogonal to the main beam; this percentage can be increased as the beam enters the chamber, since the windows can be slightly birefringent. Given the intensity of the control beam, when the control field is turned back on this small percentage can be enough to excite the atoms in the $F = 2, m = \pm 2$ sublevels and optically pump them into the $F = 1$ level. Since the portion of the control field with the right polarization to optically pump the atoms is small, it is expected that the process will be slow.

In order to test the validity of this explanation, we treat the atomic system as a simplified four-level atom and use a rate-equation approach to model the behavior of the atomic populations. The fluorescence signal observed depends on the population of the excited level. This model is presented in Appendix C. Figures 39 and 40

show satisfactory fits to the data for the slow decay of the signals based on the rate equations model.

In addition to a slowly decaying signal, Fig. 39 exhibits an additional transient when the control field is turned back on, with a significant amplitude, and much faster decay. It is also clear, from looking back at Fig. 38 that a portion of this transient signal is the result of the ground-states coherence that has been established in the atomic medium via EIT. We put forward as a possible explanation for this fast-decay transient that partial coherent population transfer has occurred [100]. In the ideal coherent population transfer process the dark state is described by

$$|NC\rangle = \cos\Theta |1\rangle - \sin\Theta |2\rangle, \quad (93)$$

where $|1\rangle$ and $|2\rangle$ are the coherently coupled states (and $|3\rangle$ is the excited and uncoupled state, see Fig. 7). The mixing angle is given by

$$\tan\Theta = \frac{\Omega_p}{\Omega_c}. \quad (94)$$

In this form it can be seen that the atoms can be driven from one level to the other. If the Rabi frequencies change adiabatically (slowly) then the state described by $|NC\rangle$ has time to adjust to the changing Rabi frequencies by rotating through the mixing angle Θ , which implies a transfer of population between the coherent states. The condition for adiabatic evolution is given by Eq. (41).

Although throughout the description of the measurements and data we have implied that the population remains basically in the $F = 1$ ground level (given the weak intensity of Ω_p), there is in fact some coherent population transfer. If the system evolved adiabatically during the control field turn-off, then the population would be transferred back to the $F = 1$ level. If the system does not evolve adiabatically, then upon the control field turn-off a considerable number of atoms remain in the $F = 2, m = 0, \pm 1$ ground levels. Since the EIT process is much more efficient for the $\Omega_c = 0.69 \Gamma_p$ measurements than for the $\Omega_c = 0.18 \Gamma_p$, this effect is more noticeable. In this context, the fast transient observed in Fig. 39 when the control field is switched back on is simply due to optical pumping into the $F = 1$ ground level. An estimate of the adiabatic condition for our system is presented in Appendix B.

It is very interesting to notice the rising portion of the transient signals observed in Fig. 39, when the control field is switched off for 100 and 200 ns. The rise of the fluorescence signal does not appear to be smooth, as if there was an additional process

occurring. Given the data obtained for the transmission measurements of slow light retrieval (Fig. 35), for a control Rabi frequency $\Omega_c = 0.69 \Gamma_p$, it is precisely in these two measurements (control field switch off/on with 100 ns and 200 ns time delay) that we would expect to observe fluorescence from slow-light processes. At this point, considering the contribution of optical pumping to the transient signals observed, and the signal-to-noise ratio of the data, any further discussion of slow-light fluorescence will have to wait for a comprehensive theoretical analysis of the data.

Finally, for a coupling laser Rabi frequency $\Omega_c = 0.69 \Gamma_p$, a set of measurements was taken to observe the fluorescence from the probe, as it propagates through the coherently prepared atomic medium, as a function of probe laser frequency detuning from resonance Δ_p ; the results are shown in Fig. 42. The data has been normalized to ordinary probe fluorescence as it propagates through the MOT cloud. The solid line is a fit to the data for an optical depth of $b = 3$, for EIT in an ideal three-level Λ configuration.

The region of reduced fluorescence naturally corresponds to the EIT transparency frequency window, where absorption-reemission processes are suppressed; this feature has a sub-natural width, just as in the transmission measurements. The effect produced on the transparency as a result of the light-shifts due to the atomic-control field interaction with the different hyperfine levels, which was discussed in the previous section, is noticeable in the observed fluorescence signal as well. As in Fig. 32, the frequency window where the transparency occurs is wider, asymmetrical, and its center is shifted to frequencies below $\Delta_p = 0$. The data presented in Figs. 32 and 42 shows very clearly the complementary nature of forward and diffusely scattered light.

It is clear, however, that a calculation for a realistic system is necessary in order to discuss the data more quantitatively. Currently, the calculations are underway by the group of D. Kupriyanov and I. Sokolov at the State Polytechnic University in St. Petersburg, Russia.

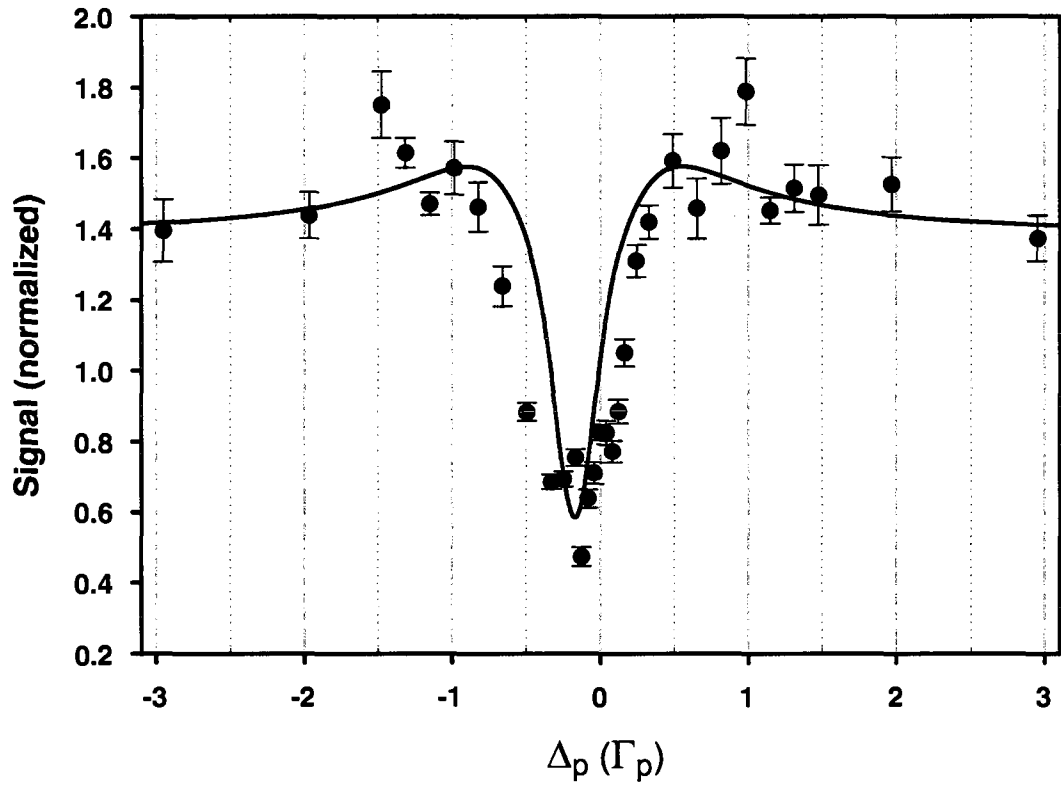


FIG. 42: Probe fluorescence from an EIT prepared medium as a function of probe frequency detuning Δ_p . The control field Rabi frequency is $\Omega_c = 0.69 \Gamma_p$. The circles correspond to data normalized to probe fluorescence from a MOT cloud. The solid line is a fit to the data for an optical depth of $b = 3$.

CHAPTER V

CONCLUSIONS AND FUTURE EXPERIMENTS

In conclusion, a comparison between forward and diffusely scattered light propagating in ultracold ^{87}Rb atomic vapor, coherently prepared through the process of electromagnetically induced transparency has been presented. This project is part of an ongoing effort to characterize the processes, such as diffusion, that contribute to coherence loss in atomic media under conditions of electromagnetically induced transparency, for applications in realistic systems.

A ^{87}Rb MOT has been built, and the atomic vapor sample has been characterized in terms of atomic density, shape and size, temperature, and optical depth. A Λ -type EIT system has been established through the sample by two co-propagating beams. The two laser fields are not phase-locked, so ground state coherence is affected by the lasers' phase fluctuations. Although the ground states decoherence rate is not negligible, for pulses of short duration (hundreds of nanoseconds), and lasers of similar characteristics (bandwidth, wavelength, electronic and environmental conditions) the relative phase between the control and probe lasers is approximately constant for sufficient time intervals. Thus, while a transparency can be established to some degree through the sample, the width of the transparency frequency window is broadened, and coherences are short-lived. Similar sets of measurements for the forward and diffusely scattered light were made for different conditions of probe pulse length, control field intensity, and probe field frequency detuning. Storage and retrieval of slow light pulses was achieved for the forward scattering (transmission) channel, but was not observed unambiguously in the diffusely scattered (fluorescence) channel. As a consequence of establishing EIT in a realistic system, coherent optical pumping occurs, and the fluorescence observed from optical repumping, when the probe field is turned off, has sufficient amplitude and time duration to obscure any fluorescence features corresponding to slow light processes.

In a realistic system, such as a ^{87}Rb atom, the hyperfine and Zeeman structures have significant decoherence effects on the EIT schemes, and need to be included for a successful description of the system. Theoretical calculations including the multilevel structures and incorporating the effects of multiple scattering are underway.

As in any experiment, the setup can be improved in a variety of ways. For future experiments using this (or similar) equipment and setup, the following suggestions are made:

As in any atomic physics laboratory, it is crucial to perform the experiment in the most stable environment possible; this could be accomplished by using an additional optical table and having separate laser and Rb chamber setups.

In order to pursue slow light storage and retrieval experiments, whether in a transmission or fluorescence detection setup, the most obvious improvement is to have a pair of phase locked lasers for the probe and coupling beams, thus having perfect phase coherence between them. Incorporating a variable attenuator in the AOM setup would also allow the coupling laser intensity (and Rabi frequency) to be varied in different ways and at different speeds, allowing the system to be optimized.

In pursuing fluorescence vs. transmission experiments, using a second PMT detector would be invaluable, as then direct comparisons would be possible which would not require changing the setup, and a direct calibration between the fluorescence and transmission signals would be a standard procedure.

Future experiments are already underway. For completeness sake the experiment should be done (selecting appropriate hyperfine transitions) in a ^{85}Rb MOT; since the ratio of ^{85}Rb to ^{87}Rb is 72% to 28%, the signal-to-noise ratio would be proportionally better.

An exciting experiment would be to perform slow light storage and retrieval in a transmission and fluorescence detection setup in an optical dipole trap, which can produce significantly higher atomic densities approaching the recurrent scattering regime. Other experiments involving multiple scattering in a coherently prepared medium include observation of coherent backscattering, the search for the dark state diffuse polariton predicted by Datsyuk et al. [43], and coherent preparation of the medium by a very intense far-detuned coupling field while allowing the probe laser frequency to be near a multiple scattering resonance.

BIBLIOGRAPHY

- [1] M. Klein, Y. Xiao, A. V. Gorshkov, M. Hohensee, C. D. Leung, M. R. Browning, D. F. Phillips, I. Novikova, and R. L. Walsworth, *Proc. of SPIE* **6904**, 69040C (2008).
- [2] J. P. Marangos, *J. Mod. Opt.* **45**, 471 (1998).
- [3] J. P. Marangos and T. Halfmann, *Handbook of Optics: Fiber Optics and Non-linear Optics* Vol. IV, 2nd. Ed., (McGraw Hill, New York, 2001).
- [4] U. Fano, *Phys. Rev.* **124**, 1866 (1961).
- [5] E. Arimondo and G. Orriols, *Nuovo Cimento* **17**, 333 (1976).
- [6] E. Arimondo, *Progr. Opt.* **35**, 259 (1996).
- [7] G. Alzetta, A. Gozzini, L. Moi, and G. Orriols, *Nuovo Cimento B* **36**, 5 (1976).
- [8] H. R. Gray, R. M. Whitley, and C. R. Stroud, *Opt. Lett.* **3**, 218 (1978).
- [9] A. S. Zibrov, M. D. Lukin, D. E. Nikonov, L. Hollberg, M. O. Scully, V. L. Velichansky, and H. G. Robinson, *Phys. Rev. Lett.* **75**, 1499 (1995).
- [10] G. G. Padmabandu, G. R. Welsh, I. N. Shubin, E. S. Fry, D. E. Nikonov, M. D. Lukin, and M. O. Scully, *Phys. Rev. Lett.* **76**, 2053 (1996).
- [11] D. S. Wiersma, *Nature Phys.* **4**, 359 (2008).
- [12] A. M. Akulshin, S. Barreiro, and A. Lezama, *Phys. Rev. A* **57**, 2996 (1998).
- [13] A. Lezama, S. Barreiro, and A. M. Akulshin, *Phys. Rev. A* **59**, 4732 (1999).
- [14] S. E. Harris, J. E. Field, and A. Imamoglu, *Phys. Rev. Lett.* **64**, 1107 (1990).
- [15] K. J. Boller, A. Imamoglu, and S. E. Harris, *Phys. Rev. Lett.* **66**, 2593 (1991).
- [16] J. E. Field, K. H. Hahn, and S. E. Harris, *Phys. Rev. Lett.* **67**, 3062 (1991).
- [17] S. E. Harris, J. E. Field, and A. Kasapi, *Phys. Rev. A* **46**, R29 (1992).
- [18] A. Kasapi, M. Jain, G. Y. Yin, and S. E. Harris, *Phys. Rev. Lett.* **74**, 2447 (1995).

- [19] A. Kasapi, Phys. Rev. Lett. **77**, 1035 (1996).
- [20] Y. Li and M. Xiao, Phys. Rev. A **51**, R2703 (1995).
- [21] J. Gea-Banacloche, Y. Q. Li, S. Jin, and M. Xiao, Phys. Rev. A **51**, 576 (1995).
- [22] M. Xiao, IEEE J. Quantum Electron. **9**, 1077 (2003).
- [23] M. Xiao, Y. Q. Li, and J. Gea-Banacloche, Phys. Rev. Lett. **74**, 666 (1995).
- [24] H. Wang, D. J. Goorskey, and M. Xiao, Phys. Rev. A **65**, 011801 (2001).
- [25] H. Wang, D. J. Goorskey, and M. Xiao, Phys. Rev. A **65**, 051802 (2002).
- [26] M. Fleischhauer, A. Imamoglu, and J. P. Marangos, Rev. Mod. Phys. **77**, 633 (2005).
- [27] K. Hakuta, L. Marmet, and B. P. Stoicheff, Phys. Rev. Lett. **66**, 596 (1991).
- [28] G. Z. Zhang, K. Hakuta, and B. P. Stoicheff, Phys. Rev. Lett. **71**, 3099 (1993).
- [29] P. R. Hemmer, D. P. Katz, J. Donoghue, M. Cronin-Golomb, M. S. Shariar, and P. Kumar, Opt. Lett. **20**, 982 (1995).
- [30] A. S. Zibrov, M. D. Lukin, and M. O. Scully, Phys. Rev. Lett. **83**, 4049 (1999).
- [31] L. V. Hau, S. E. Harris, Z. Dutton, and C. H. Behroozi, Nature **397**, 594 (1999).
- [32] C. Liu, Z. Dutton, C. H. Behroozi, and L. V. Hau, Nature **409**, 490 (2001).
- [33] Z. Dutton, N. S. Ginsberg, C. Slowe, and L. V. Hau, Europhys. News **35**, 33 (2004).
- [34] D. F. Phillips, A. Fleischhauer, A. Mair, and R. L. Walsworth, Phys. Rev. Lett. **86**, 783 (2001).
- [35] M. D. Lukin and A. Imamoglu, Nature **413**, 273 (2001).
- [36] M. D. Lukin, Rev. Mod. Phys. **75**, 457 (2003).
- [37] M. D. Eisaman, M. Fleischhauer, M. D. Lukin, and A. S. Zibrov, Opt. Photonics News **17**, 22 (2006).
- [38] M. D. Lukin, S. F. Yelin, and M. Fleischhauer, Phys. Rev. Lett. **84**, 4232 (2000).

- [39] M. Fleischhauer and M. D. Lukin, Phys. Rev. Lett. **84**, 5094 (2000).
- [40] M. Fleischhauer and M. D. Lukin, Phys. Rev. A **65**, 022314 (2002).
- [41] T. Chanelière, D. N. Matsukevich, S. D. Jenkins, S. Y. Lan, T. A. B. Kennedy, and A. Kuzmich, Nature **438**, 833 (2005).
- [42] L. M. Duan, M. D. Lukin, J. I. Cirac, and P. Zoller, Nature **414**, 413 (2001).
- [43] V. M. Datsyuk, I. M. Sokolov, and D. V. Kupriyanov, Phys. Rev. A **74**, 043812 (2006).
- [44] M. D. Havey, Contemp. Phys. **50**, 587 (2009).
- [45] Y. Castin, J. Dalibard, and C. Cohen-Tannoudji, in *Laser Cooling and Trapping of Neutral Atoms*, proceedings of the Trento Workshop on Bose-Einstein Condensation (BEC 93), edited by A. Griffin, D.W. Snoke and S. Stringari, (Cambridge University Press, Cambridge UK, 1995).
- [46] H. J. Metcalf and P. van der Straten, *Laser Cooling and Trapping* (Springer, New York, 1999).
- [47] F. Reif, *Fundamentals of Statistical and Thermal Physics* (McGraw-Hill, Boston, 1965).
- [48] S. Chu, L. Hollberg, J. E. Bjorkholm, A. Cable, and A. Ashkin, Phys. Rev. Lett. **55**, 48 (1985).
- [49] T. W. Hänsch and A. L. Shawlow, Opt. Commun. **13**, 68 (1975).
- [50] E. L. Raab, M. Prentiss, A. Cable, S. Chu, and D. E. Pritchard, Phys. Rev. Lett. **59**, 2631 (1987).
- [51] P. D. Lett, R. N. Watt, C. I. Westbrook, W. D. Phillips, P. L. Gould, and H. J. Metcalf, Phys. Rev. Lett. **61**, 169 (1988).
- [52] J. Dalibard and C. Cohen-Tannoudji, J. Opt. Soc. Am. B **6**, 2023 (1989).
- [53] P. D. Lett, W. D. Phillips, S. L. Rolston, C. E. Tanner, N. W. Watts, and C. I. Westbrook, J. Opt. Soc. Am. B **6**, 2084 (1989).
- [54] P. J. Ungar, D. S. Weiss, E. Rils, and S. Chu, J. Opt. Soc. Am. B **6**, 2058 (1989).

- [55] D. S. Weiss, E. Rils, Y. Shevy, P. J. Ungar, and S. Chu, *J. Opt. Soc. Am. B* **6**, 2072 (1989).
- [56] V. S. Letokhov, *Laser Control of Atoms and Molecules* (Oxford University Press, New York, 2007).
- [57] C. Wieman, G. Flowers, and S. Gilbert, *Am. J. Phys.* **63**, 617 (1995).
- [58] D. A. Steck, *Rubidium 87 D Line Data*, available online at <http://steck.us/alkalidata> (revision 2.1.1, 30 April 2009).
- [59] P. Lambropoulos and D. Petrosyan, *Fundamentals of Quantum Optics and Quantum Information* (Springer-Verlag, Berlin, 2007).
- [60] S. H. Autler and C. H. Townes, *Phys. Rev.* **100**, 703 (1955).
- [61] A. F. Molisch and B. P. Oehry, *Radiation Trapping in Atomic Vapours* (Oxford University Press, New York, 1998).
- [62] M. Weissbluth, *Photon-Atom Interactions* (Academic Press, Inc., San Diego, 1989).
- [63] R. E. Cunningham and R. J. J. Williams, *Diffusion in Gases and Porous Materials* (Plenum Press, New York, 1980).
- [64] F. Rief, *Fundamentals of Statistical and Thermal Physics* (McGraw-Hill, New York, 1965).
- [65] G. Labeyrie, C. A. Müller, D. S. Wiersma, C. Miniatura, and R. Kaiser, *J. Opt. B: Quantum Semiclass. Opt.* **2**, 672 (2000).
- [66] T. Holstein, *Phys. Rev.* **72**, 1212 (1947).
- [67] G. Labeyrie, E. Vaujour, C. A. Müller, D. Delande, C. Miniature, D. Wilkowski, and R. Kaiser, *Phys. Rev. Lett.* **91**, 223904 (2003).
- [68] A. Lagendijk and B. A. van Tiggelen, *Physics Reports* **270**, 143 (1996).
- [69] D. V. Kupriyanov, I. M. Sokolov, C. I. Sukenik, and M. D. Havey, *Laser Phys. Lett.* **3**, 229 (2003).
- [70] C. E. Wieman and L. Hollberg, *Rev. Sci. Instrum.* **62**, 1 (1991).

- [71] M. G. Littman and H. J. Metcalf, Appl. Opt. **17**, 2224 (1978).
- [72] K. C. Harvey and C. J. Myatt, Opt. Lett. **16**, 910 (1991).
- [73] K. B. MacAdam, A. Steinback, and C. E. Wieman, Am. J. Phys. **60**, 1098 (1992).
- [74] A. S. Arnold, J. S. Wilson, and M. G. Boshier, Rev. Sci. Instrum. **69**, 1236 (1998).
- [75] L. Ricci, M. Weidemüller, T. Esslinger, A. Hemmerich, C. Zimmermann, V. Vuletic, W. König, and T. W. Hänsch, Opt. Comm. **117**, 541 (1995).
- [76] C. J. Hawthorn, K. P. Weber, and R. E. Scholten, Rev. Sci. Instrum. **72**, 4477 (2001).
- [77] H. D. Young and R. A. Freedman, *University Physics* (Addison-Wesley Publishing Company, Inc., Massachussets, 1996).
- [78] W. Demtröder, *Laser Spectroscopy* (Springer-Verlag New York, 1996).
- [79] A. L. Schawlow, Rev. Mod. Phys. **54**, 697 (1982).
- [80] D. W. Preston, Am. J. Phys. **64**, 1432 (1996).
- [81] D. W. Preston and C. E. Wieman, (unpublished) *Doppler-free Saturated Absorption Spectroscopy: Laser Spectroscopy - Advanced Optics Laboratory*.
- [82] S. E. Park, H. S. Lee, T. Y. Kwon, and H. Cho, Opt. Comm. **192**, 49 (2001).
- [83] C. I. Sukenik, H. C. Busch, and M. Shiddiq, Opt. Comm. **203**, 133 (2002).
- [84] B. Dahmani, L. Hollberg, and R. Drullinger, Opt. Lett. **12**, 876 (1987).
- [85] M. Praeger, V. Vuletic, T. Fischer, T. W. Hänsch, and C. Zimmerman, Appl. Phys. B **67**, 163 (1998).
- [86] S. Q. Shang and H. Metcalf, Appl. Opt. **28**, 1618 (1989).
- [87] B. Razavi, IEEE J. Solid-State Circuits **39**, 1415 (2004).
- [88] E. A. Donley, T. P. Heavner, F. Levi, M. O. Tataw, and S. R. Jefferts, Rev. Sci. Instrum. **76**, 063112 (2005).

- [89] J. Wilson and J. F. B. Hawkes, *Optoelectronics: An Introduction* (Prentice-Hall, Inc., New Jersey, 1983).
- [90] M. H. Hablanian, *High-Vacuum Technology* (Marcel Dekker, Inc., New York, 1997).
- [91] J. H. Moore, C. C. Davis, and M. A. Coplan, *Building Scientific Apparatus* (Addison-Wesley Publishing Company, Inc., Massachussets, 1983).
- [92] A. Vorozcovs, M. Weel, S. Beattie, S. Cauchi, and A. Kumarakrishnan, *J. Opt. Soc. Am. B* **22**, 943 (2005).
- [93] D. Budker, D. F. Kimball, and D. P. DeMille, *Atomic Physics: an exploration through problems and solutions* (Oxford University Press, New York, 2004).
- [94] C. H. Greene and R. N. Zare, *Ann. Rev. Phys. Chem.* **33**, 119 (1982).
- [95] D. Wei, J. F. Chen, M. M. T. Loy, G. K. L. Wong, and S. Du, *Phys. Rev. Lett.* **103**, 093602 (2009).
- [96] H. Jeong and S. Ju, *Phys. Rev. A* **79**, 011802(R) (2009).
- [97] I. V. Jyotsna and G. S. Agarwal, *Phys. Rev. A* **52**, 3147 (1995).
- [98] E. A. Korsunsky, W. Maichen, and L. Windholz, *Phys. Rev. A* **56**, 3908 (1997).
- [99] D. E. Nikonov, U. W. Rathe, M. O. Scully, S. Y. Zhu, E. S. Fry, X. Li, G. G. Padmabandu, and M. Fleischhauer, *Quantum Opt.* **6**, 245 (1994).
- [100] K. Bergmann, H. Theuer, and B. W. Shore, *Rev. Mod. Phys.* **70**, 1003 (1998).
- [101] R. Loudon, *The Quantum Theory of Light*, 3rd. Ed. (Oxford Science Publications, New York, 2000).
- [102] M. O. Scully and M. S. Zubairy, *Quantum Optics* (Cambridge University Press, Cambridge UK, 1997).
- [103] D. J. Griffiths, *Introduction to Electrodynamics*, 2nd Ed. (Prentice-Hall, Inc., New Jersey, 1989).
- [104] C. Cohen-Tannoudji, B. Diu, and F. Laloë, *Quantum Mechanics* (Herman, John Wiley and Sons, Inc., Paris, 1977).

APPENDIX A

THE TWO-LEVEL ATOM

There are many excellent sources in the literature that present thorough studies of the two-level atom; this is not intended to be a comprehensive study, simply a semi-classical review of the aspects that are relevant when discussing EIT.

A.1 THE PROBABILITY AMPLITUDE APPROACH

Consider an ideal two-level atom at rest, with a ground energy state $|1\rangle$ and an excited state $|2\rangle$, with a resonant transition frequency $\omega_o = \omega_{21}$, in the presence of a near-resonant monochromatic laser field. Using the electric dipole approximation and taking the atom to be at the origin of the coordinate system, the spatial variations of the electric field can be neglected. Thus, the classical electromagnetic field can be described by a plane wave:

$$\vec{E}(t) = E_o \hat{e} \cos(\omega t) = \frac{E_o}{2} (e^{-i\omega t} + e^{i\omega t}), \quad (95)$$

where \hat{e} is the polarization vector and ω is the laser frequency, as shown in Fig. 43.

The unperturbed atom satisfies the following equations:

$$\hat{H}_o |k\rangle = E_k |k\rangle, \quad \langle n | k \rangle = \delta_{nk}, \quad (96)$$

$$\hat{H} |\psi(t)\rangle = \hat{H}_o |\psi(t)\rangle = i\hbar \frac{\partial}{\partial t} |\psi\rangle, \quad (97)$$

$$|\psi(t)\rangle = \sum_k a_k(t) |k\rangle e^{-i\omega_k t}, \quad (98)$$

$$a_k(t) = \langle k | \psi(t) \rangle, \quad P_k(t) = |a_k(t)|^2, \quad (99)$$

where $|k\rangle$ are the eigenstates (also known as the bare states) of the unperturbed Hamiltonian \hat{H}_o with eigenvalues $E_k = \hbar\omega_k$, $|\psi(t)\rangle$ is the atomic wave function, $a_k(t)$ is a probability amplitude and $P_k(t)$ is the probability of the atom to be in the state $|k\rangle$ at a time t .

According to time-dependent perturbation theory [101, 102], when a perturbation \hat{V} is added such that

$$\hat{H} = \hat{H}_o + \hat{V}, \quad (100)$$

the Schrödinger equation now reads:

$$i\hbar \frac{\partial}{\partial t} |\psi\rangle = \sum_k i\hbar \dot{a}_k |k\rangle e^{-i\omega_k t} + \sum_k \hbar\omega_k a_k |k\rangle e^{-i\omega_k t} = \hat{V} |\psi\rangle + \hat{H}_o |\psi\rangle; \quad (101)$$

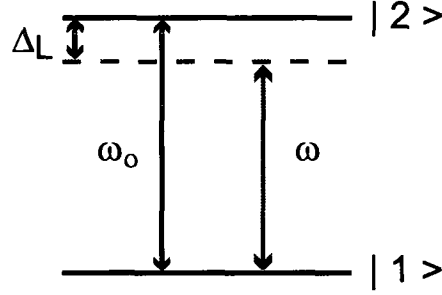


FIG. 43: An ideal two-level atom in the presence of a classical laser field. $|1\rangle$ is the ground state, $|2\rangle$ is the excited state, ω_o is the resonant transition frequency, ω is the laser frequency, Δ_L is the laser detuning from resonance.

comparing with Eqs. (96 - 98), it can be seen that

$$\hat{V}|\psi\rangle = \sum_k a_k \hat{V}|k\rangle e^{-i\omega_k t}. \quad (102)$$

Applying the orthogonality condition, multiply by $\langle n|$ to suppress the summation and leave only the terms

$$\dot{a}_n = \frac{1}{i\hbar} \sum_k a_k \langle n|\hat{V}|k\rangle e^{-i\omega_{kn}t}, \quad \omega_{kn} = \omega_k - \omega_n. \quad (103)$$

The perturbation is really the electric dipole operator,

$$\hat{V} = q\vec{E} \cdot \vec{r} = qE_o \hat{e} \cdot \vec{r} \cos(\omega t) = qE_o \hat{e} \cdot \vec{r} \frac{1}{2} (e^{i\omega t} + e^{-i\omega t}), \quad (104)$$

where Eq. (95) has been used, and \vec{r} is the operator specifying the electron coordinate for a one-electron atom.

Because only near-resonant interactions are considered, the \hat{V} operator (which has odd parity) only interacts with the two states $|1\rangle$ and $|2\rangle$. Combining equations (103) and (104) gives the coupled differential equations

$$\dot{a}_1 = \frac{1}{i\hbar} a_2 \frac{\langle 1|qE_o \hat{e} \cdot \vec{r}|2\rangle}{2} (e^{i(\omega-\omega_{21})t} + e^{-i(\omega+\omega_{21})t}), \quad (105)$$

$$\dot{a}_2 = \frac{1}{i\hbar} a_1 \frac{\langle 2|qE_o \hat{e} \cdot \vec{r}|1\rangle}{2} (e^{i(\omega+\omega_{21})t} + e^{-i(\omega-\omega_{21})t}). \quad (106)$$

Recall that $\omega_{21} = \omega_o$. It is assumed that $|\omega - \omega_o| \ll (\omega + \omega_o)$; using the Rotating-Wave Approximation (RWA) which focuses on slow dynamics, the fast oscillating

terms $e^{-i(\omega+\omega_o)t}$ are replaced by their zero average value. Define the laser's frequency detuning from resonance

$$\Delta_L = \omega - \omega_o, \quad (107)$$

and the previous equations (105, 106) reduce to:

$$\dot{a}_1 = \frac{1}{i\hbar} a_2 \frac{\langle 1|qE_o\hat{\epsilon} \cdot \vec{r}|2 \rangle}{2} e^{it\Delta_L}, \quad (108)$$

$$\dot{a}_2 = \frac{1}{i\hbar} a_1 \frac{\langle 2|qE_o\hat{\epsilon} \cdot \vec{r}|1 \rangle}{2} e^{-it\Delta_L}. \quad (109)$$

The Rabi frequency Ω , which characterizes the coupling between the atom and the radiation field, is defined as

$$\Omega = \frac{qE_o}{\hbar} \langle 2|\hat{\epsilon} \cdot \vec{r}|1 \rangle. \quad (110)$$

A.2 THE WEAK FIELD LIMIT

In the weak field excitation regime, it can be assumed that the probability amplitude for the atoms to be in the ground state is $a_1 \simeq 1$, and that initially there are no atoms in the excited state so that $a_2(0) = 0$. Then a_2 can be found by integrating Eq. (109), and in turn the probability $P_2(\omega, \hat{\epsilon})$ that at time t the atom is in the excited state:

$$a_2(t) = \frac{\Omega e^{\frac{-it\Delta_L}{2}}}{-i\Delta_L} \sin\left(\frac{t\Delta_L}{2}\right), \quad (111)$$

$$P_2(\omega, \hat{\epsilon}) = |a_2|^2 = \frac{|\Omega|^2}{\Delta_L^2} \sin^2\left(\frac{t\Delta_L}{2}\right). \quad (112)$$

Integrating over the bandwidth of the radiation field $\delta\omega$ and recalling the relationship between the cycle-averaged intensity, the electric field, and the energy density \bar{W} for an electromagnetic plane wave we obtain:

$$I = \frac{|E_o|^2}{2\mu_o c} = c\bar{W}, \quad (113)$$

$$\bar{P}_2(\hat{\epsilon}) = |\langle 2|\hat{\epsilon} \cdot \vec{r}|1 \rangle|^2 \frac{q^2\pi\bar{W}t}{\epsilon_o\hbar^2}. \quad (114)$$

If the angle between $\hat{\epsilon}$ and \vec{r} is θ , then an average over all the possible transition dipole moments means that the squared matrix element in Ω is:

$$\overline{|\langle 2|\hat{\epsilon} \cdot \vec{r}|1 \rangle|^2} = \overline{\cos^2\theta} |\langle 2|r|1 \rangle|^2 = \frac{1}{3} |\langle 2|r|1 \rangle|^2. \quad (115)$$

Recalling the Einstein coefficients and incorporating Eqs. (114) and (115):

$$\langle \bar{P}_2 \rangle = B_{12} \langle \bar{W} \rangle t, \quad (116)$$

$$\frac{B_{12}}{B_{21}} = \frac{g_2}{g_1}, \quad (117)$$

$$A_{21} = \frac{\hbar\omega^3}{\pi^2 c^3} B_{21}, \quad (118)$$

where B_{12} is the stimulated absorption coefficient, B_{21} is the stimulated emission coefficient, A_{21} is the spontaneous emission rate, g_1 and g_2 are the degeneracies of the ground and excited states of the atom respectively. Finally,

$$B_{12} = \frac{q^2 \pi}{3 \epsilon_0 \hbar^2} |\langle 2 | r | 1 \rangle|^2, \quad (119)$$

$$A_{21} = \frac{\omega^3 q^2 g_1}{3 \pi c^3 \epsilon_0 \hbar g_2} |\langle 2 | r | 1 \rangle|^2. \quad (120)$$

Equations (108, 109) can be solved exactly for the weak field approximation; applying the initial conditions $a_2(0) = 0$, $a_1(0) = 1$, yields:

$$a_2(t) = -i \frac{\Omega}{\Omega'} \sin\left(\frac{t\Omega'}{2}\right) e^{\frac{it\Delta_L}{2}}, \quad \Omega' = \sqrt{|\Omega|^2 + \Delta_L^2}, \quad (121)$$

where Ω' is known as the generalized Rabi frequency. This equation reveals that the probability $|a_2(t)|^2$ of finding the atom in the excited state $|2\rangle$ oscillates at a frequency Ω' , and that this frequency of oscillation increases with increasing detuning Δ_L from resonance, while the probability amplitude decreases.

Now, for a dilute ensemble of atoms, the atomic excitations are not in phase, so the time-dependence averages to 1/2, so for a steady ensemble excitation:

$$\langle P_2(t) \rangle = \frac{1}{2} \frac{|\Omega|^2}{\Omega'^2}. \quad (122)$$

Thus, the average probability of excitation has a Lorentzian lineshape, centered at ω_o , with full-width half-maximum (FWHM) of $2|\Omega|$.

So far, no damping phenomena have been included in the probability amplitudes. Consider now that the population of the excited state can decay via spontaneous emission, collisions, etc., such that:

$$P_2 = e^{-\Gamma_L t}, \quad \Gamma_L = A_{21}, \quad (123)$$

$$\tau = \frac{1}{\Gamma_L}, \quad (124)$$

where Γ_L is the bandwidth of the transition, and τ is the lifetime of the transition. Including this decay rate in the probability amplitude differential equation (109) gives

$$\dot{a}_2 = \frac{\Omega}{2i} a_1 e^{-it\Delta_L} - \left(\frac{\Gamma_L}{2}\right) a_2. \quad (125)$$

where a damping term has been added such that

$$a_1(t) = a_1(0)e^{-\frac{t\Gamma_L}{2}}, \quad P_2(t) = |a_1(0)|^2 e^{-t\Gamma_L}. \quad (126)$$

To solve this equation, define a new variable \tilde{a}_2 such that

$$\tilde{a}_2 = a_2 e^{\frac{t\Gamma_L}{2}}; \quad (127)$$

differentiation and term-by-term comparison with Eq. (125) yields

$$\dot{\tilde{a}}_2 = \frac{\Omega}{2i} a_1 e^{-it\Delta_L} e^{\frac{t\Gamma_L}{2}}. \quad (128)$$

Finally, integration with respect to t , input of initial conditions, and comparison with Eq. (127), gives the time-dependent probability amplitude for the atom to be found in the excited state:

$$a_2(t) = \frac{\Omega}{2} \left(\frac{e^{-it\Delta_L}}{\Delta_L + i\frac{\Gamma_L}{2}} \right). \quad (129)$$

A.3 OPTICAL ATTENUATION AND LINEAR SUSCEPTIBILITY OF THE MEDIUM

An electric field applied to an ensemble of atoms will polarize it as the atomic dipoles become lined up with the field [103]. The polarization \vec{P} of the ensemble is then proportional to the atomic density ϱ with average dipole moment $\langle \vec{p} \rangle$:

$$\vec{P} = \varrho \langle \vec{p} \rangle = \varrho (-q \langle \hat{\epsilon} \cdot \vec{r} \rangle). \quad (130)$$

The average dipole moment of the ensemble is given by

$$\langle \vec{p} \rangle = -q \langle \psi | \hat{\epsilon} \cdot \vec{r} | \psi \rangle, \quad (131)$$

where the atomic wavefunctions are given by Eq. (101). Recall that for the two-level atom the only two relevant levels are $|1\rangle$ and $|2\rangle$:

$$\langle \vec{p} \rangle = -q (a_1^* \langle 1 | e^{i\omega_1 t} + a_2^* \langle 2 | e^{i\omega_2 t} \rangle \hat{\epsilon} \cdot \vec{r} (a_1 | 1 \rangle e^{-i\omega_1 t} + a_2 | 2 \rangle e^{-i\omega_2 t}), \quad (132)$$

$$= -q (a_1^* a_2 \langle 1 | \hat{\epsilon} \cdot \vec{r} | 2 \rangle e^{-i\omega_0 t} + a_1 a_2^* \langle 2 | \hat{\epsilon} \cdot \vec{r} | 1 \rangle e^{i\omega_0 t}), \quad (133)$$

where $\omega_2 - \omega_1 = \omega_o$. Again, for the weak-field approximation, the initial conditions are that $a_1 \simeq a_1^* \simeq 1$ (most of the atoms remain in the ground state). Incorporating Eqs. (95), (129) gives

$$\langle \vec{p} \rangle = -\frac{q^2 E_o}{2\hbar} |\langle 2|\hat{\epsilon} \cdot \vec{r}|1 \rangle|^2 \left(\frac{e^{-i\omega t}}{\omega - \omega_o + \frac{i\Gamma_L}{2}} + \frac{e^{i\omega t}}{\omega - \omega_o - \frac{i\Gamma_L}{2}} \right). \quad (134)$$

The polarizability \vec{P} is proportional to the electric field E in Eq. (95) by the complex linear susceptibility $\chi(\omega)$ defined such that:

$$P(t) = \frac{\epsilon_o E_o}{2} \left(\chi(\omega) e^{-i\omega t} + \chi(-\omega) e^{i\omega t} \right), \quad (135)$$

then the linear susceptibility is found to be

$$\chi(\omega) = -\frac{q^2}{\epsilon_o \hbar} |\langle 2|\hat{\epsilon} \cdot \vec{r}|1 \rangle|^2 \left(\frac{\Delta_L - i\Gamma_L/2}{\Delta_L^2 + \left(\frac{\Gamma_L}{2}\right)^2} \right). \quad (136)$$

If the susceptibility is expressed in the complex form

$$\chi = \chi_r + i\chi_i, \quad (137)$$

where χ_r and χ_i refer to the real and imaginary parts of χ respectively; then the following equations are obtained:

$$\chi_r = -\frac{q^2}{\epsilon_o \hbar} |\langle 2|\hat{\epsilon} \cdot \vec{r}|1 \rangle|^2 \frac{\Delta_L}{\Delta_L^2 + \left(\frac{\Gamma_L}{2}\right)^2}, \quad (138)$$

$$\chi_i = \frac{q^2}{\epsilon_o \hbar} |\langle 2|\hat{\epsilon} \cdot \vec{r}|1 \rangle|^2 \frac{\frac{\Gamma_L}{2}}{\Delta_L^2 + \left(\frac{\Gamma_L}{2}\right)^2}, \quad (139)$$

Consider now the optical properties of the atomic medium. The complex susceptibility of the medium is related to the complex index of refraction n through

$$n = n_r + in_i, \quad n^2 = (1 + \chi) = \frac{\epsilon}{\epsilon_o}, \quad (140)$$

$$n_r \approx 1 + \frac{\chi_r}{2}, \quad (141)$$

$$n_i \approx \frac{\chi_i}{2}, \quad (142)$$

where n_r and n_i are the real and imaginary parts of n respectively.

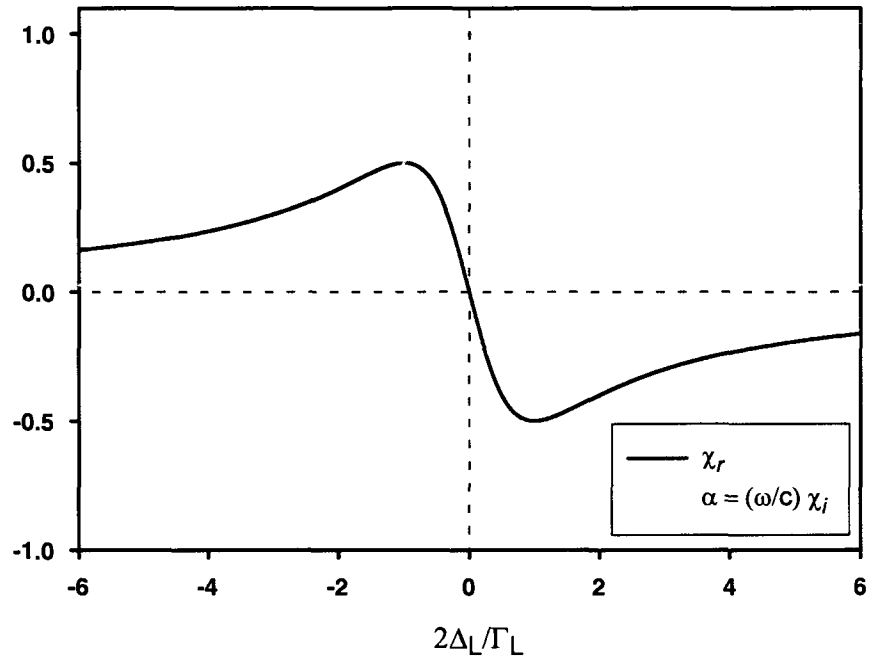


FIG. 44: Complex susceptibility $\chi(\omega)$ of a medium composed of two-level atoms. χ_r is the real part of the susceptibility. α is the absorption coefficient which depends on the frequency ω of the plane wave going through the medium, the imaginary part of the susceptibility χ_i , and the speed of light c . The complex susceptibility is plotted as a function of the normalized detuning from resonance $\Delta_L = \omega - \omega_o$, and the transition linewidth Γ_L .

The complex susceptibility is related to the complex permittivity: $\epsilon = \epsilon_o(1 + \chi)$ and so to the complex wave number $k = k_r + ik_i = \sqrt{\epsilon\mu_o}\omega$. By expressing the electric field \vec{E} in complex form $\vec{E}(z, t) = \vec{E}_o e^{i(kz - \omega t)} = \vec{E}_o e^{-k_i z} e^{i(k_r z - \omega t)}$, it becomes evident that the wave becomes attenuated, and that the attenuation is related to the imaginary part of the index of refraction through $k_i = \frac{\omega}{c} n_i$. Since the intensity of the wave is proportional to $|\vec{E}|^2$, then the absorption coefficient can be defined as:

$$\alpha = \frac{2\omega}{c} n_i = \frac{\omega}{c} \chi_i, \quad (143)$$

such that the intensity I of the wave decays over a distance z as $\frac{I}{I_o} = e^{-\alpha z}$ (the familiar Lambert-Beer law). Plugging in Eqs. (115), (120), (123), and (139) the absorption coefficient (which measures the optical depth of the sample) for unpolarized light is found to be:

$$\alpha = \frac{\rho \lambda^2 g_2}{2\pi g_1} \left(\frac{1}{1 + 4 \left(\frac{\Delta_L}{\Gamma_L} \right)^2} \right). \quad (144)$$

The real part of the susceptibility χ_r and the coefficient of absorption α are plotted in Fig. 44, as a function of the normalized detuning $2\Delta_L/\Gamma_L$. It can be seen that attenuation is maximum at the resonance frequency. The real part of the susceptibility χ_r , measures the dispersion of the medium. It can be seen that most of the time it increases with increasing frequency as is consistent with optics (increasing index of refraction for increasing frequency), but near a resonance it drops. Since this is not the usual behavior it is referred to as “anomalous dispersion”.

The phase velocity v_p of the wave can be found by

$$v_p = \frac{\omega}{k_r} = \frac{c}{n_r} = \frac{c}{1 + \chi_r/2} \simeq c(1 - \chi_r/2) \simeq c, \quad (145)$$

and the group velocity v_g , can also be found by recalling the equations:

$$v_g = \frac{d\omega}{dk}, \quad k = \frac{\omega n_r(\omega)}{c}, \quad (146)$$

$$\frac{1}{v_g} = \frac{dk}{d\omega} = \frac{1}{c} \left(\omega \frac{dn_r}{d\omega} + n_r \right). \quad (147)$$

This can be solved by inserting Eqs. (138) and (141) to get the following:

$$\frac{c}{v_g} = 1 + A \frac{x}{x^2 + 1} + \frac{2A\omega}{\Gamma_L} \left(\frac{1}{x^2 + 1} - \frac{2x^2}{(x^2 + 1)^2} \right), \quad (148)$$

$$x = \frac{2\Delta_L}{\Gamma_L}, \quad A = -\rho \frac{\lambda^3 g_2}{8\pi^2 g_1}. \quad (149)$$

A.4 THE DENSITY MATRIX APPROACH

This section closely follows the arguments of [102]. As in the probability amplitude approach, Eqs. (96) to (99), assume that there is a wave function $|\psi(t)\rangle$ that contains all the information of a system, satisfies Schrödinger's equation, and may be written as a superposition of a complete set of eigenstates $|k\rangle$. Physical observables may be measured by the expectation value of the associated operator \hat{Q} , such that

$$\langle \hat{Q} \rangle = \langle \psi | \hat{Q} | \psi \rangle. \quad (150)$$

For an ensemble of atoms, however, the wavefunction $|\psi\rangle$ of each atom is not necessarily known, only a statistical probability W_n for the atom to be in state $|\psi_n\rangle$, such that

$$\langle \hat{Q} \rangle = \sum_n W_n \langle \psi_n | \hat{Q} | \psi_n \rangle = \text{Tr}(\hat{Q}\hat{\rho}) = \text{Tr}(\hat{\rho}\hat{Q}), \quad (151)$$

$$\hat{\rho} = \sum_n W_n |\psi_n\rangle \langle \psi_n|, \quad (152)$$

where $\hat{\rho}$ is called the density matrix. The matrix elements are given by

$$\rho_{ij} = \sum_n W_n a_{in} a_{jn}^*, \quad (153)$$

$$\rho_{ii} = \sum_n W_n |a_{in}|^2, \quad (154)$$

where $|a_{in}|^2$ describes the probability that the n atom is in the state $|\psi_i\rangle$, and ρ_{ii} is the population of the ensemble which is in a state $|\psi_i\rangle$.

From Schrödinger's equation it is possible to obtain an equation of motion for the density matrix:

$$|\dot{\psi}\rangle = \frac{1}{i\hbar} \hat{H}_o |\psi\rangle, \quad (155)$$

$$\dot{\hat{\rho}} = \sum_n W_n \left(|\dot{\psi}_n\rangle \langle \psi_n| + |\psi\rangle \langle \dot{\psi}_n| \right), \quad (156)$$

$$\dot{\hat{\rho}} = \frac{1}{i\hbar} [\hat{H}, \hat{\rho}], \quad (157)$$

where Eq. (157) is called the Liouville equation. At this point it might be useful to remember the commutator and anticommutator brackets:

$$[\hat{a}, \hat{b}] = \hat{a}\hat{b} - \hat{b}\hat{a}, \quad \{\hat{a}, \hat{b}\} = \hat{a}\hat{b} + \hat{b}\hat{a}. \quad (158)$$

For the specific case of the two-level atom without spontaneous decay or any damping processes, the density matrix is given by

$$\rho = \begin{pmatrix} \rho_{22} & \rho_{21} \\ \rho_{12} & \rho_{11} \end{pmatrix} = \begin{pmatrix} a_2 a_2^* & a_1^* a_2 \\ a_1 a_2^* & a_1 a_1^* \end{pmatrix}. \quad (159)$$

Using Eq. (157) for the case of interaction with a near-resonant plane wave leads to the same equations (108), (109) as in the probability amplitude approach.

The finite lifetime of an excitation and any relaxation phenomena such as dissipation, decoherence, and damping can be incorporated by adding a relaxation matrix $\hat{\Gamma}'$ such that

$$\langle n | \hat{\Gamma}' | m \rangle = \Gamma_n \delta_{nm}, \quad (160)$$

$$\dot{\rho} = \frac{1}{i\hbar} [\hat{H}, \rho] - \frac{1}{2} \{ \hat{\Gamma}' \rho \}, \quad (161)$$

$$\dot{\rho}_{ij} = \frac{1}{i\hbar} \sum_k \left(H_{ik} \rho_{kj} - \rho_{ik} H_{kj} \right) - \frac{1}{2} \left(\Gamma'_{ik} \rho_{kj} + \rho_{ik} \Gamma'_{kj} \right). \quad (162)$$

The off-diagonal elements of the density matrix, ρ_{ij} , are called coherences, which decay according to the rates Γ_n .

Going back to the specific case of the two-level atom, incorporating spontaneous emission can be done by the exponential decay of the matrix element ρ_{21} at a rate $\frac{\Gamma_L}{2}$ such that

$$\dot{\rho}_{21} = -\frac{\Gamma_L}{2} \rho_{21}. \quad (163)$$

In a similar way the time evolution of the matrix element ρ_{21} would be altered to account for a gain in population due to the spontaneous emission process. The population of states $|1\rangle$ and $|2\rangle$, described by ρ_{11} and ρ_{22} respectively, would change at a rate Γ_L .

Solving the equations described by (162) for the time-evolution of the two-level atom system, including damping effects, under the RWA, gives the following equations [46]:

$$\tilde{\rho}_{12} = \rho_{12} e^{-it\Delta_L}, \quad \tilde{\rho}_{21} = \rho_{21} e^{it\Delta_L}, \quad (164)$$

$$\dot{\rho}_{11} = +\Gamma_L \rho_{22} + \frac{i}{2} \left(\Omega^* \tilde{\rho}_{21} - \Omega \tilde{\rho}_{12} \right), \quad (165)$$

$$\dot{\rho}_{22} = -\Gamma_L \rho_{22} + \frac{i}{2} \left(\Omega \tilde{\rho}_{12} - \Omega^* \tilde{\rho}_{21} \right), \quad (166)$$

$$\dot{\tilde{\rho}}_{12} = -\left(\frac{\Gamma_L}{2} + i\Delta_L \right) \tilde{\rho}_{12} + \frac{i}{2} \Omega^* (\rho_{22} - \rho_{11}), \quad (167)$$

$$\dot{\tilde{\rho}}_{21} = -\left(\frac{\Gamma_L}{2} - i\Delta_L \right) \tilde{\rho}_{21} + \frac{i}{2} \Omega (\rho_{11} - \rho_{22}). \quad (168)$$

The last four equations are called the optical Bloch equations, and they completely describe the evolution of the system. It is here that the power of the density matrix approach is revealed. The solution to the density matrix equation of motion contains time-dependent information about the statistical and quantum mechanical properties of an ensemble of atoms, in terms of populations, coherences, and relaxation effects, while at the same time it provides a simple way to calculate expectation values of physical observables. Systems of atoms with multiple levels and multiple coherences can analogously be studied by finding numerical solutions to the time-evolution density matrix elements.

For example, to derive the susceptibility of the medium, Eq. (133), may be rewritten as

$$\langle \vec{p} \rangle = -q (\rho_{21} \langle 1 | \hat{\epsilon} \cdot \vec{r} | 2 \rangle e^{-i\omega_o t} + \rho_{12} \langle 2 | \hat{\epsilon} \cdot \vec{r} | 1 \rangle e^{i\omega_o t}). \quad (169)$$

For steady state $\dot{\rho}_{21} = 0$, so from the optical Bloch equations above the following equation is obtained

$$\left(\frac{\Gamma_L}{2} - i\Delta_L \right) \rho_{21} = \frac{i}{2} \Omega (\rho_{11} - \rho_{22}); \quad (170)$$

the matrix element ρ_{21} may be found by applying the initial conditions $\rho_{11} \simeq 1, \rho_{22} \simeq 0$, and Eq. (164). Substituting ρ_{21} into Eq. (169) gives the equation

$$\langle \vec{p} \rangle = \frac{-\hbar}{2E} \left(\frac{|\Omega|}{\Delta_L + \frac{i\Gamma_L}{2}} e^{-i\omega t} + \frac{|\Omega|}{\Delta_L - \frac{i\Gamma_L}{2}} e^{i\omega t} \right), \quad (171)$$

and finally, term-by-term comparison with Eq. (135) gives the following expression for the linear susceptibility:

$$\chi(\omega) = -\frac{\rho q^2}{\epsilon_o \hbar} |\langle 2 | \hat{\epsilon} \cdot \vec{r} | 1 \rangle|^2 \left(\frac{\Delta_L - i\Gamma_L/2}{\Delta_L^2 + \left(\frac{\Gamma_L}{2} \right)^2} \right), \quad (172)$$

which is the same result found in Eq. (136).

A.5 THE AUTLER-TOWNES EFFECT

An exact solution can be found for Eqs. (108), (109). For the case of a strong field at resonance ($\Delta_L = 0$) the probability amplitudes oscillate as [56]:

$$a_1(t) = \cos \frac{\Omega t}{2}, \quad (173)$$

$$a_2(t) = \sin \frac{\Omega t}{2}. \quad (174)$$

Using the superposition principle, the wave function may be written as [104]:

$$\hat{H}|\psi(t)\rangle = a_1(t)\psi_1 e^{-i(E_1/\hbar)t} + a_2(t)\psi_2 e^{-i(E_2/\hbar)t}, \quad (175)$$

from which it follows that

$$|\psi(t)\rangle = \frac{1}{2} \sum_{k=1,2} \exp\left(-i\left(\frac{E_k}{\hbar} + \frac{\Omega}{2}\right)t\right) + \exp\left(-i\left(\frac{E_k}{\hbar} - \frac{\Omega}{2}\right)t\right). \quad (176)$$

This implies that the energy levels split into two sublevels with energies

$$E'_k = E_k \pm \frac{\Omega\hbar}{2}, \quad (177)$$

which have an energy difference of $\hbar\Omega$. This phenomenon was first explained in 1955 by Autler and Townes [60], and is referred to as the Autler-Townes doublet or Autler-Townes splitting.

APPENDIX B

ESTIMATE OF THE ADIABATIC EVOLUTION CONDITION

In CPT and EIT, the dark state is given in terms of a mixing angle Θ , such that

$$|NC\rangle = \cos\Theta |1\rangle - \sin\Theta |2\rangle, \quad (178)$$

$$\tan\Theta = \frac{\Omega_p}{\Omega_c}, \quad \sin\Theta = \frac{\Omega_p}{\Omega}, \quad \cos\Theta = \frac{\Omega_c}{\Omega}, \quad (179)$$

$$\Omega = \sqrt{\Omega_p^2 + \Omega_c^2}. \quad (180)$$

If the Rabi frequencies change adiabatically (slowly enough in time) then the non-coupling state described by $|NC\rangle$ has time to adjust to the changing Rabi frequencies by rotating through the angle Θ .

The condition for adiabatic evolution is that, as the ratio of the control and field Rabi frequencies changes, the dark state should be able to follow the rotation of the angle Θ [26, 59]. For the case when $\Delta_p = \Delta_c = 0$, this reduces to

$$\Omega(t) \gg |\dot{\Theta}|. \quad (181)$$

This can be expressed in a more convenient way, by finding the time-dependent mixing angle

$$\frac{d}{dt}(\tan\Theta) = \sec^2\Theta \frac{d\Theta}{dt} = \frac{d}{dt} \left(\frac{\Omega_p(t)}{\Omega_c(t)} \right), \quad (182)$$

and assuming that $\Omega_p \ll \Omega_c$. Then the condition for adiabatic following simplifies to

$$1 \gg \frac{\Omega_p}{\Omega_c^2} \left(\frac{\dot{\Omega}_p}{\Omega_p} - \frac{\dot{\Omega}_c}{\Omega_c} \right). \quad (183)$$

From the measured temporal profiles of the control and probe fields, we can estimate the ratio at which the laser fields turn-off (decay from $\simeq 90\% \rightarrow 10\%$):

$$\frac{\dot{\Omega}_c}{\Omega_c} \simeq -82 \text{ MHz}, \quad (184)$$

$$\frac{\dot{\Omega}_p}{\Omega_p} \simeq -67 \text{ MHz}, \quad (185)$$

$$\left(\frac{\dot{\Omega}_p}{\Omega_p} - \frac{\dot{\Omega}_c}{\Omega_c} \right) \simeq 15 \text{ MHz}. \quad (186)$$

On the other hand, comparing the intensities of the probe $I(\omega_p)$ and control $I(\omega_c)$ fields, for transmission (nW vs. mW) we find that $I(\omega_p) \approx I(\omega_c)^{-6}$ and for fluorescence (μ W vs. mW) we find that $I(\omega_p) \approx I(\omega_c)^{-3}$. If the Rabi frequencies are given in units of MHz, then

$$\frac{\Omega_p}{\Omega_c^2} \approx \text{value} \left(\frac{1}{\Omega_c^5} \right) \mu\text{s}, \quad \text{for transmission,} \quad (187)$$

$$\frac{\Omega_p}{\Omega_c^2} \approx \text{value} \left(\frac{1}{\Omega_c^3} \right) \mu\text{s}, \quad \text{for fluorescence.} \quad (188)$$

It can be seen that the condition for adiabatic following is easier to satisfy for the transmission measurements, where the difference between the intensities of the lasers is greater. We may now evaluate the condition of adiabatic evolution for a few values of the control field in transmission and fluorescence, these estimates are presented in Tables 4 and 5.

TABLE 4: Estimates of the condition for adiabatic evolution for the transmission measurements.

Control Rabi Frequency (Ω_c)	$\frac{\Omega_p}{\Omega_c^2} \left(\frac{\dot{\Omega}_p}{\Omega_p} - \frac{\dot{\Omega}_c}{\Omega_c} \right)$	Satisfies Condition ($\ll 1$)
1.45 $\Gamma_p = 8.8$ MHz	0.0003	yes
0.69 $\Gamma_p = 4.2$ MHz	0.01	yes
0.18 $\Gamma_p = 1.1$ MHz	9.3	no

TABLE 5: Estimates of the condition for adiabatic evolution for the fluorescence measurements.

Control Rabi Frequency (Ω_c)	$\frac{\Omega_p}{\Omega_c^2} \left(\frac{\dot{\Omega}_p}{\Omega_p} - \frac{\dot{\Omega}_c}{\Omega_c} \right)$	Satisfies Condition ($\ll 1$)
1.45 $\Gamma_p = 8.8$ MHz	0.02	yes
0.69 $\Gamma_p = 4.2$ MHz	0.2	yes, weakly
0.18 $\Gamma_p = 1.1$ MHz	12	no

APPENDIX C

OPTICAL PUMPING AND RATE EQUATIONS MODEL

As a way to understand the slow-decay transient signals observed on Figs. 39 and 40 when the control field is turned back on, we have used a rate-equation approach to model the data. This model is based on a four-level atom, as in Fig. 45, where levels 1, 2, and 4 have been involved in an EIT Λ -type scheme, and where population has leaked to level 3 due to coherent optical pumping. In this sense, level 3 models the behavior of atomic population that has decayed to the $F' = 2$, $m = \pm 2$ hyperfine levels in the real atomic system. This model is equivalent of a four-state density matrix approach, for which all coherences have been neglected.

The levels have atomic populations N_1, N_2, N_3 , and N_4 respectively. The atomic population of interest is concentrated initially in levels 2 and 3. When a field is applied at a time t , the population in the levels changes according to excitation and decay rates. g_0 is the rate of decay from the excited level 4 to level 1, g_1 is the rate of decay to level 2 and 3. We expect these decay rates to be proportional to the atomic spontaneous decay rate Γ_p . g_2 and g_3 are the excitation rates from levels 2 and 3 respectively. We expect these excitation rates to be proportional to the control field Rabi frequency, although $g_3 \ll g_2$.

The population of the atomic levels changes according to the following equations:

$$\frac{dN_1}{dt} = g_0 N_4, \quad (189)$$

$$\frac{dN_2}{dt} = g_1 N_4 - g_2 N_2, \quad (190)$$

$$\frac{dN_3}{dt} = g_1 N_4 - g_3 N_3, \quad (191)$$

$$\frac{dN_4}{dt} = g_2 N_2 + g_3 N_3 - (g_0 + 2g_1) N_4, \quad (192)$$

These equations have been solved numerically using *Mathematica 5.2* for initial conditions: $N_1(0) = 0, N_4(0) = 0, N_2(0) + N_3(0) = 1, \dot{N}_1(0) = 0$.

A fit to Fig. 39 for $g_0 = \Gamma_p, g_1 = \Gamma_p/2$ yielded the following values for the pumping rates: $g_2 = 3\Omega_c/4, g_3 = \Omega_c/50$. Using these rate values we have then calculated the decay rate for Fig. 40, and have found good agreement with the data for the slow decay transient.

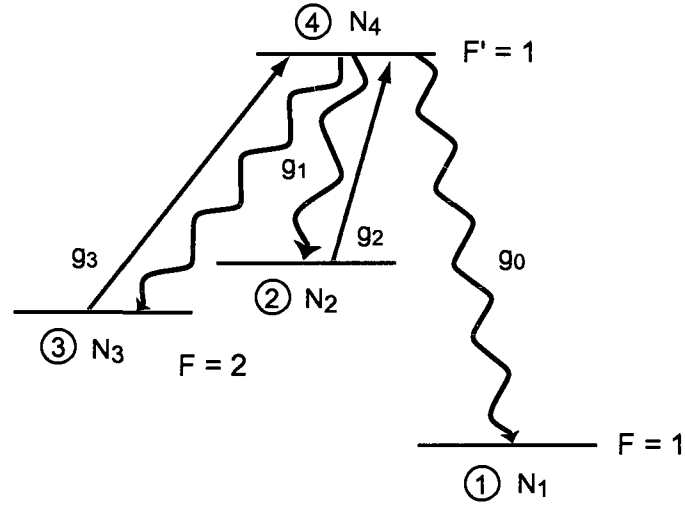


FIG. 45: Optical pumping and rate equations model. The model is based on a four-level atom, where levels 1, 2, and 4 have been involved in an EIT Λ -type scheme, and population has leaked to the level 3 due to coherent optical pumping. The levels have atomic populations N_1, N_2, N_3 , and N_4 respectively. When a field is applied at a time t , the population in the levels changes according to excitation and decay rates. g_0 is the rate of decay from the excited level 4 to level 1, g_1 is the rate of decay to level 2 and 3. g_2 and g_3 are the excitation rates from levels 2 and 3 respectively.

VITA

Rocio Gisela Olave
 Department of Physics
 Old Dominion University
 Norfolk, VA 23529

EDUCATION:

Ph. D. in Physics, Old Dominion University, December 2009
 M.S. in Physics, Old Dominion University, May 2003
 B.S. in Physics, Summa Cum Laude, University of Texas at El Paso, December 1999

ACADEMIC HONORS:

ODU Dominion Scholarship - 2000 to 2002
 UTEP College of Science Dean's List - 1997, 1998, 1999
 UTEP Outstanding Junior Physics Student - 1998

PUBLICATIONS:

Alignment dynamics of slow light diffusion in ultracold atomic ^{85}Rb .
 S. Balik, R. G. Olave, C. I. Sukenik, M. D. Havey, V. M. Datsyuk, I. M. Sokolov, D. V. Kupriyanov, Phys. Rev. A, **72**, 051402 (2005).
Spectral Dependence of diffuse light dynamics in ultracold atomic ^{85}Rb .
 S. Balik, R. G. Olave, C. I. Sukenik, M. D. Havey, V. M. Datsyuk, D. V. Kupriyanov, I. M. Sokolov, J. Mod. Opt., **53**, 2495 (2006).

EXTRACURRICULAR ACTIVITIES:

Preparing Future Faculty Certificate Program - 2009
 DAMOP and Student Symposium 2002, DAMOP 2006, DAMOP 2009
 GS RCR Compliance: Ethical, Legal, and Professional Standards Workshop - 2009
 PGSA - 2005 to 2009
 2004 Boulder Summer School - 2004
 HUGS at CEBAF, and Undergraduate Summer at JLAB - 1999

Typeset using L^AT_EX.